The Faroese Fisheries Laboratory

Fiskirannsóknarstovan

On the accuracy of computing slope current transports from current meter arrays

by

Hjálmar Hátún

Tórshavn

January 2001

On the accuracy of computing slope current transports from current meter arrays

Hjálmar Hátún

16.06.2000

Preface

This work is done as a final thesis for my degree "Sivilingeniør" at The Norwegian University of Science and Technology - NTNU. The work has been carried out at SINTEF Bygg og miljøteknikk in collaboration with the University. My main subject through this study has been Theoretical Physics, but this thesis is an attempt to converge toward Physical Oceanography. No previous knowledge on the subject is expected of the reader, and the special terminology is introduced before it is used. A lot of different data have been analysed and the thesis contains a lot of graphic visualization of these. I have tried to emphasize the figure texts, so that a reader can quickly get the essence without having to read all the main text.

02.09.2000: Some corrections have been done. The document is converted to a black and white format which is more easily distributed to the participants of the MAIA project. Some figures might regrettably be harder to understand in this format

Acknowledgement

I should like to thank my assistant supervisor Professor Thomas A. McClimans at SINTEF for good supervision during this work and always being ready to answer my questions. His efficiency to supply me with literature is also much appreciated. I also would like to thank Dr. Bogi Hansen at the Faroese Fisheries Laboratory (FFL) for his supplies of data and for the dialog with him via e-mail. His insight in the waters around the Faroes has helped me a whole lot. My supervisor and vocational contact to NTNU, Professor Johannes Falnes, deserves also the greatest of thanks. He has made sure that the formalities between SINTEF and NTNU concerning this thesis always were as prescribed. A thanks goes also to the staff at SINTEF and my the swedish colleague-student, Lars Nilsson, who has made the completion of this work much more fun. Trondheim 15/6-2000

Hjálmar Hátún

Contents

Abstract

Oceanographic data from a section to the north of the Faroe Islands are analyzed. These data come from ADCP current instruments deployed in the period 1994 to 1999, Aanderaa current meters deployed during two week in June '86, and hydrographic (CTD) data from this section sampled three to six times a year in the period 1987 to 1999. A combination of these data is used to establish an annually averaged current profile for this section, and an estimate for the volume flux is calculated from this profile. Averaged volume fluxes in the years 1997 and 1998, are found to be 4.17 Sv (Sv $= 10^6 m^3/s$) and 4.56 Sv, respectively. The current has a strong vertical current shear, and it has a jet-like character with the core centered above the 600-650 m isobaths. A tidal model is employed to remove the tidal currents in the ADCP data, and the residual current from this analysis is used to describe the form of the current jet at short time-scales. This method finds the instantaneous horizontal current shear of the jet. Water level data from Tórshavn are adjusted with air pressure measurements, and the adjusted sea-level is compared to current velocities and volume fluxes. Negative correlations are found from this analysis. Based on all this information, suggestions are given of where to deploy future current instruments to get the best data from the fewest instruments used.

Chapter 1
INTRODUCTION

The water flow from the Atlantic into the Nordic Seas is of great interest regarding global climatic changes, local climate, fisheries and other biological production. More detailed knowledge on how these currents flow on a smaller scale has in recent years received much attention from the oil-industry. Oil exploration in Faroese waters is the "hot potato" these days. The force from currents on risers, which are the tubes used for drilling and for oil transportation, increases drastically with depth, and the potentially exploitable areas south of the Faroes Islands are very deep.

This work is an attempt to gain geographical information on how currents flow to the north of the Faroe Islands, and from this information estimate yearly averaged volume fluxes in this region. Oil exploration is not expected in this region, but the measurement strategies used here, and those used in the Faroe-Shetland Channel (FSC) where test-drilling is about to begin, are the same. So it is likely that the knowledge obtained here can be used in the channel as well. The analysis is a part of the larger MAIA (Monitoring the Atlantic Inflow toward the Arctic) project, whose objective is to use coastal water level data to estimate Atlantic Water flux toward the Arctic. If this approach is successful, one has a way to use the historical data in flux calculations and much better statistics can thereby be obtained on climatic changes, extreme conditions and the interpretation of current meter data from random short period studies. The existing current data are so sparse at present that any reliable statistics can hardly be computed. This is because it is expensive to make *in situ* current measurements, while just measuring the water elevation at the coast is cost-effective. The MAIA project is in its beginning stage now and only an extensive compilation of historical data has been made. This thesis can be regarded as a preliminary assessment of what to expect in the Faroese regions. The later stages of MAIA will include a validation, or benchmark, of the model, including several types of measurements. From the sectional current profile form, I shall suggest a deployment strategy that can give the most comprehensive data coverage for a minimum of costs.

The major transport of Atlantic Water into the Nordic Seas is believed to occur in current jets that follow the bottom topography. The large continental shelves, from France past the British Isles and along Norway, are known to stabilize these mainly barotropic currents and steer them in quite confined areas. But there are many stochastic perturbations in the oceans, that influence this flow and there are more

regular oscillations like the tidal currents. Since these jets are confined to a restricted region, measurements placed say 10 km apart can give markedly different values. We can "step" on each side of a major current in a measurement series if we are not careful, and thereby conclude a far to low transport. Or opposite, we can make most measurements in a fast area and assume that the whole region has these large velocities. A good understanding of the sectional current profile is therefore most helpful.

The historical estimates of water masses passing the Greenland-Scotland section have assumed the major transport to be flowing through the Faroe-Shetland Channel. Later it is proposed that the flow between Iceland and the Faroes are considerably larger than has been generally assumed (Hansen et al. 1986).

A few estimates of the volume flux north of the islands can be found in the literature. Hermann (1949) estimated 4.5 Sv (Sv $= 10^6 m^3/s$), but only a part of this was Atlantic Water. Tait (1957) cites a number, based on hydrographic data, of considerable smaller magnitude. The first estimates based on observed currents are presented by Hansen et al. (1986) and the conclusions were a total flow of 3-4 Sv, which gave an Atlantic Water flux of 2.9 Sv. These estimates are based on Aanderaa current meter data, and the same data are included in this work. The most recent estimation is given by Hansen et al.(1999), and this is based on ADCP (Acoustic Doppler Current Profiler) and CTD (Conductivity, Temperature, Depth) data from this same region. The conclusions were that the average total volume flux was 4.5-4.8 Sv, giving an Atlantic Water flux of 3.0-3.7 Sv, in the two years 1997-99.

Chapter 2
BATHYMETRY AND STREAM PATTERN

The Faroe Islands lie on a bank which in the south is separated from the Shetland-Scotland shelf by the fairly deep Faroe-Shetland Channel, and in the north-west is connected to the Iceland-Faroe Ridge (IFR) (figure 2.1). This ridge goes all the way from the Faroe shelf to Iceland with depths along the crest of 300-500m, generally deepening from the Iceland to the Faroese end. The ridge is wide and slopes gradually down into the abyss on both the east and the west side. But the isobaths (lines of equal depth) on the eastern side converge when approaching the Faroe shelf. North east of the islands at about $5\text{-}6°W$, these lines of equal depth get very close indicating a steep shelf as shown in figure 2.2. The isobaths are nearly parallel in this region and their inclination to the east-west line is approximately $15°$ south of east. Following these lines further east we see that they diverge again, and when the deep isobaths keep following a nearly east-west route, the shallower ones turn southwards.

Just southwest of the Faroe Islands, we find the Faroe Bank (FB) which is isolated from the main shelf by the deep Faroe Bank Channel. The depth on the bank itself is shallower than 200m but the channel gets deeper than 800 m.

The North Atlantic Current (NAC), that originates from a branch of the well known Gulf Current, finds the Greenland-Scotland ridge as a hindrance on its way to the Nordic Seas. The Faroe-Shetland Channel, the Iceland-Faroe Ridge and the Denmark Strait are used as pathways for this flow as shown in figure 2.1. The presence of Atlantic Water on the Iceland-Faroe Ridge has been known for a long time (Nielsen, 1904), and a qualitative flow pattern was already given by Helland-Hansen and Nansen (1909). This picture has not been altered much through the years, and numerous experiments have since confirmed a pattern like the one that is sketched in figure 2.1. The Overflow '60 expedition (Tait 1967) has verified the dominating presence of Atlantic Water; the Overflow '73 experiment could confirm the current directions with short term current meters, and more recently drifter experiments have shown the same character (Poulain et al. 1996).

The time that it takes the drifters to pass the ridge varies greatly, from two weeks to half a year (Hansen and Østerhus, 2000, pp.136). The drifters can get caught on the ridge for some time making clockwise rotations, before moving into the Nordic Seas. But there are also examples of drifters that enter the slope region west of the Faroes and follow the bottom topography in regular paths, crossing the ridge where
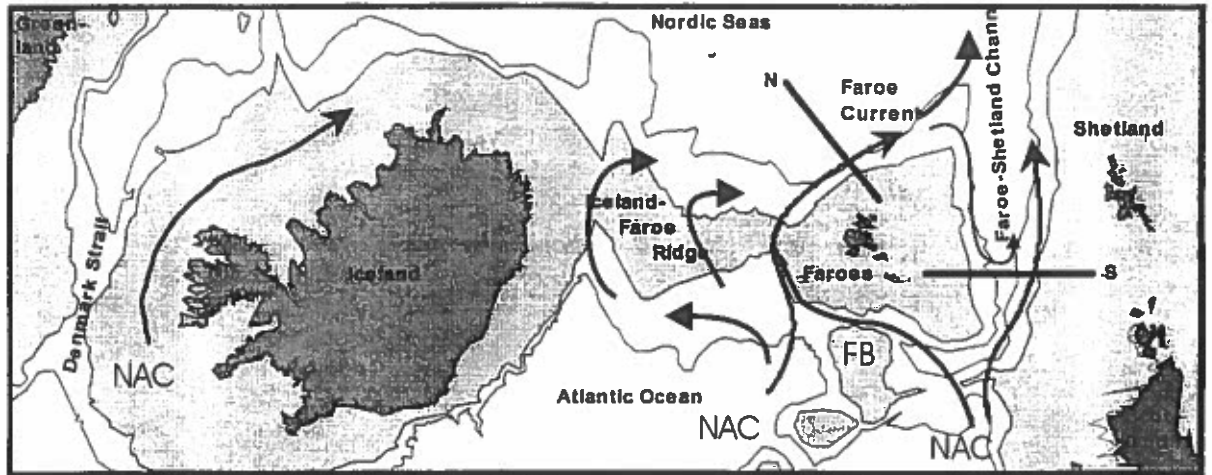
Figure 2.1   Bathymetry and main flow pattern across the Greenland-Scotland Ridge. The current branches that become the Faroe Current are shown and its further flow into the Nordic Seas is indicated. (Source: B.Hansen, privat communication)

Figure 2.2   Top view of the Faroe Plateau. The shelf guided fast track is shown with the thin arrow, and the thicker arrow shows the currents coming over the Iceland-Faroe Ridge closer to Iceland. The white line indicates the measurement section.

Figure 2.3 Birds eye view of bottom topography, having the Faroe Plateau on the right. We see how the Iceland-Faroe Ridge is sloping into the depth of the Norwegian Sea. The measurement section is shown in white, and the currents are drawn with black arrows.

it slopes up towards the northern Faroe shelf. These can enter the slope through the Faroe Bank Channel or north of the bank as shown in figure 2.1, and might have entered the fast track that is a main theme of this thesis.

The shelf-guided current follows the isobaths north of the Faroes, but water that has crossed the ridge close to Iceland and water from the North Icelandic Irminger Current, which originates in the Denmark Strait follow the flow in a more southerly direction when approaching the Faroe shelf. This is illustrated in figure 2.3, where the thin arrow is the fast track and the wider arrow represents the current coming from Iceland.

These two current branches converge in the region where we have the steep slope as mentioned, making this area well suited for current measurements.

The current is now termed the 'Faroe Current' (FC) (Hansen and Meincke, 1984), and this current gives a considerable contribution to the total volume flux further north to the Arctic regions. When water in the Faroe Current flows further east, east of about 4° W, it gets affected by the diverging isobaths. It has to continue eastward without bottom steering or turn the corner, where shallow isobaths turn

south, and proceed into the Faroe-Shetland Channel as shown in figure 2.1. The branch that turns south will eventually join the slope current from the south that has crossed the Wyville Thomson ridge and continues up towards the Norwegian continental slope.

On the Faroe shelf itself, which is illustrated in figure 2.2, there is the Faroe Coastal Current (termed FCC in the figure) which circulates clockwise around the islands. This current should not be included when calculating volume flux of the Faroe Current, because this water is not transported north toward the Arctic. The boundary between the Faroe Current and the circulating coastal current must be estimated.

The upstream conditions are always important for flow character and our digitalized 3-D images of the bathymetry north of the Faroes give a nice impression of this.

Atlantic water masses do not reach much deeper than 500m in the Nordic Seas and beneath this lies colder Arctic Intermediate Water. The deep regions shown in figures 2.2 and 2.3 act as a buffer region for the Iceland-Scotland overflow water, which is a common name for southerly flowing currents to the deep ocean (this 'Overflow' is heavier, colder water flowing towards the equator). Most of the water from the buffer region flows through the Faroe-Shetland Channel, but one small branch reaches over the Iceland -Faroe ridge close to the Faroe shelf. One can imagine that this backflow establishes a thermocline (layer of sharp temperature differences) that acts as a level 'floor' for all Inflowing Atlantic water.

2.1 Instrumentation and mooring positions

2.1.1 Aanderaa Instruments

The Aanderaa current meter (RCM-4) is a half meter high metal cylinder connected to a fin as shown in figure 2.4. On top of the cylinder there is a propeller, a pressure sensor, a termistor and conductivity sensor if the instrument is fully equipped. Inside the cylinder body there is a counter that counts propeller revolutions, an accurate compass and a DSU (Data Storing Unit) in which all data are stored. The cylinder and the fin are tied to a line through a flexible joint. The deep end of the line is moored to the bottom, and the shallow end is connected to a buoyancy element. There can be many instruments tied to one mooring, these will hang at different depths. Data from some SD Sensor data current instruments shall be employed, and these instruments work in principle in the same way as the RCM. These are all short term current meters when 20/10 minute sampling intervals are used. The sampling intervals are optional in these instruments.

2.1.2 RD Instruments, ADCP

The ADCPs use the well known Doppler effect that is observed when wave propagation is reflected from a moving target. The instrument sends sound pulses in a fan up

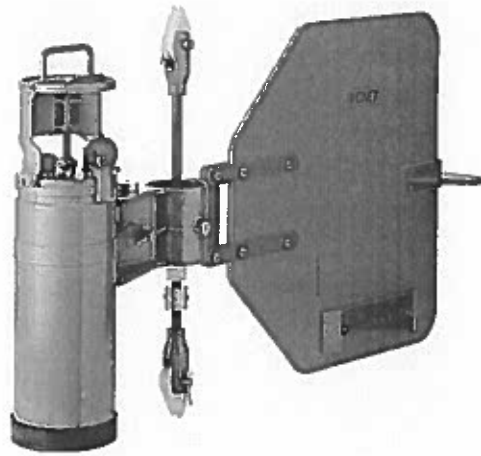Figure 2.4 The Aanderaa RCM-7 current meter, which is a newer version of the RCM-4 that has supplied our data. The fin that orientates the instrument toward the current and the propeller that finds current speed, are clearly seen.
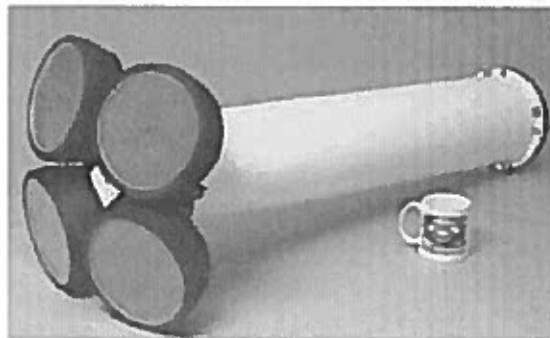

Figure 2.5 The Broadband ADCP, 75 kHz, which is put into a buoyancy module, and hangs in mid-depths. The four panels are the transducers, which send and receive sound pulses.

through the water column above it with a know frequency. These sound pulses get reflected by density irregularities, plankton and other particles and by receiving a frequency shifted signal, flow velocities are calculated. There are used bottom mounted instruments and instruments that hang at mid depth in a buoyancy module but they are all upward looking. The bottom mounted ones are of the type 150 kHz RDI Broadband, and the mid-depth are of the type 75 kHz RDI Broadband (see figure 2.5). These are all long-term current meters, supplying continuous data series of up to one year duration.

2.1.3 CTD

A sensor to measure Conductivity, Temperature and Pressure is lowered from a ship at certain positions along sections of interest and such *cruises* are done at regular time-intervals. One uses algorithms to find Salinity and Density from Conductivity and Temperature, and by use of the thermal wind equation, current velocities are calculated.

2.1.4 Overview of data

The section that shall be analyzed here is shown in figures 2.1, 2.2 and 2.3, and good coverage of oceanographic measurements spaced along this string, during 12-14 years are available. These data include regular CTD sampling from 1987 and up to present at 13 stations spaced 10 nautical miles apart, periods with short term current meters and bottom mounted ADCPs since 1994. This work began with a compilation of data, and all data that have been used shall be shortly mentioned here.

ADCP: In the Nordic WOCE and the VEINS project, ADCP's have been moored on the mentioned section, and data are collected and quality checked by the Faroese Fisheries Laboratory (FFL). The positions and observational periods are presented in table 2.1, and illustrated in figure 6.1, but the nomenclature for each record are not the same as used by FFL. Distances between the moorings are : $A \frown B \approx 23.4\ km$, $B \frown D \approx 5.0\ km$ and $D \frown C \approx 13.4\ km$. (Note that the order is not A,B,C and D, but C and D are swapped).

Current meters: SD2000 Sensordata (Gytre) and Aanderaa current data roughly along this same section (see figure 5.1), from two weeks in June 86, have been supplied by S. Østerhus at the Geophysical Institute in Bergen, and by B. Hansen at FFL. The section was more comprehensive than shown in table 2.2, but those not shown (mooring e, f and g) in the table are just briefly discussed in the text. The asterix $^{*)}$, indicates that the depth is not exactly known by the author, and distances between the moorings are : $a \frown b = 25.56\ km$, $b \frown c = 14.53\ km$ and $c \frown d \approx 13.42\ km$.

(To avoid confusion Aanderaa labels are shown in lower case letters (except in chapter five), while ADCP are in the upper case)

The part of the CTD stations along the section, which will be discussed here (the section extends to N013) is found in table 2.3. The positions, approximate depth, measurement period and number of successful cruises are shown.

Table 2.1   ADCP deployments along the section in the period October 1994 to July
1999.

Rec.	Position		Depth to		Int.	Observational period	
	Latitude , Longitude		Bottom , Instr.		min	yy/mm/dd	: days
A9601	62°42.37 'N , 6°05.31 'W		302m ,	301m	15	96/01/25-96/05/25 :	123
A9606	62°41.93 'N , 6°04.67 'W		292m ,	291m	20	96/06/17-97/05/21 :	340
A97	62°42.32 'N , 6°05.17 'W		300m ,	299m	20	97/06/15-98/06/08 :	359
A98	62°42.18 'N , 6°05.04 'W		297m ,	296m	20	98/07/08-99/07/01 :	360
B94	62°55.09 'N , 6°04.63 'W		963m ,	654m	5	94/10/23-95/02/16 :	118
B97	62°54.82 'N , 6°04.96 'W		925m ,	659m	20	97/06/14-98/06/12 :	365
B98	62°55.16 'N , 6°04.84 'W		961m ,	708m	20	98/07/05-99/06/18 :	349
C94	63°16.35 'N , 6°06.30 'W		1736m ,	616m	5	94/10/23-95/02/16 :	118
C96	63°16.08 'N , 6°06.51 'W		1738m ,	640m	20	96/06/17-97/05/21 :	339
C97	63°16.43 'N , 6°06.60 'W		1731m ,	659m	20	97/06/14-98/06/12 :	364
C98	63°15.94 'N , 6°06.30 'W		1739m ,	655m	20	98/07/06-99/06/18 :	349
D97	62°57.54 'N , 6°05.60 'W		1276m ,	670m	20	97/11/12-98/06/12 :	214

Table 2.2   The Aanderaa (and Gytre) moorings along the section in June '86.

Rec.	Position		Depth to		Int.	Observational period	
	Latitude , Longitude		Bottom , Instr.		min.	yy/mm/dd	: days
a1	62°27.00 'N , 6°10.10 'W		92m ,	43m	20	86/06/05-86/06/15 :	10
b1	62°40.60 'N , 6°09.60 'W		195m ,	45m	20	86/06/05-86/06/15 :	10
b2	62°40.60 'N , 6°09.60 'W		195m ,	95m	20	86/06/05-86/06/15 :	10
b3	62°40.60 'N , 6°09.60 'W		195m ,	170m	10	86/06/05-86/06/15 :	10
c1	62°48.80 'N , 6°07.70 'W		550*)m ,	41m	10	86/06/02-86/06/15 :	13
c2	62°48.80 'N , 6°07.70 'W		550*)m ,	90m	10	86/06/02-86/06/15 :	13
c3	62°48.80 'N , 6°07.70 'W		550*)m ,	292m	10	86/06/02-86/06/15 :	13
d1	62°55.40 'N , 6°05.80 'W		1200*)m ,	57m	10	86/06/02-86/06/15 :	13
d2	62°55.40 'N , 6°05.80 'W		1200*)m ,	110m	10	86/06/02-86/06/15 :	13
d3	62°55.40 'N , 6°05.80 'W		1200*)m ,	310m	10	86/06/02-86/06/15 :	13

Table 2.3   A part of the CTD section roughly along the same section in the period July '87 to June '99

Rec.	Position		Bottom depth	Observational period	
	Latitude , Longitude		m	yy/mm/dd	: cruises
N01	62°20.000 ′N , 6°05.000 ′W		∼70	87/07/05-99/06/14 :	51
N02	62°30.000 ′N , 6°05.000 ′W		∼100	87/07/05-99/06/14 :	52
N03	62°40.000 ′N , 6°05.000 ′W		∼220	87/07/05-99/06/14 :	51
N04	62°50.000 ′N , 6°05.000 ′W		∼540	87/07/05-99/06/14 :	51
N05	63°00.000 ′N , 6°05.000 ′W		>690	87/07/05-99/06/14 :	52
N06	63°10.000 ′N , 6°05.000 ′W		>690	87/07/05-99/06/14 :	44
N07	63°20.000 ′N , 6°05.000 ′W		>690	87/07/05-99/06/14 :	42
N08	63°30.000 ′N , 6°05.000 ′W		>690	87/07/05-99/06/14 :	42
N09	63°40.000 ′N , 6°05.000 ′W		>690	87/07/05-99/06/14 :	41

Chapter 3
THEORY

3.1 Important results from Oceanography

Before discussing slope currents, something general should be said about the driving agents that are believed to produce the current that we experience, and to make sure that we agree on some terminology used later. Background material for these considerations is found in Gill (1982), Pond and Pickard (1983), Kundu (1990) and Li and McClimans (1998, 2000).

3.1.1 Geostrophic Flow

In quasi-steady large-scale motions in the oceans, away from boundaries, one finds that an excellent approximation for the horizontal equilibrium is a balance, between the Coriolis force and the pressure gradient:

$$-fv = -\frac{1}{\rho_0}\frac{\partial p}{\partial x} \tag{3.1}$$

$$fu = -\frac{1}{\rho_0}\frac{\partial p}{\partial y} \tag{3.2}$$

Here, u and v are east-west current and north-south current velocities respectively, ρ_0 is reference water density and f is the Coriolis parameter given by $f = 2\Omega \sin\theta$, where again Ω is the angular velocity of the earth's rotation and θ is the latitude. Nonlinear acceleration terms and friction term are ignored and this is justified on such large-scale motions. This kind of balance where pressure forces are balanced by Coriolis forces, is called *Geostrophic balance.*

Velocities in a geostrophic flow are perpendicular to the horizontal pressure gradient. This is because (3.1) and (3.2) imply that

$$(\mathbf{i}u + \mathbf{j}v) \cdot \nabla p = \frac{1}{\rho_0 f}(-\mathbf{i}\frac{\partial p}{\partial y} + \mathbf{j}\frac{\partial p}{\partial x}) \cdot (\mathbf{i}\frac{\partial p}{\partial x} + \mathbf{j}\frac{\partial p}{\partial y}) = 0$$

Where i and j are unit vectors in the x and the y direction, respectively and the vertical velocities are negligible. Thus, the horizontal velocity is along, and not across, the lines of constant pressure.
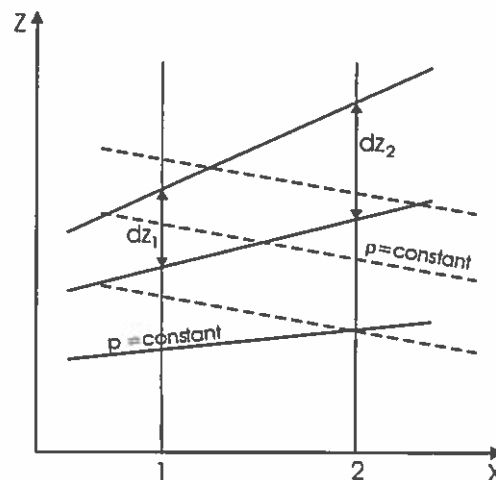
Figure 3.1   Sketch of circumstances that induce thermal wind.

To understand the physics one can think this way: Consider a horizontally converging flow in the surface layer of the ocean. The convergent flow sets up the sea surface in the form of a gentle "hill", with the sea surface dropping away from the center of the hill. A fluid particle starting to move down the "hill" is deflected to the right in the Northern Hemisphere (NH), and a steady state is reached when the particle finally moves *along* the isobars. It is this geostrophic assumption and the measurement of this "hill" that is the basis for the MAIA project.

3.1.2   Thermal wind

In the presence of a horizontal gradient of density, the geostrophic velocity develops a vertical shear, meaning that current velocity is a function of depth, $u = u(z)$.

Consider a situation in which the density contours (isopycnals) slope downward with x, the contours at lower levels representing higher density(figure 3.1). This implies that $\partial \rho / \partial x$ is negative, so that the density at 1 is larger than at station 2. Hydrostatic equilibrium requires that the weights of columns dz_1 and dz_2 are equal, so that the separation across two isobars increases with x, that is $dz_1 < dz_2$. Consequently, the isobaric surfaces must slope upward with x, with the slope increasing with height, resulting in a positive $\partial p / \partial x$ whose magnitude increases with height. Since the geostrophic flow is to the right of the horizontal pressure force (NH) we get velocities that increase with height.

From the geostrophic balance given in (3.1) and (3.2) in addition to hydrostatic balance

$$0 = -\frac{\partial p}{\partial z} - g\rho \tag{3.3}$$

we get, by eliminating p between (3.1) and (3.3) and also between (3.2) and (3.3), the current shear slopes

$$\frac{\partial v}{\partial z} = -\frac{g}{\rho_0}\frac{\partial \rho}{\partial x} \tag{3.4}$$

$$\frac{\partial u}{\partial z} = \frac{g}{\rho_0}\frac{\partial \rho}{\partial y} \tag{3.5}$$

respectively. These velocity gradients are the *thermal wind* named for the corresponding flow in the atmosphere where the density is a function of temperature, and it is a *baroclinic* phenomena since the lines of constant densities ρ and the lines of constant pressure p are not parallel. If the lines of equal density were level, there would be no velocity shear and an eventual current would be *barotropic*.

If the density field were known, we could, by integrating (3.4) and (3.5), find relative velocities for different depths, and additional knowledge of absolute current velocity at a reference point would determine absolute velocities in a line above and below the reference point. This is what is done with CTD measurements and the velocity profiles based on CTD-data that we present later will therefore be thermal wind profiles . The problem is a lack of reference points. To circumvent this problem one assumes that water masses in the deep layer have no velocities, which often is a good assumption. We will see that this indeed gives good results in deep water far from the continental shelf, but problems arise when approaching land.

3.1.3 Potential Vorticity Conservation

Expressed simply, *vorticity* is a characteristic of the kinematics of fluid flow which expresses the tendency of the fluid to rotate. The rotating earth gives fluids that are motionless in the earth's reference frame a vorticity f, the local planetary vorticity defined above. Any additional vorticity that stems from a fluids motion relative to the earth will be termed *relative vorticity* ζ. In Oceanography one is mostly interested in the vertical component of this vorticity. The vertical component is dominating over the two horizontal components because the horizontal scales of the oceans are so much larger than the depth. The vertical component is defined as:

$$\zeta \equiv \frac{\partial v}{\partial x} - \frac{\partial u}{\partial y} \tag{3.6}$$

The sum of planetary vorticity and relative vorticity $(\zeta + f)$ is called *absolute vorticity*, and if we divide this quantity by the thickness of the flow h we get the *potential vorticity* $pv \equiv (\zeta + f)/h$ for the flow. Assuming no friction and no vertical
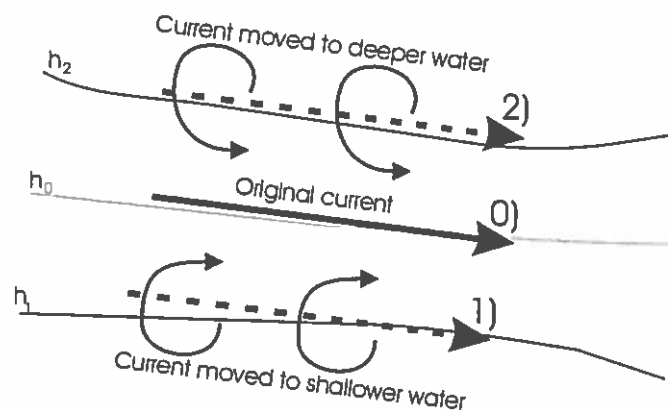
Figure 3.2 Sketch of a current jet with initially zero relative vorticity. Vorticity induced by depth-changes is shown.

velocity shear, one can, from shallow water eqn's of motion and continuity, derive a very important result for this potential vorticity:

$$\frac{D}{Dt}(\frac{\zeta + f}{h}) = 0 \tag{3.7}$$

The pv is conserved, from which the following conclusions can be made:

Vorticity is defined positive anti clockwise (cyclonic), and f is assumed to be a constant here. Now consider a current which flows along an isobath with depth h_0 with initially zero relative vorticity $\zeta = 0$. If this current, for some reason, is moved to follow a shallower isobath at depth $h_1 < h_0$, it must to obey (3.7) get a smaller absolute vorticity $(\zeta + f)$. f is a constant, forcing ζ to be smaller. The relative vorticity ζ, which initially was zero, must therefor become negative and we have a clockwise, or anticyclonic rotation of fluid parcels, as shown in figure 3.2

The conservation of pv will in a way resist that the current is moved, and tries to maintain the original flow. The situation is reversed if the current jet is moved to deeper isobaths at depth h_2, shown with arrow number two in the sketch. A cyclonic vorticity is induced, which again tries to restore the original flow pattern. This is believed to be the main agent in what we know as *topographic steering*.

3.1.4 Forcing agents

Before trying to estimate the amounts of water that flow north to the Arctic, some word should by said about the driving forces of this current. When water enters very cold regions like the Arctic or Antarctic, it gets cooled down, its density increases and it begins to sink down into the abyss. It creates a "push"on the deeper water layers forcing these to flow toward the equator, and this is the flow referred to as *Outflow* from the Nordic Seas. At the same time this increased density creates a

downhill "suction" on more shallow water masses, pulling these toward the poles. The entire process is referred to as *Thermohaline circulation* and is believed to work as the "heart" of global ocean circulation.

On a smaller scale, wind exerts friction on the ocean surface, inducing water mass transport. It can be shown (Gill) that surface transport induced by wind is 90 degrees to the right of the wind direction on the NH. This means that northward wind along a western coast in the NH will "push" water towards land forcing a water level increase. This increase will be part of what we referred to as a "hill" in section 3.1, and the wind has thereby induced a flow going northward. The Faroe Islands lie on, what meteorologists refer to as a "Highway of polar lows", and the most dominant wind direction is southwesterly, meaning that the wind comes from the southwest. Orvik et al. (2000) show strong correlation between the eastern branch of the NAC and the low pressures.

On even smaller scales, theory shows that a significant contribution to currents near bathymetric irregularities and banks comes from *Tidal rectification*. Tidal rectification is a purely nonlinear and frictional effect where the sloshing of tidal oscillation and the effect of the Earth's rotation result in a clockwise circulation around banks in the NH. Loder (1980) shows tidally rectified currents in the range 0.2-0.3 m/s along the northern slope of Georges Bank, and the variations in this current are closely correlated with variations in the amplitude of the tidal current.

3.2   Tidal currents

Tides are experienced as a movement of the sea surface up and down, and few people think of this phenomena as waves but it indeed is. The astronomical bodies (mostly the moon) induce by their gravitational pull, a large wave that moves across the oceans with a dominating period of 12.5 hours. These waves resemble normal ocean waves in shallow water if we imagine these in very slow motion, and most of us have experienced that there is an oscillatory water movement in waves.

Without going into to much mathematics, we can present the Shallow Water Equations which are derived from continuity and momentum equations and where friction and nonlinear terms are neglected.

$$\frac{\partial \eta}{\partial t} + H\left(\frac{\partial u}{\partial x} + \frac{\partial v}{\partial y}\right) = 0$$

$$\frac{\partial u}{\partial t} - fv = -g\frac{\partial \eta}{\partial x} \qquad (3.8)$$

$$\frac{\partial v}{\partial t} + fu = -g\frac{\partial \eta}{\partial y}$$

η is the water elevation, H is a constant mean water depth, u(x,y) and v(x,y) are vertically averaged velocities and g is the acceleration of gravity. The main difference between tidal waves and normal gravity waves is that the tidal waves are so large in the horizontal direction that they 'feel' the rotation of the earth and this is not the case with normal ocean waves. This means that we must retain the Coriolis parameter f in a derivation of eqn's of motion and this will make the water parcels move in elliptical trajectories instead of just back and forth. The excursion of water parcels is on the order of 5 km, and f is assumed to be constant here (f-plane).

Consider progressive waves of the form

$$(u, v, \eta) = (\widehat{u}, \widehat{v}, \widehat{\eta})e^{i(kx+ly-\omega t)}$$

where $\widehat{u}, \widehat{v}$ and $\widehat{\eta}$ are complex amplitudes, k and l are wave numbers in east-west and north-south direction respectively, ω is wave frequency and the real part of the right side is meant. Then 3.8 gives

$$-i\omega\widehat{u} - f\widehat{v} = -ikg\widehat{\eta} \tag{3.9}$$

$$-i\omega\widehat{v} + f\widehat{u} = -ilg\widehat{\eta} \tag{3.10}$$

$$-i\omega\widehat{\eta} + iH(k\widehat{u} + l\widehat{v}) = 0 \tag{3.11}$$

Solving for $\widehat{u}$ and $\widehat{v}$ between (3.9) and (3.10), we get

$$\widehat{u} = \frac{g\widehat{\eta}}{\omega^2 - f^2}(\omega k + ifl) \tag{3.12}$$

$$\widehat{v} = \frac{g\widehat{\eta}}{\omega^2 - f^2}(\omega l - ifk) \tag{3.13}$$

Tidal waves are gravity waves that are affected by Coriolis force and such waves are also called *Poincaré waves, Sverdrup waves* or simply *rotational gravity waves*. From the dispersion relation (not shown) of these waves one can see that the wavefield doesn't feel the x and the y direction differently, and this horizontal isotropy is a result from treating f as a constant. Let us for simplicity assume the sea surface elevation is given by

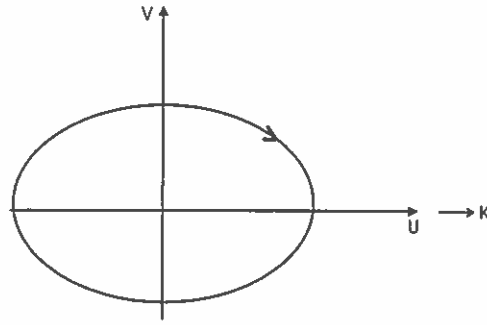$$\eta = \widehat{\eta}\cos(kx - \omega t)$$

Figure 3.3   u,v-plot (hodograph) of a tidal wave propagating eastward. An orientation of rotation is indicated.

where $\widehat{\eta}$ is real. By multiplying (3.12) and (3.13) by $\exp(ikx - i\omega t)$ and evaluating the real part of both sides gives finally

$$u = \frac{\omega\widehat{\eta}}{kH} \cos(kx - \omega t) \tag{3.14}$$

$$v = \frac{f\widehat{\eta}}{kH} \sin(kx - \omega t) \tag{3.15}$$

We have now found expressions for east-west and north-south velocities for a tidal current, where the tidal wave propagates to the east on a flat bottom of depth H. A hodograph, which is a u,v-plot, of these two velocity components gives a current tidal ellipse (figure 3.3).

3.3   Eliminating tidal currents

The fast track current jet is from theory assumed to be quite narrow and to have a much larger velocity than the surrounding waters. This jet-core is not stationary, but is regularly oscillated up and down the shelf with the tidal current, and other more stochastic perturbations like large meanders will also disturb this jet additionally. One aim of this work is to look at the character of this jet, in short time intervals at a time and the primary motivation for looking at this variability was to follow up the work of McClimans and Lønseth (1984) for an oscillating front. They were able to remove inertial oscillations, which have a circular nature, from data. The idea here is to use the same approach, but instead of removing a circular signal we shall try to remove the somewhat more complicated tidal ellipse. A current meter measures absolute current and direction and is not able to distinguish between the currents, and we must therefore try to eliminate the distortions that are unwanted. Since we

are at short time scales at a time, say two days or less, large and slow meanders will seldom give any larger effect, and we therefore focus on removing the tidal currents.

We must find tidal current ellipses at each mooring position, and must therefore resolve tidal current variations down to a 15 km horizontal length scale, because this is the order of the separation between moorings. The existing current maps are far to coarse for our purpose and other solutions must be found. The problem is approached this way: A barotropic tidal current model has been used which has a resolution of 10 km, and the closest grid point to the wanted location will thereby be nearer than this distance. This model is compared to year long ADCP time series.

3.3.1 Time series from model

A barotropic model is developed at the Faculty of Science and Technology, University of Faroe Island, by Knud Simonsen (private communication). The model is based on the depth integrated hydrodynamic equations, which in a Cartesian system with horizontal x, y, z and the corresponding volume transports (U, V) may be written:

$$\frac{\partial U}{\partial t} + \frac{U}{h}\frac{\partial U}{\partial x} + \frac{V}{h}\frac{\partial U}{\partial y} - fV = -gh\frac{\partial \eta}{\partial x} + A_x + B_x \qquad (3.16)$$

$$\frac{\partial V}{\partial t} + \frac{U}{h}\frac{\partial V}{\partial x} + \frac{V}{h}\frac{\partial V}{\partial y} + fU = -gh\frac{\partial \eta}{\partial y} + A_y + B_y \qquad (3.17)$$

where A_x, A_y are the components of the bottom friction, and B_x, B_y are the components of the lateral friction. The equation of motion has been discretized on a space-staggered C-grid using a forward-backward scheme. The advective terms are implemented by a forward centered scheme which is known for its high diffusivity. The model is implemented using a Mercator projection relative to the 7° W meridian (from K. Simonsen). Boundary values are taken from distant regions. They do not include any residual currents in the calculation region, and this suites us fine, since we want to remove the tidal data only. Having seen this model demonstrated at the Faroese Fisheries Laboratory during the MAIA meeting 2/5-5/5 this year, I feel that this might be the best way to estimate the wanted current ellipses. The model gives us the eight tidal constituents: $M_2, S_2, K_1, O_1, P_1, K_2, N_2$ and Q_1. For each constituent, semi-axis amplitudes of a current ellipse and its inclination to the east-west axis is given and, of course, also the Greenwich phase lag. The definition of all parameters are given in the sketch in figure 3.4.

The orientation of rotation is clockwise, and the phase lag is relative to the ellipse major-axis end that lies above the east-west line. Two time series are generated for each constituent in the ellipse reference frame. One along the minor semi-axis called v^e and one along the major axis called u^e, where the superscript 'e' indicates that these time series are in the ellipse reference frame.

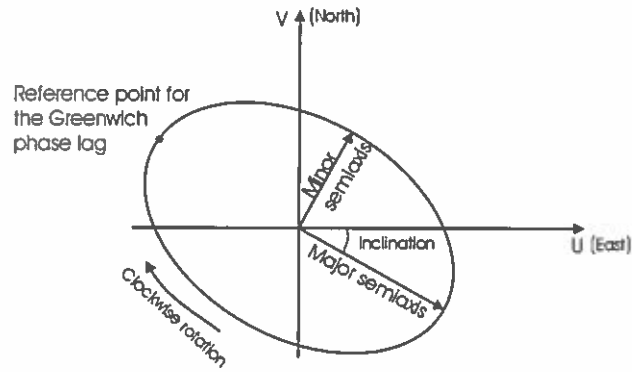$$v_i^e = V_i \cos(\sigma_i t - v_{0i}(t) + g_i) \qquad (3.18)$$

Figure 3.4 Parameters of the tidal allipse for a given constituent. The reference point for the Greenwich phase lag is always chosen to be above the east-west axis.

$$u_i^e = U_i \cos(\sigma_i t - v_{0i}(t) + g_i) \tag{3.19}$$

U_i and V_i the amplitudes given by the model, σ_i are frequencies that are tabulated to great accuracies for all tidal constituents, g_i are the Greenwich phase lags that give the time relation between climax of a constituent at a given site and when its driving force crosses the Greenwich meridian. e.g. the relation between the climax of M_2 and the time when the moon stands over the $0°$ meridian. The $v_{0i}(t)$ phases depend on the choice of zero time in the generated time series, and give the positions of the astronomical bodies at this time. A software program, based on the work of Schwiderski (1980), (private communication with Martin Mathiesen at SINTEF), was used to find these phases and the start time was chosen to be 12/11-1997: 00.00, because at this time all four ADCP moorings are sampling.

The individual current ellipses are finally transformed to the east–north reference frame, with the linear transformation

$$\begin{bmatrix} u_i \\ v_i \end{bmatrix} = \begin{bmatrix} \cos(\alpha_i) & \sin(\alpha_i) \\ -\sin(\alpha_i) & \cos(\alpha_i) \end{bmatrix} \cdot \begin{bmatrix} u_i \\ v_i \end{bmatrix}^e, \tag{3.20}$$

where α_i is the inclination to the east-west line for constituent 'i'. The tidal currents in north-south and east-west direction u and v, respectively are now found by summing the individual contributions

$$u = \sum_{i=1}^{8} u_i \tag{3.21}$$
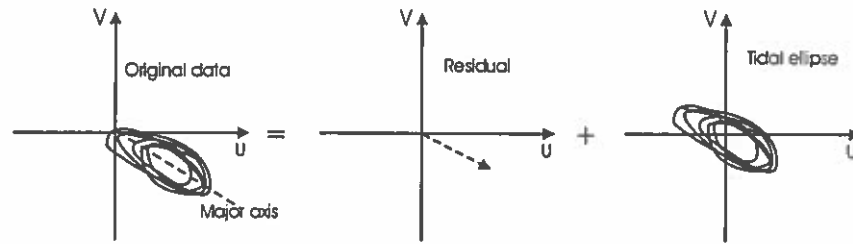
$$v = \sum_{i=1}^{8} v_i \tag{3.22}$$

Figure 3.5   Sketch of assumption. Data are composed of a residual and a tidal ellipse

3.3.2   Profile gradient

The basic assumption in this analysis is shown in figure 3.5. The original current velocities observed are assumed to be composed of a current jet which steadily follows the isobath directions, and a disturbing tidal current. It is of interest to find the geometrical profile of this residual in a plane perpendicular to its flow direction and to find the average position of this profile peak. The only way to determine the main flow direction, is to find a major axis from the hodographs as shown in the sketch. But this would give individual profiles for the different current meters because flow directions are slightly different at each site and this will complicate the analysis considerably. An attempt to look at each site individually shall be mentioned, but we shall now describe how this analysis is done in the north-east Cartesian frame. The isobaths in the measurement section are oriented about 15° south of east as mentioned, and a uniform analysis will therefor give profiles closely resembling the cross-isobath ones. We shall stay in the original frame when annually averaged data are considered in chapter 7, and an unified analysis here is the best.

The east-west current component of the residual current shown in the middle window in figure 3.5, is given as

$$\widehat{u} = u_{\text{data}} - u_{\text{model}} \tag{3.23}$$

and this should be oscillating with tidal frequency. But this tidal "amplitude" is not caused by the tidal current directly, but indirectly since it is the tide that perturbs the residual jet itself. This jet will have a geometrical distribution, and looking from east to west, one could imagine a profile as drawn at different times in figure 3.6.

The figure shows one half tidal cycle, beginning with the left most instantaneous profile and proceeding to the right. If we plot the signal which an instrument placed at the origo in upper the window measures against the position of the traversing jet, we will get a plot as shown in the lower window. The position of the traversing jet is found as the time-integral of the north-south current velocity v

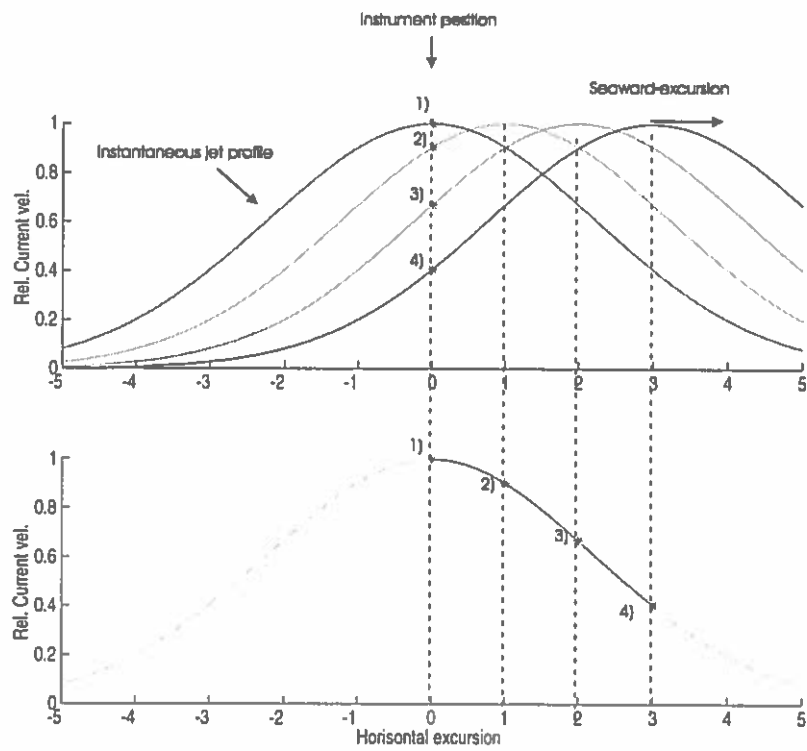$$y(t) = \int_{t_0}^{t} v\,dt. \tag{3.24}$$

Figure 3.6   Illustration of how the jet will oscillate with the tide, and how an instrument placed as shown will measure this traversing current.

This plot will in reality be more like a straight line, because the aspect ratio jet-width/tidal excursion is much larger than shown and what we find is therefore a tangent at the place where the instrument is moored. If the analysis is successful, one should, with the help of many instruments at different places, be able to find many tangents from which one could draw conclusions on the jet-profile itself. The width of the jet-profile is not known, but is assumed to be 10 - 15 km and should be varying. We find from data that tidal traversing typically lies around 2.5 km giving us an aspect ratio of 4-6. The traversing coordinate y, is in the north-south line (positive north), and not in the cross isobath direction. The volume flux is calculated from current speed multiplied by the sectional area A, $Flux = u \cdot A$. If we decompose on the major axis inclined at an angle θ to the east-west line, we find directions of maximum speed but the cross-sectional areas will be multiplied by a factor $\cos(\theta)$ relative to area sections in north-south plane A_{n-s}, $Flux = u_{max} \cdot (A_{n-s} \cos(\theta))$. If we stay in the original-frame this cosine factor will appear in the velocity instead, giving the same result, $Flux = (u_{max} \cos(\theta)) \cdot A_{n-s}$. Staying in this original frame will make the tidal traversing method somewhat more confusing, because the residual of v is not zero (as it would be in a cross-isobath frame)and the time integral of v will therefor give an tidally oscillating signal plus a movement caused by the residual. This movement will make the profiles that we obtain (see lower window in figure 3.6), move over periods longer than the tidal period.

A similar analysis was done with Aanderaa data. The main differences are : The tidal ellipse was found as a modified average between adjacent moorings (before I knew about the model), current values were decomposed on the major axis (figure 3.5, left window) so that $v \rightarrow v^t$ and $u \rightarrow u^t$, where superscript 't' stand for values transformed into the major-axis frame.

3.4 Narrow instantaneous jet in a wider averaged jet

The reason for working with high-resolution time series (10-20 min. sampling period) is to find the character of an instantaneous high-velocity current as discussed. This is interesting from a theoretical point of view, and also when we measure phenomena that occur on short time scales. However, if the purpose is to find monthly or yearly average current fluxes, this complicated and data-demanding analysis might be superfluous. We know from the *Central Limit Theorem* in statistics, that a sum of stochastic variables will approach a normal distribution when the number of variables gets large enough. Let us now consider the instantaneous jet profile given as a function $f(y,t)$ which is assumed to be a symmetrical function around a mean y_0. This profile will fluctuate up and down the shelf slope with a tidal frequency, so if we average over a tidal cycle, this will give us a somewhat lower and broader profile $\overline{f(y,t)}$ where the overbar denotes averaging over 12.5 hours. This is still a function of time on larger time scales and this time dependency will be caused by meanders, Rossby waves and other stochastic phenomena. It will therefore be a natural assump-
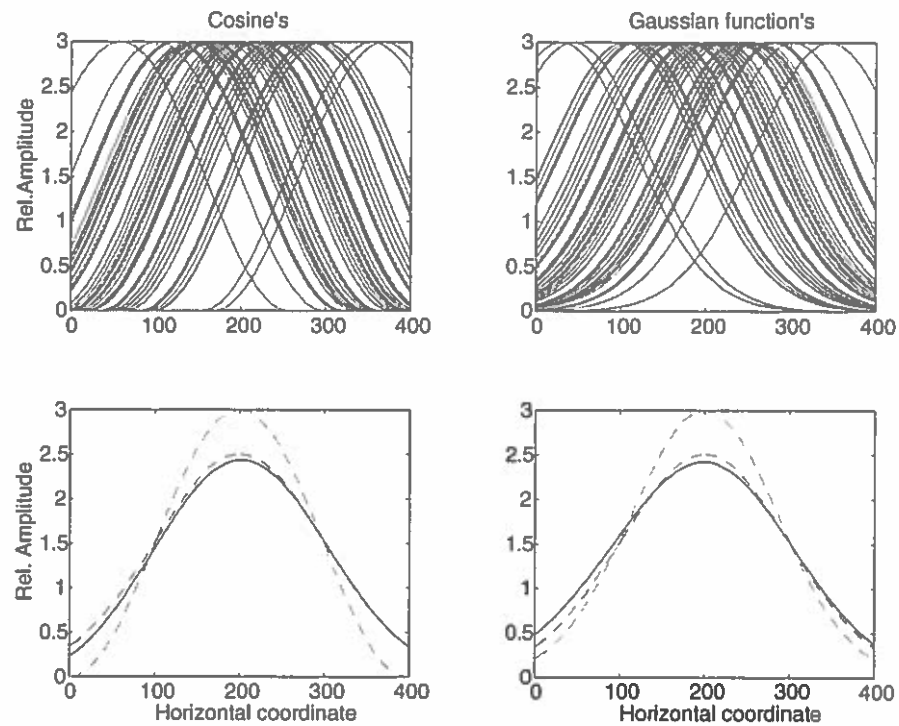
Figure 3.7   A simulation of oscillating cosine- and Gaussian functions. Their mean are assumed to be stochastic variables, and the upper windows show 52 realizations. The higher dashed curves in lower windows are original functions (with mean=200), the lower dashed are all 52 realisations averaged and the full line figures are Gaussian functions for comparison.

tion that the time dependency is introduced in a mean $y_0(t)$ which is a stochastic variable, and express the profile as

$$\overline{f(y,t)} = g(y - y_0(t)) \tag{3.25}$$

We have done this in figure 3.7, and a simulation is done for $g(y - y_0(t))$ given as a cosine- and a Gaussian function. In the lower windows we see an average over 52 such realizations, and this approaches a steady normal distribution when the number of realizations increases, much in accordance with the Central Limit Theorem, although this is for functions and not just scalar variables. The two different symmetrical jet-profiles $g(y - y_0(t))$ are simulated to illustrate that the mean is Gaussian even though the initial jet-form is somewhat arbitrary.

This tells us that an analysis with ADCP data with a 20 min time resolution, and an analysis with annual averages will give two different profiles. The slopes found

from the fine resolution analysis will be steeper than the ones found from the coarser data, and a natural choice for the y dependency of the annually averaged profile would be a normal distribution.

Chapter 4
TIDAL ELEVATION IN TÓRSHAVN

Since the aim with MAIA is to use coastal water level measurements to predict total inflow over the Iceland-Shetland ridge, a short review of the water level characteristics in Tórshavn is in place

4.1 Short introduction to the basis of MAIA

The large time and space scales considered are believed to support the use of a simple geostrophic balance. Data seem to indicate that the sea-level rise propagates along coasts as barotropic Kelvin waves (McClimans et al. 1999), which again will establish geostrophic balance within a few days. A good correlation is found between five day averages of sea-level data and current velocities along the Norwegian continental slope. The measured water level in Tórshavn , ζ_T above a chosen reference level ζ_0, is a sum of the different contributions:

$$\zeta_T = \zeta_{BT} + \zeta_{BC} + \zeta_{FCC} + \zeta_{AP} + \zeta_{SH} + \zeta_W \qquad (4.1)$$

where ζ_{BC} = baroclinic rise, ζ_{BT} = barotropic rise, ζ_{FCC} = rise due to the barotropic Faroe Coastal Current, ζ_{AP} = rise due to atmospheric pressure, ζ_{SH} = Steric Height which is a rise caused by brackish water with lower density near the coast (see figure 4.1) and ζ_W = wind effect on sea level.

Comparing data from a standard CTD section crossing the Faroe Bank Channel, with data from a coastal salinity station which has been sampling twice a week for nearly three years, we see that the water is consistently fresher near land. But a strong tidal mixing (mixing effect of tidal currents) on shallow water keeps the shelf water colder than the surrounding sea. By using averaged seasonal temperature differences between the shelf and deep water, together with salinity and then calculate water densities, reveals that the water is slightly denser near land, and no appreciable steric anomaly is expected. This result is in contrast to the Norwegian coast, where large steric anomalies are found. This allows us to neglect the effect of the steric height, $\zeta_{SH} = 0$. The effect of Atmospheric pressure ζ_{AP}, the inverse barometer, is removed with data series of air pressure in Tórshavn. By assuming that each millibar corresponds to a centimeter decrease in water level, we can simply add the two time series. No wind-data is available at present, but data do exist and should be interpreted in this analysis.
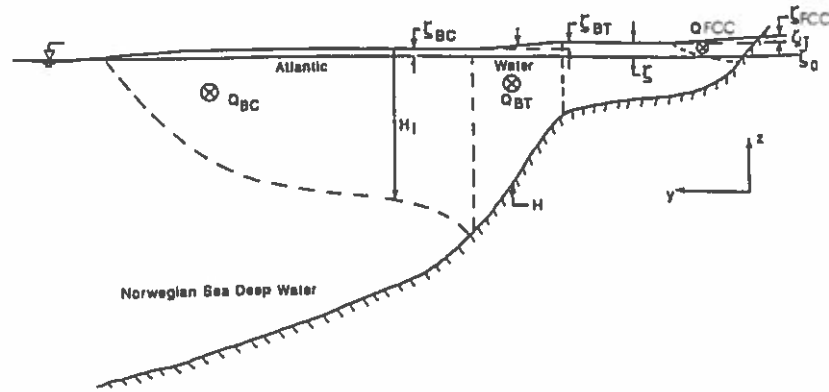
Figure 4.1 Cross section of the geostrophic balance in the long-slope currents. BT and BC indicate barotropic and baroclinic respectively. FCC stands for Faroe Coastal Current and the $\zeta's$ are water elevations. (Adapted from McClimans et al. (1999) for the northern shelf of the Faroe Islands)

Some more assumptions must be made in order to establish an algorithm between tidal data and volume flux. In theory, barotropic and baroclinic transports are given by (McClimans et al. 1999)

$$Q_{BT} = \frac{gH\zeta_{BT}}{f} \qquad (4.2)$$

$$Q_{BC} = \frac{g^2\zeta_{BC}^2}{2g'f} \qquad (4.3)$$

respectively, where H is the average depth of the core of the barotropic current and $g' = g(\rho - \rho_0)/\rho$ is reduced gravity. If we have made all the corrections right, that is completely removed air pressure effect, wind effect and possibly other effects, and if the assumptions, that no steric height exists and no effect is felt from the barotropic coastal current, hold, then the measured sea-level is given by $\zeta = \zeta_{BC} + \zeta_{BT}$. Computations of the total transport require now the constraint

$$Q_{BT} = KQ \qquad (4.4)$$

McClimans et al. (1999) choose $K = 3/8$ for the NAC and end up with the algorithm

$$\zeta = Q^{1/2}/11 + Q/90 \qquad (4.5)$$

that relates coastal water level to the total transport of water, for which ζ is in m and Q in Sverdrups ($Sv = 10^6 m^3/s$).

4.2   A look at the data from Tórshavn

MAIA will rely on specific main tide recording stations in different countries and Tórshavn is the one chosen in the Faroes. We have water-level data from Tórshavn in the period 1991-2000 which are sampled with an hourly interval. Some holes with missing data exist, but the series is quite continuous. Pressure data from 1993 exist as well with a more random sampling interval (3 or 6 hours). Firstly there are made time series which contain daily averages for water-level (from 00 to 23) and for air pressure (as well as one could cover a day). Then there are made routines in Matlab®, which pick out data from chosen time-intervals, average these over an optional number of days and correct the water-level with air pressure ζ_{corr} [cm] $= \zeta_{measured}$ [cm]$+airpress$ [$mBar$] (see example of correction in figure A.25). Hansen (1975) analyzed almost one year (1973) of sea-level data from Tórshavn with a Maximum Entropy Method (MEM). The conclusions were that some higher harmonics appeared in the tide, and this was assumed to stem from local non-linearities due to frictional effects in the current, the socalled shallow water harmonics. The non-harmonic part of sea level fluctuations was very well explained by the air pressure variations, although the sea was not found to be able to respond to rapid pressure fluctuations. The wind had therefore minor effects and the many-day averages will certainly remove the probable wind effect ζ_W, and also remedy the sea-level lag when the pressure variations are too rapid. These data shall be compared with the currents later.

Chapter 5
AANDERAA DATA

A string of current meters was deployed for two weeks in June 1986 to the north of the Faroe Islands as shown in figures 5.1 and 5.2 (Hansen et al. 1986). The dots indicate moorings and each mooring contained one to four instruments placed at different depths. Most instruments were Aanderaa RCM-4, which we introduced in section 2.1.2, but the two sites closest to land had three of the somewhat cheaper and therefor less reliable SD 2000 Sensor instruments. These give data series similar to the Aanderaa. Two weeks is a fairly short measurement period, but the area is heavily fished and the risk of loosing instruments in fishing nets is large. The limited storage is also a limitation when such instruments are used with short sampling periods.

The Aanderaa data have a 10 min. sampling interval, and include temperature, absolute current speed (magnitude) and current direction. Some have salinity and pressure, but since these parameters are not common to all, and do not show any appreciable variability, they will be disregarded in the analysis. The SD Sensor data have a 20 min. sampling interval, and have only current magnitude, direction and temperature measurements. East-west and north- south current velocity u and v respectively, were included in all data series, and error codes '-999' were removed with linear interpolation. No long patches with error coding occurred, so the interpolation should be justified. All parameters were plotted on the same diagram, for each individual instrument, to get an overview of the data. These plots illustrate clearly how different signals show through the various parameters (figures 5.3 and 5.4).

For some series clear non-physical measurements were seen, especially in the beginning or the end of the time-series. These anomalies stem probably from the mooring process itself, and are excluded from the data-analysis. Note that this chapter shall refer to Aanderaa (Sensordata) with upper case letters!

5.1 Jet profile analysis

The technique that we described in section 3.3.2, requires that quite clear tidal signal is in the data we analyze, because the cross isobath coordinate y is found by integrating the cross isobath current, which is assumed to be purely tidal. We are therefore mostly interested in signals with tidal frequencies and thus restrict our analysis to the
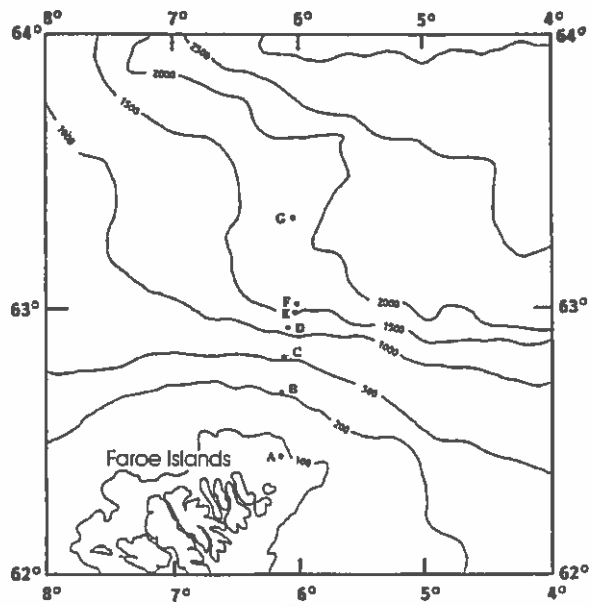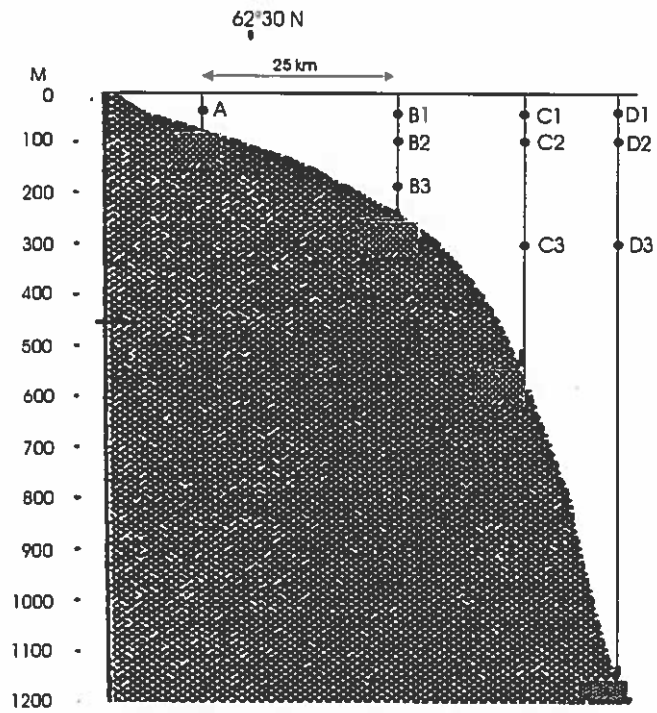
Figure 5.1   All Aanderaa moorings, June 1986.

Figure 5.2   A westward look at the innermost instrument postions A,B,C and D. The lines indicate the mooring lines, and the Faroe shelf is shown. Row one is shallowest and row three is the deepest.
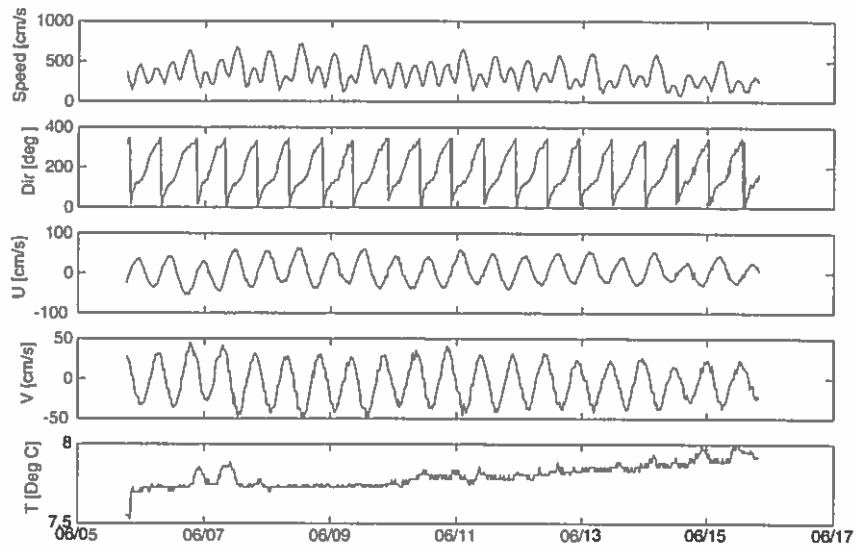
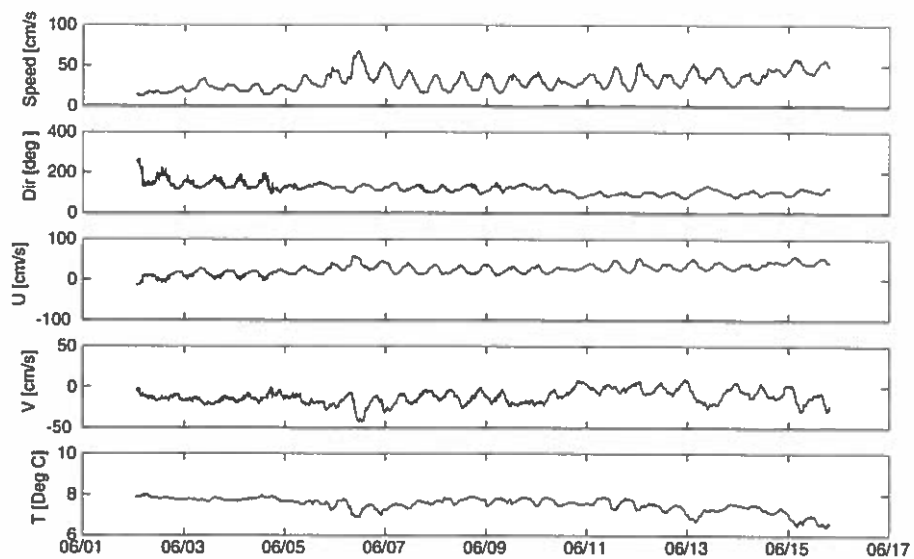Figure 5.3 All parameters for A (z=43m), in the period 6/6- to 16/6-86. (Note American date notation)

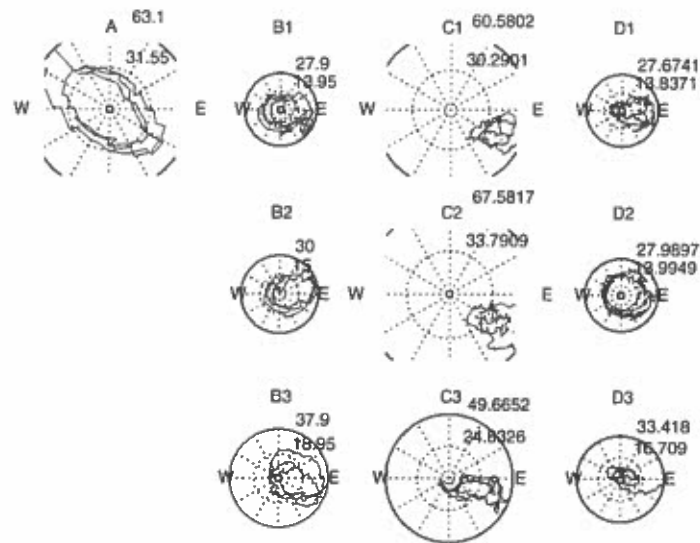Figure 5.4 All parameters for C2 (z=90m) in the period 2/6- to 16/6-86.(Note American date notation)

Figure 5.5 Hodographs (u,v-plots) for a chosen period lasting approx. 35 hours. The plots are shown as in the measurement section viewed from east to west. A is closest to land, D is farthest away, A1, B1 and C1 are at equal depths, and depth 1 is shallower than depth 3. Numbers give max. current magnitude for the period in cm/s.

moorings A, B, C and D (see figure 5.1). Farther seaward these signals get blurred and weak, and are therefore not suited for such an analysis. Another argument for a limited analysis is that we, from theory and experience, expect the shelf guided jet-core to be in waters shallower than one kilometer. Work has been done on all data series, but it is not found necessary to include all of them in this paper.

All mechanical current meters (Aanderaa and Sensordata) that will be discussed are shown in figure 5.2.

In the subsequent analysis, running averages over three data points are applied when this is found necessary for clarity. This means an average over half an hour for Aanderaa data, and one hour for Sensor data which is closer to an acceptable limit when looking at tidal frequencies. To get an idea about the rotary motion of the currents, hodographs, were plotted for entire series, and for different 'nice' parts of the data (figure 5.5).

Feather plots, which are vector plots of current speed (magnitude, see figure 5.6) as a function of time, give a qualitative picture of the current rotation and we see that site A shows clockwise rotation, and this fact is common for all measurements.

We now have current data in the east-west and north-south directions, and a routine which finds major axis is made in Matlab®, and we are ready to apply the method described in section 3.3 to a sample of data. A period lasting 35 hours,
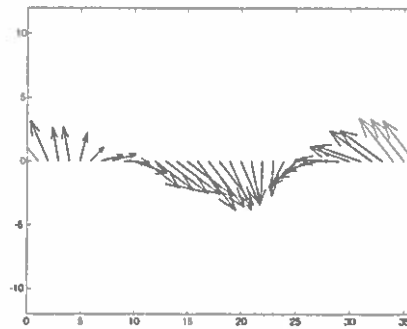
Figure 5.6   A feather-plot for mooring A. The arrows show qualitatively how the current vector rotates with time. (Clockwise rotation)

which showed fairly good data from all moorings is chosen to illustrate the method. As we see in the hodographs in figure 5.5, smooth characteristics are expected from site A, but the rest is, like real data often are, rather chaotic. In figure 5.7, we see east-west and north-south current velocities u,v and their transformed counterparts for this short period. A correct transformation to the major axis would render a zero cross slope current residual v, shown in green, and it is especially clear in C1 how the v-oscillation is moved to oscillate around zero, and the effect of the running average is also evident. After finding the major axis, common tidal ellipses between adjacent moorings and subtracting, we produce profile plots shown in figure 5.8.

5.2   Short discussion and critics

If we take a look at the hodographs again, we see that the ellipses for A and C, are much larger in magnitude than the one for B, and while the former show a quite stable character, the hodograph at B shows smaller current magnitudes and a more disoriented nature. One can deduce that the assumption of a common tidal ellipse fails.

5.3   Different application

Let us just make a short temperature observation, to see how this tidal-traversing method can be used differently. Most measurement locations did not show any appreciable variation in temperature with tidal frequency. We do have some larger drift over days at some sites, which could be interesting to analyze, thinking about larger meanders coming in against the shelf or other effects, but that is not the topic here. All measurements fairly close to the bottom show uniform temperature indicating tidal-mixing of waters. We show here only the data that show a tidal variation, which are the shallower and farther-from-land locations C1, C2, D1 and D2. In figure 5.9 we have, in the upper row, transformed cross-shelf velocity (full line and to scale)
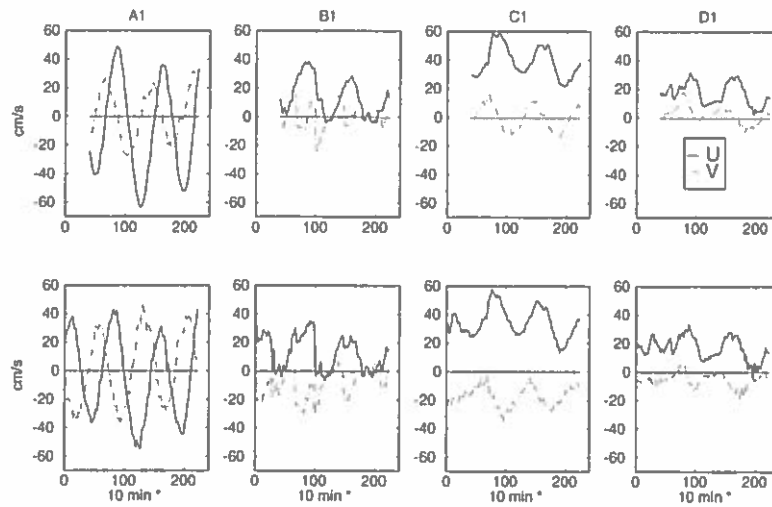
Figure 5.7 Current components u (full line) and v (dash-dot) in a chosen period for the shallowest depth 1. Lower row shows east-west and north-south components, and the upper row shows currents decomposed on each local major axis.
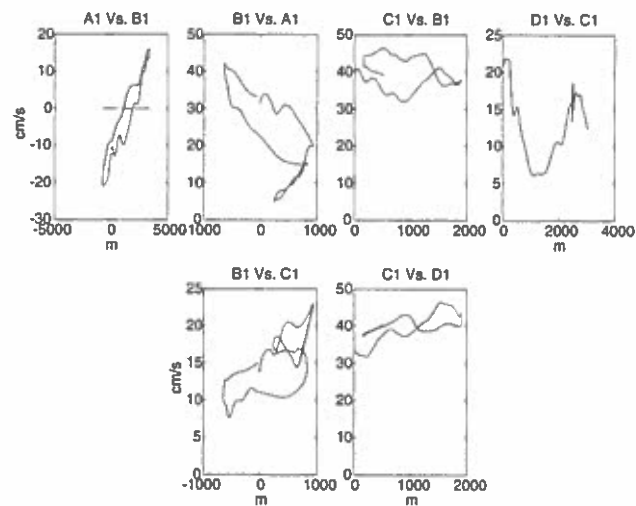

Figure 5.8 Residual along-slope currents for depth 1 (the shallowest), as a function of cross slope excursion y. We need two rows because the 'background' tidal ellipse for say B is found between B,A and B,C.
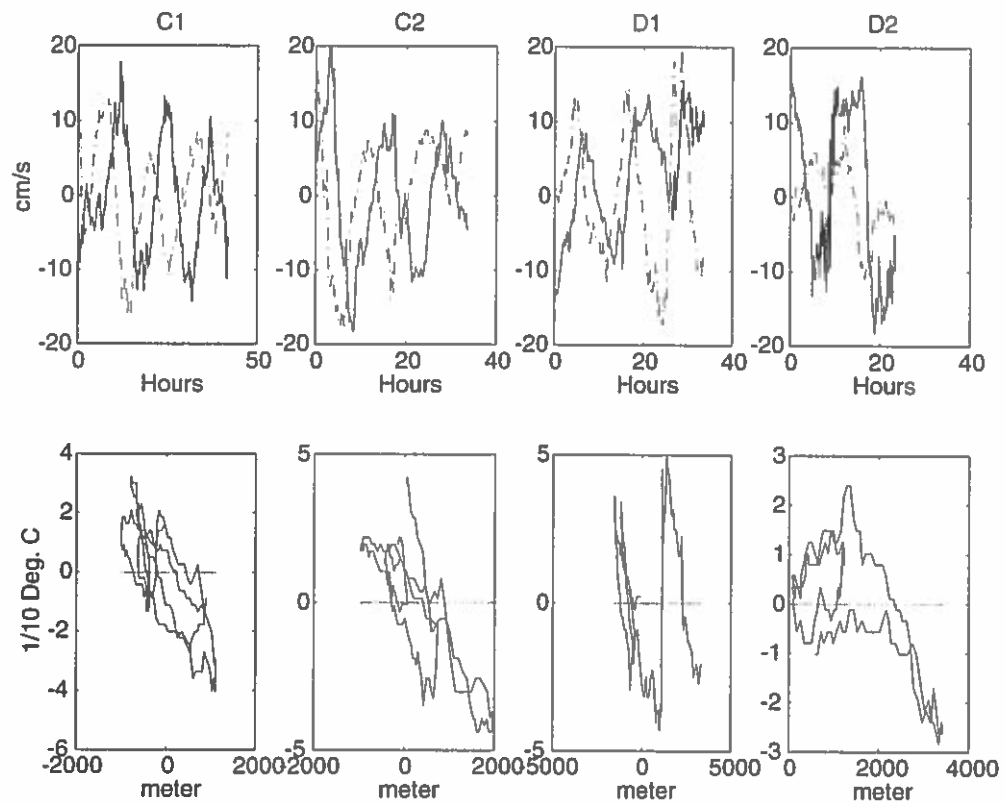
Figure 5.9 Temperature T as a function of cross-isobath excursion y, which is positive seawards. The upper row shows cross isobath current velocities v (full line) and temperature T (dash-dot). The lower row shows temperature changes for the traversing water. A negative slope indicates a lower temperature on the shelf.

versus temperature (dashed and not to scale).

One confirmation of a correct transformation is that while the north-south component does not show any reasonable correlation with temperature, the transformed do. We see that the temperature goes from increasing to decreasing at the exact instance when the current has zero velocity, meaning change of direction of water flow. Plotting temperature as a function of lateral coordinate, shows a linear decrease of temperature when the flow goes seaward (lateral coordinate positive seaward). This implies that colder water is traversing the instrument, and hence that the shelf has colder water than the surrounding waters. The periods chosen (the graphs are not synchronized), are the ones with the greatest temperature variability, and we find temperature differences of almost one degree centigrade in waters only 2-3 km apart!

5.4 Average character of the data

The traversing method is a search for the jet-profile that was referred to as instantaneous high-velocity profile in section 3.4. In order to get a picture of the time averaged wider and lower profile, we take the average of the two components of current velocity for all data from June '86, and plot these averages as functions of the different instrument depths. The east-west profiles are shown in figure 5.10, for all moorings. The highest velocities occur at mooring C which is approximately on the 550 m isobath. There is a quite strong vertical velocity shear at this site, and a similar shear is seen at mooring D, which has somewhat lower velocities. Mooring B (195m) had again lower velocities but the velocity profile seems to be more uniform, and mooring A (95m) with only one instrument had even smaller residual current velocities. Mooring E, F and G show a more odd character with a back-flow at F, very small flow velocities at E and a more regular flow at G. A larger meander probably entered the section in this period as also seen from CTD-data at the same time (Hansen et al., 1986), and the strange appearance is due to this. An interesting feature is that velocities seem to be smaller close to the surface for all sites. This cannot be a purely wind-induced phenomenon because a 10 day average should remove these effects that change rapidly. Even the backflow at F shows the same phenomena, proving that this is not a wind-effect. ADCP data are not trustworthy close to the surface, and this shallow water character shall be used when constructing a 2-D model for current profiles. Apart from this meander, no evidence seems to show that the situation was not normal, and these profiles will thus be used as support when looking at larger time scales with the ADCP data.
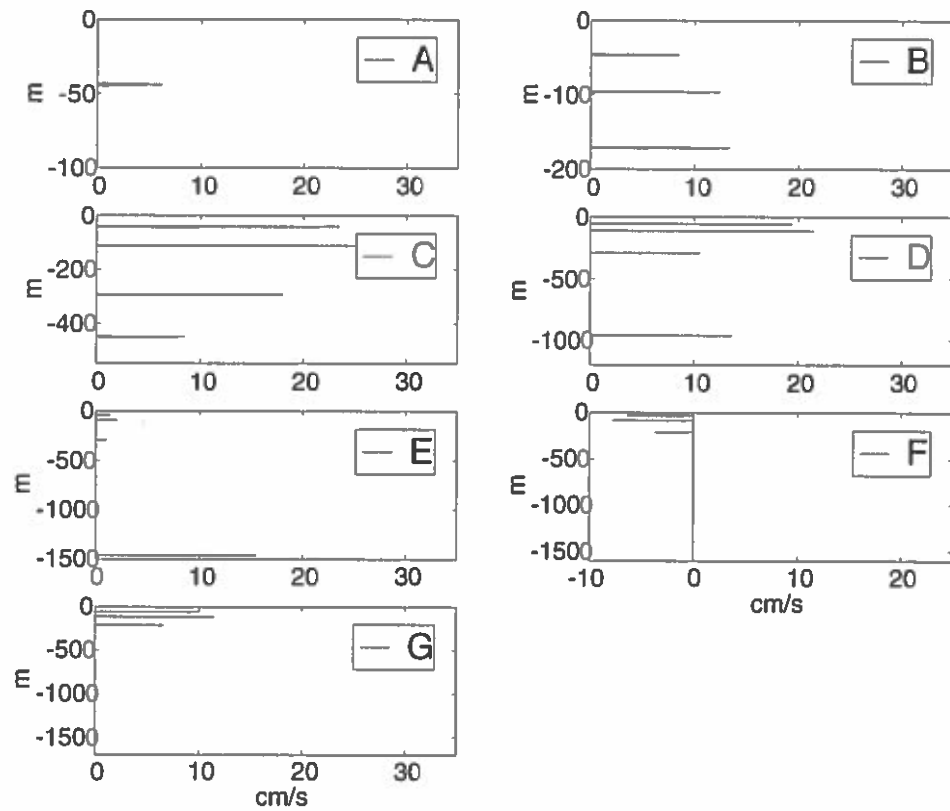
Figure 5.10   Average east-west current (positive east) velocities, for all Aanderaa '86 moorings shown at instrument depths. Lower boundaries are near the sea bottom at each site.

Chapter 6
ADCP

All ADCP data that were sent to me had been through a primary data analysis at the FFL in Tórshavn (Larsen et al. 1999a, 1999b), and tidal analysis and statistics had been applied. The locations of the moorings are shown in figure 6.1. The ADCP instruments give data separated into bins, where one bin is a depth interval (see figure 6.2). The 150 kHz Broadband bottom mounted instruments, like the one placed at A, use a 10 m bin while the 75 kHz instruments use a 25 m bin. The data files are separated into one current speed (magnitude) file and one current direction file, where both consist of one column for each bin and one row for each sampling. Different sampling periods are tried through the years, as we see in table 2.1, but it seems like the 20 min. period is found to be the best. All data from 1994 to 1999 are treated, but most attention is given to 1997-98 because this is the only period when all four stations A, B, C and D are operational at the same time.

The instruments were adjusted to give just one ping (sound pulse) at a time, because this reduces the battery consumption, but at the same time gives rather a noisy (many errors) time series. Data were delivered in daily average files and at full time-resolution, which depends on the instruments sampling period (5, 15 or 20 minutes). The data shown in figure 6.2 are from a daily averaged file, and we see quite a lot of erroneous data even for this long time resolution, but these are luckily confined mostly to the bottom and the sea surface. The full resolution and very voluminous data are even messier and a "cleaning" must be done, before beginning to use these data. This is a dubious task since the error codings are put there because of non-physical data. Care has been taken not to use too much corrected data, and I do not feel that the corrections have introduced any spurious effects.

6.1 Fine time-resolution ADCP

In its full resolution, all ADCP measurements consist of a very large amount of data. This data, which came in a speed-file (*9706.spd) and a direction file (*9706.dir), were first checked for error coding values, and uncoded data were then transformed into east-west and north-south current velocities u and v respectively (positive east and
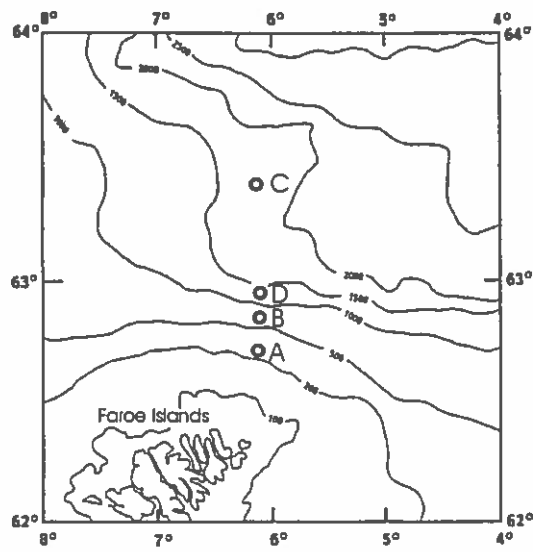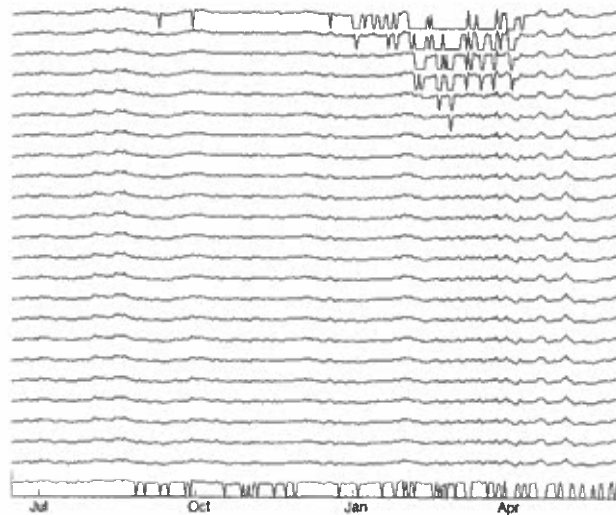
Figure 6.1   All ADCP moorings.

Figure 6.2   One year (1997) of data from mooring A. The lines are eastward current velocities at different bins (10m depth interval). The gaps show error codings '-999', and these occur most frequently close to the surface or close to sea bed.

north). The error codings were retained in these files which now are called *u97.m and *v97.m. The asterix stands for measurement site (A, B, D or C) and the files, containing data from 1997 to 1998, are taken as an example. All the gaps in these files (u and v), are now smoothed out with a cubic spline interpolation, which uses good data from both sides of the error codings, to fit a third order polynomial to the gap itself. All corrections made are marked as one's and good data as zero's in an error log-file of the same dimensionality as the original data file. This log-file (*err9706.m) can be used to change the corrected data points to any number wanted later (0,-999 or something else). It can also be plotted along when viewing corrected data, and we thereby see immediately when data has been modified. This also makes it easier to produce error-statistics.

The following files are then ready for use: "mooring label"u"time period".m, "mooring label"v"time period".m and "mooring label"err"time period".m, for example Au97.m, Av97.m and Aerr97.m, where the extension "m" tells us that these are Matlab® files.

To get a better understanding of data, many different plots were tried: Plots that viewed all data in one diagram like the one shown in figure 6.2, 'feather'-plots that show data from each bin as a rotating vector as a function of time, where its length is current speed and the angle is direction (not shown), hodographs (u,v-plots) for each bin, the instantaneous vertical velocity profile in eastward direction, this velocity profile shown as a movie where one day is shown during each frame and the profiles are plotted with half a second interval and more. All of these plots revealed a quite homogeneous character down through the water column, although quite strong shears are found. The harmonic analysis applied to each bin separately, which already was done at FFL also indicated stable tidal ellipses down through the water column, not differing much in strength or direction. Site C, lying far north of what probably is the main current, showed more variation but this mooring is outside the coverage of the tidal model that shall be applied here.

The homogeneous character of the flow tells us that there are not large phase differences between the deepest and shallowest bins, and this allows us to find a tidal signal by averaging over depth (all bins). Each bin can have a rather irregular appearance, maybe caused by the precision of ADCP measurements, which makes it hard to do analysis on a 20 minute time resolution. But when averaging over depth, a very harmonic signal is found like shown in figures 6.4, A.3 and A.4. The plan is now to compare this depth averaged time series to the barotropic tidal model mentioned in section 3.3.1. Tidal constituents and phases supplied by the model for each mooring location, are found in table 6.1 and described in figure 3.4.

The phases in the last column in table 6.1 are also described in section 3.3.2, and depend on the chosen start time of the model-syntesized times series. The ADCP at D started recording on the eleventh of November 1997, and we have data from all four sites between this time and June 1998 as mentioned. Long-term comparisons between eastward current at A, B and D, and the eastward component of the tidal
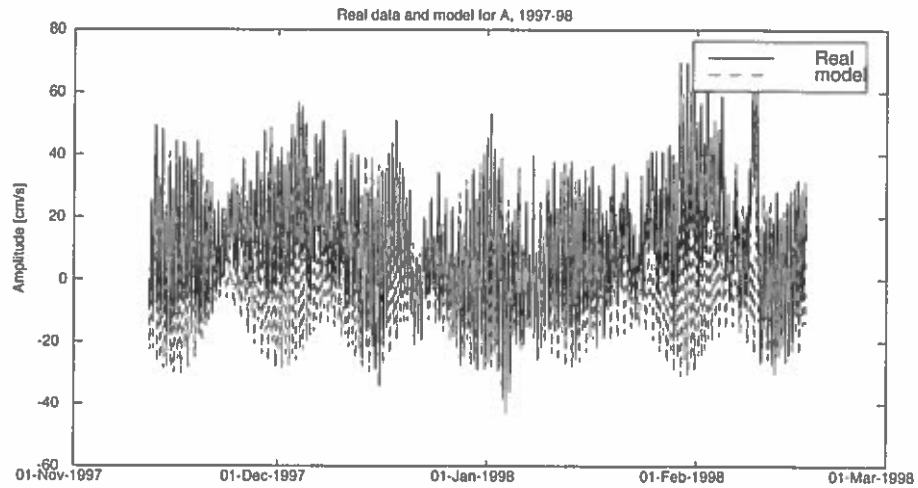
Figure 6.3   Three months of data from mooring A (300 m) compared to a barotropic tidal model. The fluctuations are neap and spring, and we see a nice correlation. The constituents $M_2, S_2, O_1, K_2, N_2, P_1, K_1$, and Q_1, are found in the model

Table 6.1   Six tidal constituents and phases from the model

Con.	A	B	D	v_o
	Major, Minor, Incl,Gpl	Major, Minor, Incl,Gpl	Major, Minor, Incl,Gpl	deg.
Q_1	3.74, -2.11, 74.1, 230	1.27, −0.01, 61.8, 200	0.89, 0.23, 44.6, 180	98.4
O_1	8.06, -4.58, 80.1, 294	2.73, 1.56, 112.5, 298	2.88, 1.31, 165.0, 346	116.1
P_1	5.69, -2.79, 68.6, 296	1.78, 0.92, 62.7, 260	1.64, 0.94, 11.0, 211	38.8
K_1	7.54, -4.99, 70.7, 292	2.20, 1.13, 45.6, 258	2.39, 1.08, 06.0, 216	318.8
N_2	4.03, -2.76, 160.6, 137	1.69, -0.88, 14.7, 283	1.42, -0.56, 19.5, 275	55.8
M_2	16.75, -9.08, 156.6, 139	7.49, -2.67, 07.3, 289	6.93, -1.57, 10.4, 284	73.5
S_2	9.97, -6.56, 172.2, 171	4.76, -2.36, 10.8, 333	4.12, -1.64, 13.2, 329	0
K_2	2.18, -1.61, 167.3, 186	1.05, -0.53, 14.7, 334	0.90, -0.35, 17.1, 328	97.8
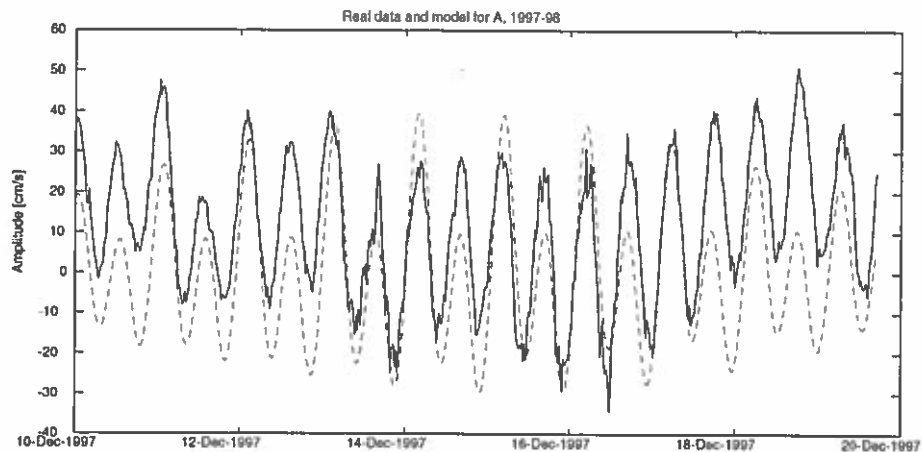
Figure 6.4 Depth-averaged data from mooring A (300m) over ten days compared to the model. The east-west component of the current velocities is shown, being positive eastwards. We see a nice correspondence, but the model has a more mixed semidiurnal-diurnal signal.

current at each location calculated by the model, are shown in figures 6.3, A.1 and A.2. This is over three months, beginning in mid November 1997 and ending in mid February 1998. At all three sites it is evident that the model predicts the correct neap and spring variations, because the undulating movements with around a fourteen day period follow. The spikes are tidal oscillations. A closer look at the correspondence between data and model is shown in figures 6.4, A.3 and A.4. We see that the model predicts reality remarkably well, and at B (figure A.3) even the semi-diurnal/diurnal mixture is almost exactly predicted. Semi-diurnal constituents (those with subscripts '2' in table 6.1) have half day periods and diurnal (subscripts '1') have approximately day periods. If a tidal signal shows that successive current amplitudes have different magnitudes, we have a semi-diurnal/diurnal mixture and the level of mixing is given by the relative sizes of semi-diurnal and diurnal constituents. The model over predicts this mixture somewhat at sites A and D, giving larger differences between successive amplitudes than the data show. But apart from this, I feel that the model gives a very good approximation to the tidal ellipses we are seeking.

The tidal traversing method, shall now be adopted to these data. The e-w components of the generated tidal ellipses are subtracted from the vertically averaged currents in this same direction and if our assumptions hold, this residual shall give us the e-w component of the jet. The main flow direction follows the isobaths in the region quite well, and these are oriented approximately 15° south of east. So the eastward velocities that we present in this and later sections will be a factor $\cos(15°) = 0.966$ of the maximum current velocities in the jet, and these n-s profiles will have slightly lower gradients than those taken cross-isobath. The choice of the
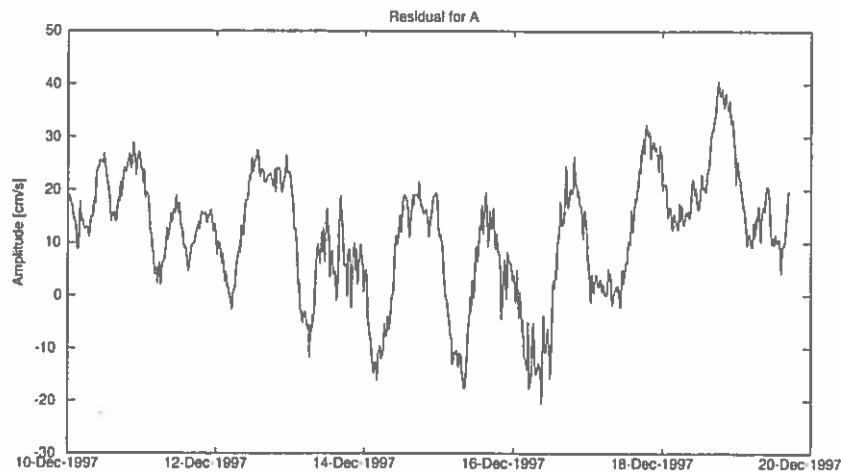
Figure 6.5   The velocity residual found by subtracting the model-syntesized time series from the data at A.

reference frame is irrelevant for flux calculation, as described in section 3.3.2. The profiles will not be stationary when looking north-south because there is a southward residual in the current velocity v, which might be somewhat confusing. The residuals are shown in figures 6.5, A.5 and A.6.

A n-s excursion is now found by integrating the n-s velocities v, and having obtained residuals and coordinates, we are now equipped with a lot more data than with the Aanderaa data. All time series, A, B and D are now scanned from the beginning to the end to find typical profiles for these sites. As mentioned before, oceanographical data can get quite chaotic in such a fine time resolution and these profiles were not easy to interpret. But the trends were there and what I found as typical is shown in figures 6.6, 6.7 and 6.8. The intervals chosen for illustration are from relatively stable periods, because there were periods that did not make any sense at all. We could even get contradicting results with opposite sign on profile slopes during some periods, so the results should be viewd with some precaution. It is clear though that the tendency at A was a negative slope which, as discussed in section 3.3.2, indicates a higher current velocity on the seaward side of this mooring. B shows a more regular character than A, and has always a positive slope when circumstances are stable, and this mooring is therefore probably on the off-shore side of the main jet. Instrument D shows also most often a positive slope, but the signal is harder to read here because the tidal excursions are small there.

A negative slope in these plots means positive gradients in reality and vice versa (see section 3.3.2). Slopes at A are found to have gradients ranging from $3\frac{cm/s}{km}$ to $8\frac{cm/s}{km}$ meaning that current velocities increase 3 to 8 cm/s for each kilometer one
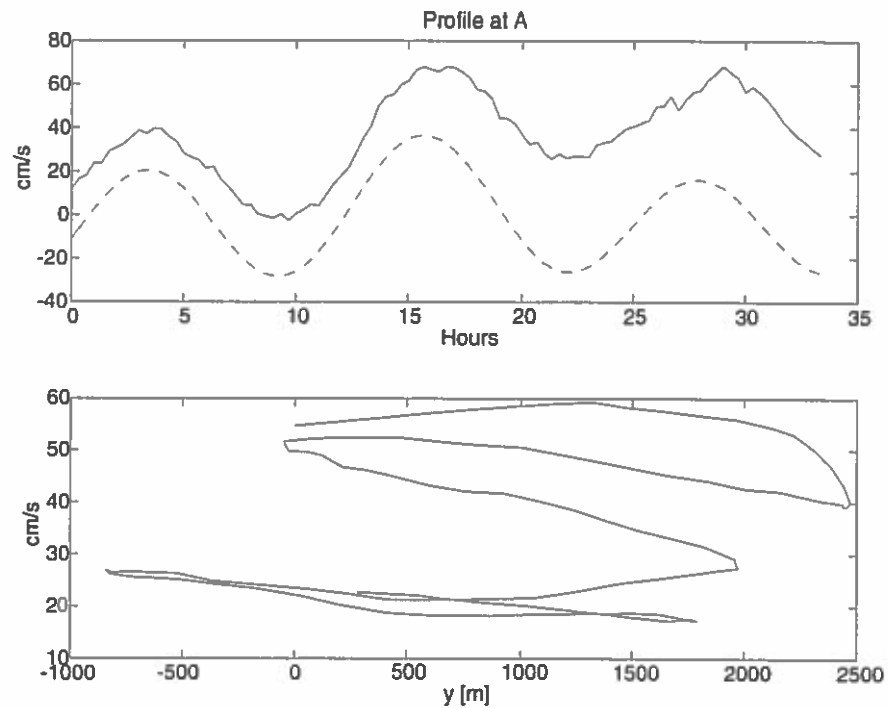
Figure 6.6 Thirty-five hours of data in a period with high current velocities. The upper window shows the depth averaged data from mooring A and the model prediction. The lower window shows the residual plotted as a function of north-south coordinate y (positive north). y is found from an integration of the north-south current velocity v. A negative slope of this profile tells us that higher current velocities are on the offshore side of the instrument.
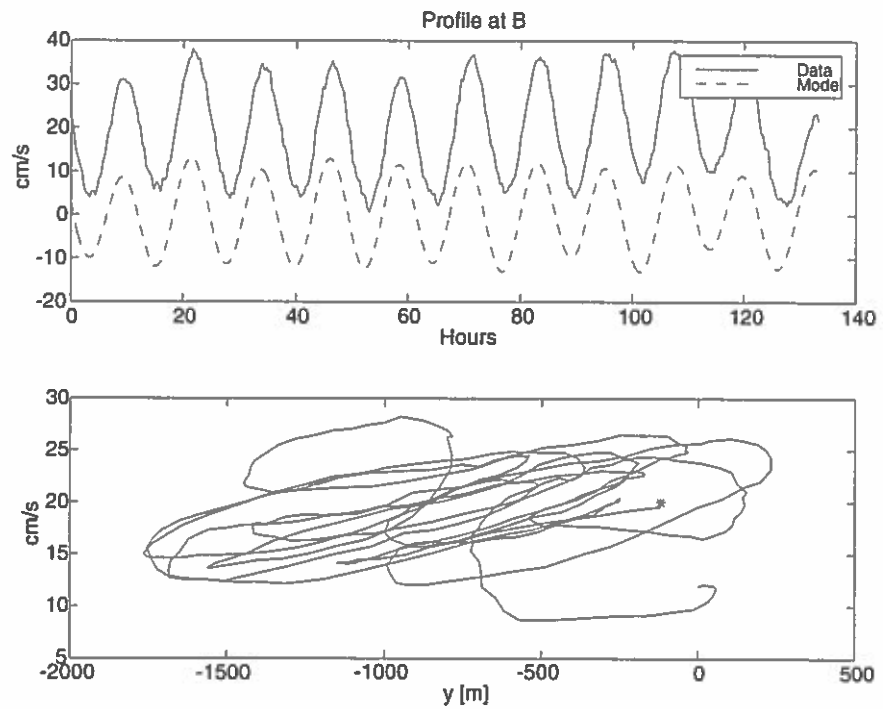
Figure 6.7 Almost two days of data from a period with stable current conditions at B. The upper window shows that fluctuations are nearly matched by the model, and have a fairly constant residual in difference. Lower window shows the profile with a postive slope in a confined region during the period.
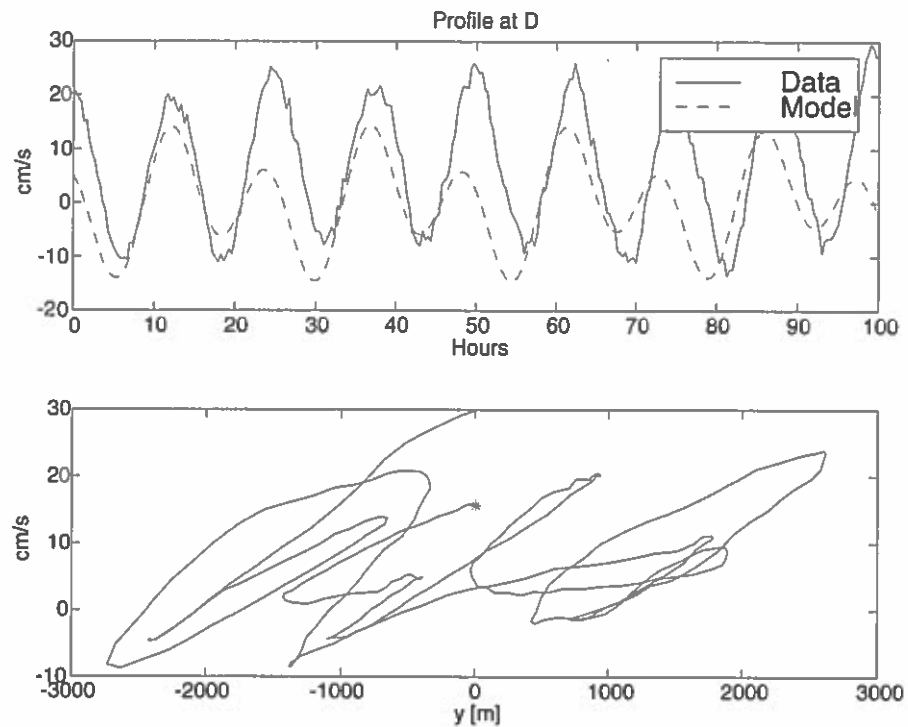
Figure 6.8   Average conditions during 100 hours at D. The lower window shows again a postive slope as expected, and the gradient is steeper than at B.

moves north of the site, at times when the narrow jet is assumed to be close to A. At B we find a gradient range from $-6\frac{cm/s}{km}$ to $-10\frac{cm/s}{km}$ and at D this ranges from $-8\frac{cm/s}{km}$ to $-13\frac{cm/s}{km}$. These estimates are found visually from figures 6.6-6.8, and must be looked upon as very coarse, however $-13\frac{cm/s}{km}$ is a large relative vorticity, on the order of -f.

The presented slopes are much steeper than the slopes of the annual averaged profile which will be discussed later, and this was expected from the discussion in section 3.4.

6.2   Daily averaged data

The daily averaged data files have been through an analysis at FFL which is described in Larsen et al. (1999a) and (1999b). We apply the same component decomposition and primary analysis as we did for the high-resolution data. To get an overview of the data and to compare individual moorings, I first plot all the data from each year in one diagram as shown in figures 6.9 and 6.10 which should speak for themselves. Similar plots for the years 94-95 and 96-97 are found in Appendix A.2.
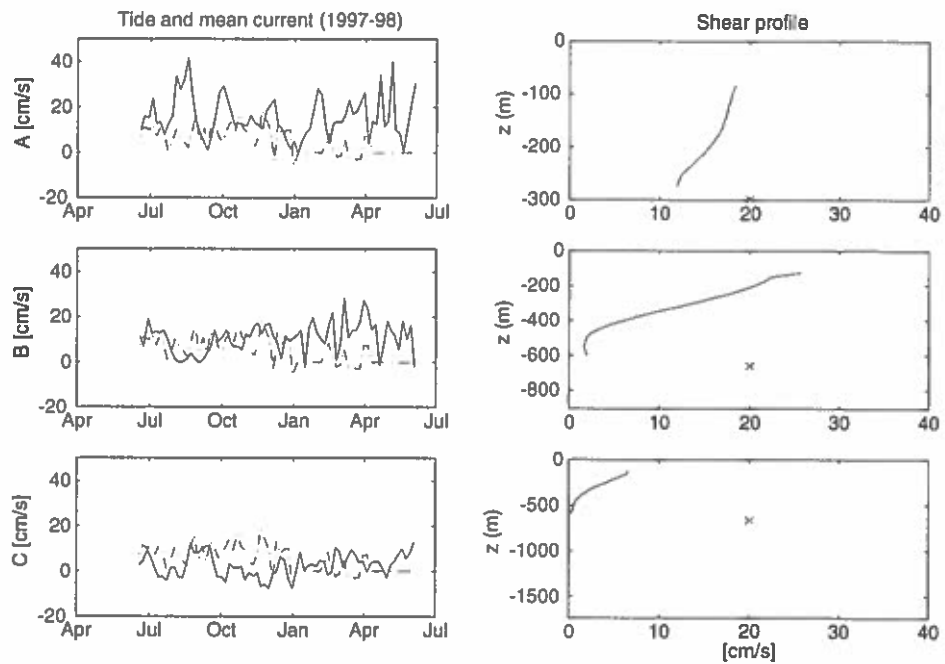
Figure 6.9 Overview over the data from 1997-98, where the dash-dot lines are five-day average water level in Tórshavn and the full lines are east-west depth-averaged currents at site A, B and C. Their averaged shear profiles over the period are also shown, where lower boundaries are at the bottom and the 'x' marks the instrument position. Horizontal dash-dot lines indicate period of missing data.
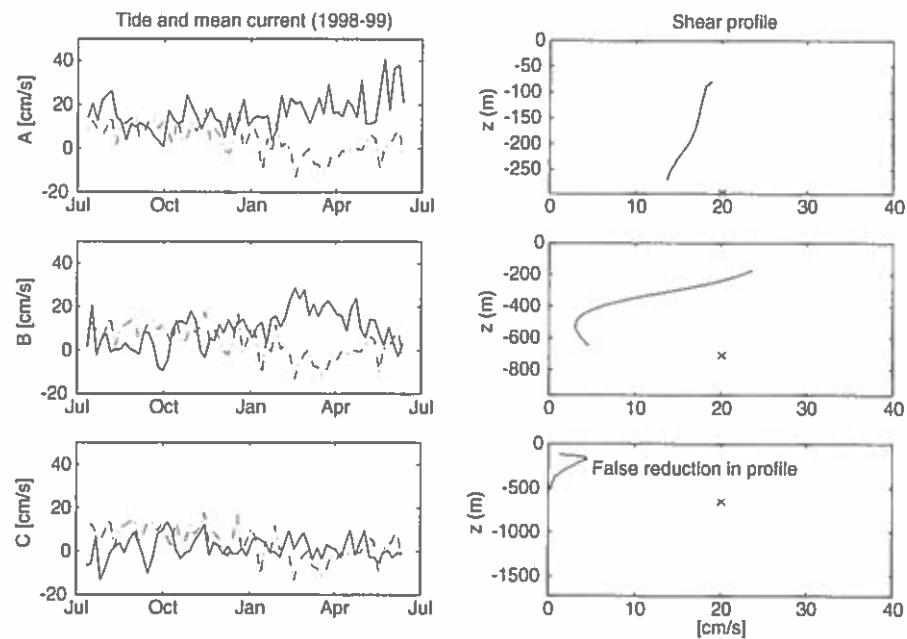
Figure 6.10 Overview over the data from 1998-99, where the dash-dot lines are five-day average water level in Tórshavn and the full-lines are east-west depth-averaged currents at sites A, B and C. Their averaged shear profiles over the period are also shown where the lower boundaries are at the bottom and the 'x' marks the instrument position. The profile shows false values for shallow water bins because of too long error coding patches.

Strong shears are seen at site B, which is the mooring placed closest to the main jet, and the more remote A and C also show a shear. Plot for site D is in Appendix A.2. Site A shows higher mean values, which comes from the fact that it is shallower, and velocities never reach very low values. There is a considerable flow along the bottom here.

6.2.1 *Erroneous data*

In the lowest right window in figure 6.10, we see that the velocity profile suddenly jumps to almost zero. This is because the data were too bad in the shallower bins for this time series. If we take a look again at 6.2 in this chapter, we see that a correction of data in the shallowest two bins is hardly trustworthy and the illustrations in this section are all done disregarding the two shallowest bins. Most errors occurred in March and April, and the CTD data show that the water temperatures on the Faroe Plateau and off the shelf are lowest in these months. So the high error frequency is probably caused by a lack of reflectors (plankton) in cold conditions (private communication with K.M.H. Larsen at FFL). Having disregarded the two uppermost bins (and the deepest when this was necessary), we find errors only around this period,
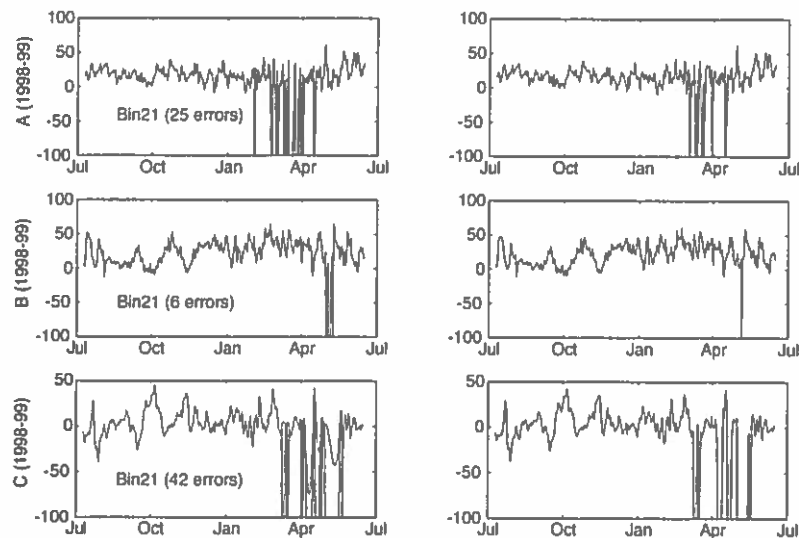
Figure 6.11 An illustration of the errors in the highest two (worst) bins. A careful eye should be able to detect the spline interpolation, that we used to smoothen error codings in the lowest right window.

and the error frequency has become so low in the included bins that the cubic spline interpolation is deemed to be a sufficient remedy for the gaps. The jumps in the lowest right window in figure 6.10, is an example of when the interpolations fail, and figure 6.11 shows why. The two highest (worst) bins that are included are shown, and in the lowest left window we see the performance of the interpolation at mooring C.

The cleaning follows of course good data exactly, but when big gaps occur this interpolation takes a large "dip" introducing too low values to the data series. The insufficiency of the interpolation affects only the highest bins, and the middle section of these shear profiles can be regarded as completely free of error.

6.2.2 Correlations

After having performed the corrections on water level in Tórshavn, as described in section 4.2, these are compared to the currents. This was done in order to do a preliminary check on the correlations that lie as a basis for MAIA. Unfortunately the water level data from Tórshavn are missing in the beginning of 1998, and this makes a thorough correlation analysis difficult for the year 1997-98. ADCP data are averaged in depth, that is, time series are made which contain the mean of all bins. These means are then *block averaged* over an optional time period, and plotted against corrected water level data which also are block averaged over this same period. If we choose a period of e.g. five days for the block average, then the mean value of five consecutive days is calculated and the third day will present these day with

this mean value. This procedure is done throughout the entire data series, and we obtain new data series which are five times shorter than the original. This is in contrast to a *running average*, where the time series keep their length. The duration of these periods is then varied to see how the correlations depend on different time scales. Many such simultaneous plots are shown in Appendix A.2. All plots show that the correlations increase with increased length of the block used, and this is expected considering all the random fluctuations that occur, both at the water level measurement site and at the current meter locations, in a short time scale. We have wind changes, current non-linearities and rapidly fluctuating air pressure (see section 4.2) affecting the water level somewhat randomly close to the coast, and we have large meanders, internal waves and more which disturbs geostrophy in short time scales.

The plots show that water level and current velocities are negatively correlated, and this was not expected considering the work of McClimans et al. (1999), which showed good positive correlations along the continental shelf in Norway. The flow along the shelf in Norway is geographically divided into a baroclinic part and a barotropic part, and this is not the case along the northern shelf of the Faroe Plateau, so should one expect same results? But a negative- and a positive correlation are equally good for predictional purposes. The trend during all these four years of data is that ADCP site B shows the strongest correlations, which is expected, since this station lies closest to the assumed main current jet and there for presents the largest volume fluxes. The correlation between corrected water level and current velocity at B, in a five day block average are stronger than -0.50 and this correlation approaches -0.90 when using monthly blocks. Site A shows a weaker correlation, ranging from un-correlated in a five day time window, but approaching -0.50 for monthly blocks. Site C has an even weaker correlation than A, being most often positively correlated to the water level. The time periods where both current- and sea-level data exist during 1997-98, show remarkably close positive correlations between the more remote sites D and C, on a short time scale (see Appendix A.2), while those closer to the shelf, A and B, still show negative correlations.

The model that we shall present in chapter seven will give good estimates of annually averaged volume fluxes, but it gives also a lot of geographical information on the current form. This information is used to make a preliminary algorithm following the examples of Turrell et al. (1999) and Hansen et al. (1999). Weighting factors are found from the mathematical current distribution, presented in the model, and this makes volume flux calculations with a daily resolution possible. Using this preliminary algorithm to calculate a time series with volume fluxes, and then compare block averages of this time series to the corrected water level, reveals very good negative correlations. In figure A.24, in Appendix A.2, we see that the water level is almost mirrored in the volume flux using a monthly block average, and the correlation is -0.86. This comparison is only performed for the year 1998-99, because this is the only year with good ADCP and good water level data coverage. It is most evident in this figure, that volume fluxes in the early spring are much larger than in the

summer-autumn period. All years show an increase in current speed in early spring and lowest current speed in late summer.

Chapter 7
FINDING A VELOCITY PROFILE FOR THE SECTION

We have up to now compared ADCP with a tidal model and to water level data in Tórshavn. In this section, a compilation of Aanderaa, CTD and ADCP data shall be used to construct an analytic function that describes an annual average eastward current velocity distribution. The CTD stations which are regularly spaced at 10 nautical miles (18.52 km) intervals along our section at 6°05' W, shall establish the "backbone" of our coordinate system as shown in figure 7.1. Here the ADCP stations are noted by upper case labels and the Aanderaa stations are noted by lower case.

7.1 Presenting the method

The idea now is to test-fit a cosine to the depth dependence of the vertical velocity profiles shown in figures 6.9 and 6.10. We use mooring B, with the strongest and deepest profile, to calibrate a mathematical function

$$D(z) = \xi + \beta \cos(kz + \mu) \tag{7.1}$$

for the profile, and find that this approach showed a remarkably good correspondence with the data. The hope is now that this function should also reproduce the other shear profiles, just by multiplying it with a factor for each site. This was a valid assumption for site A (300 m), where the flow "feels" the bottom and has a large barotropic component, but the baroclinic percentage increases when moving seaward, and the profiles diminish in strength and begin to "move" to the sea-surface. They go to a minimum velocity value at smaller depths than do those closer to land, and the phase μ in (7.1) has to be altered for optimal fit at mooring C. At the suggestion of B. Hansen, a linear y dependence

$$\mu(y) = \alpha y + \mu_0 \tag{7.2}$$

was tried. This idea comes from the wedge shape of the Faroe Current in this region, and the coefficient α comes from the sloping pycnoclines in the region, as we shall see. The flow becomes more and more baroclinic moving seaward, and the thermal wind calculations should therefore be more and more accurate. In this deep region around mooring C (depths from 1200-2000 m), thermal wind shears calculated from CTD data using station N05, N06, N07 and N08 are used as an aid to fit the linear
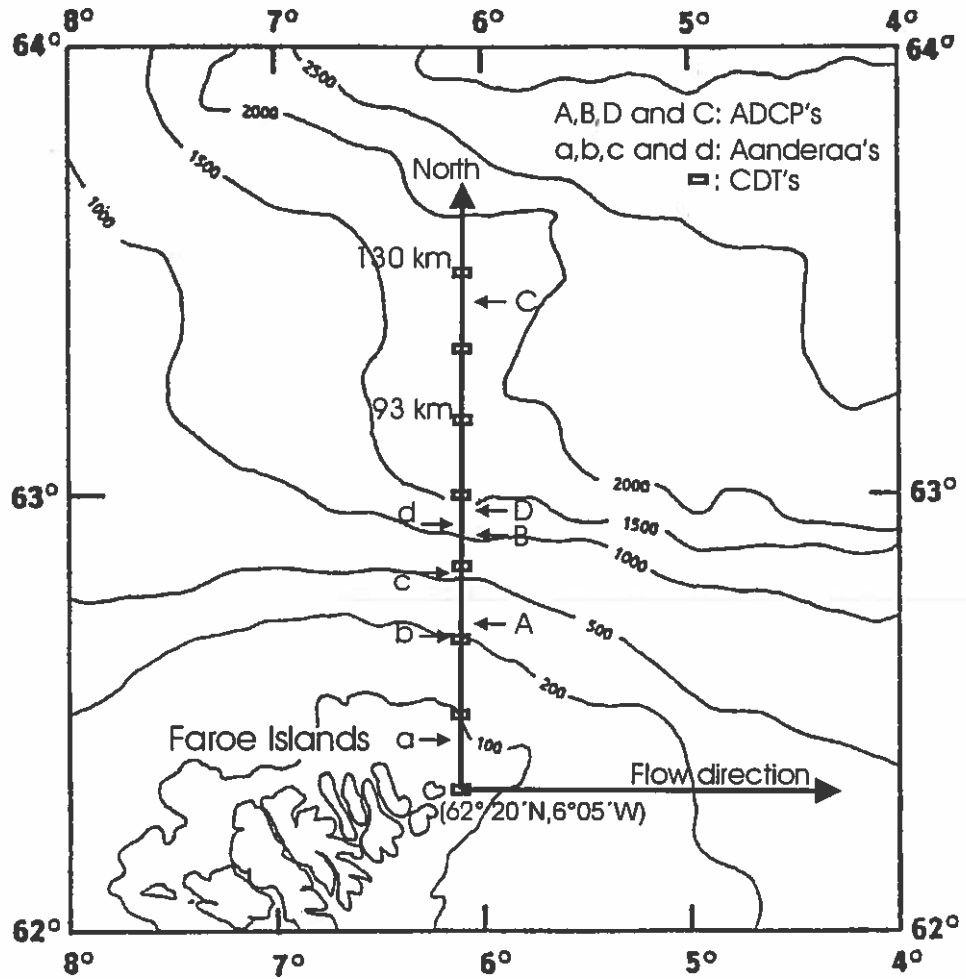
Figure 7.1   The coordinate frame based on CTD stations. Positions of the origin and the different moorings are shown.
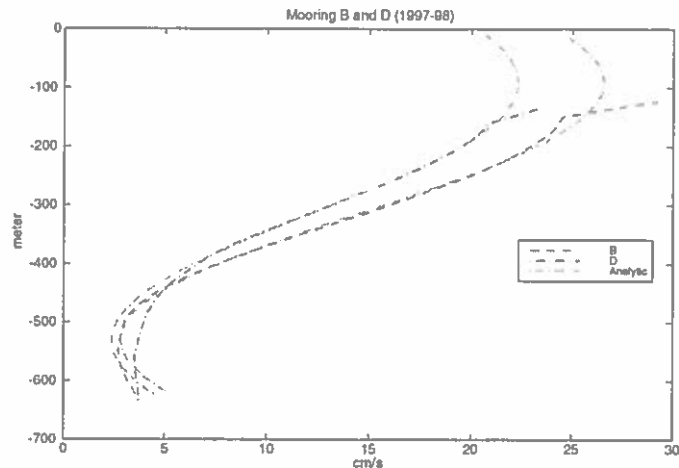
Figure 7.2 A comparison between Mooring B and D during the same time period (11/11-1997 to 13/06-1998). The same depth functions are used while the weighting factor is varied. This shows good fit, but D deviates somewhat at large depths (> 450m). The analytical functions are dash-dotted and extend to the surface, while data from B is shown in dashed and data from D is shown in dash-dot.

y-dependence of the phase μ. Knowing that CTD data are taken from twelve years, while we now look at one year of average profiles at a time, we should not expect complete correspondence between our model and the CTD data. It is also uncertain at what geographical distance from land the flow looses its barotropic character completely, and therefore, when to expect a good fit to the CTD data. So the thermal wind is merely used as a guideline while the ADCP profiles must agree optimally. Doing this analysis, I find good fits, but must use two piecewise linear functions for $\mu = \mu(y)$, to obtain it. This is reasonable because the pycnoclines are not rectilinear throughout the entire region. Moving towards land from our starting point, mooring B, we see that the CTD data begin to disagree strongly with the ADCP data. CTD N03 and ADCP A, show completely different profiles (A much stronger in figure 7.7) and it is clear that we can not rely on density data alone. We then seek guidance from the nearly two weeks of Aanderaa current data. Again knowing that these data come from a different year and over a short period, we will not rely on them, but use them as indications where we do not have anything better. ADCP A must again fit optimally.

ADCP D does not have data from the entire year 1997-98, and the winter shear profiles are slightly different than the summer profiles. We have generally higher velocities in the winter time, and this difference is especially clear in the deeper layers (see figure 7.2). So in order to fit D to the year average data, moorings B and D are compared during the same time interval, and the relation found between them during this period (11 Nov. 1997 to 13 June 1998), is assumed to hold for the full year. The
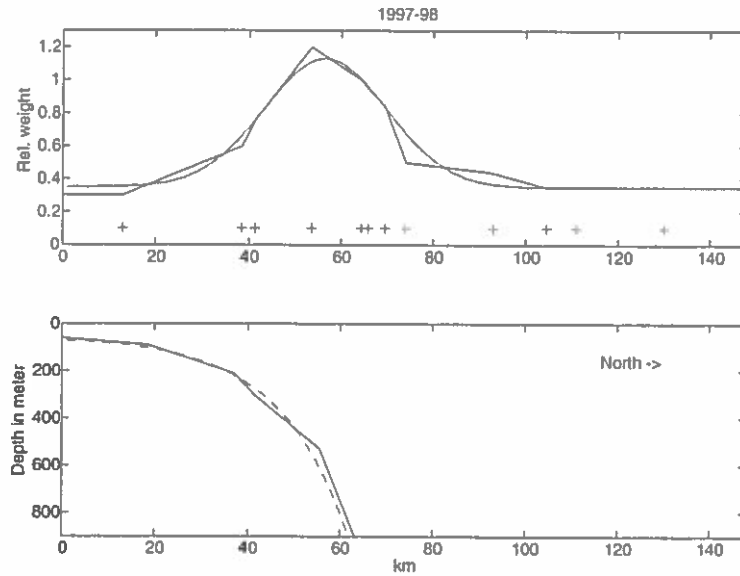
Figure 7.3 Upper window: Relative weigthing factors for the different moorings, and a fitted normal distribution. The depth-dependent function at B has a reference weight of unity. The moorings upon which the fitting is based are shown with crosses. Lower window: The bottom depth shown as a function of the coordinate y which has its origin at N01 (62 deg. 20 min. N, 6 deg. 5 min.W, bottom depth 70m). An exponential function is fitted to the shelf profile (dashed line).

difference between the two analytic functions in figure 7.2, is only a multiplicative constant.

The depth function, for each site is now given by the following expression

$$D_i(y, z) = (\varepsilon_z + \beta_z \cos(k_z z + \mu_z(y)))\delta_i \tag{7.3}$$

where the subscript stands for mooring 'i', and δ_i is referred to as a weight. The interesting thing is that a very good fit was obtainable with the same mean ζ_z, amplitude β_z "wavenumber" k_z and linear varying phase μ_z, at all sites. This simplifies the analytical approach considerably. We consider the mooring B profile as a reference for both the 1997-98 analysis and the 1998-99 analysis, with $\delta_{B97} = 1$. Plotting all the weights, found by fitting, as a function of lateral coordinate y, we find the full line in the upper window in figure 7.3. After trying many analytical functions to fit these weights, I found that the one which corresponded best, and was by far easiest to handle from an analytical viewpoint, was the normal distribution. This is in agreement with the discussion in section 3.4, and the fitted Gaussian function, shown with dashed line in figure 7.3, is given as

$$f(y) = \varepsilon_y + \beta_y e^{-\{(y-\mu_y)/\sigma\}^2} \tag{7.4}$$

ε_y gives the level that the function approaches when y gets very large, β_y gives the maximum amplitude over this level, μ_y gives the lateral position of the peak and σ is a kind of variance giving the spread of this function. Finally we have the form of the overall sectional eastward velocity profile is given by

$$u(y,z) = D(y,z)f(y) = (\varepsilon_z + \beta_z \cos(k_z z + \mu_z(y)))(\varepsilon_y + \beta_y e^{-\{(y-\mu_y)/\sigma\}^2}) \quad (7.5)$$

In the lower window in figure 7.3, we have plotted some known depths as functions of the lateral coordinate in our coordinate system, and an exponential function

$$s(y) = \varepsilon_s + \beta_s e^{\gamma(y+\mu_s)} \quad (7.6)$$

is fitted to the shelf with fairly good resemblance. This function is used as a depth limit down to 600 m from where we have a horizontal integration limit for some distance. Further off-shore these integration limits begin to slope up toward the surface governed by the linear phase functions (see figure 7.8). We begin our integration between N01 and N02 (at 9.26 km in our frame) and end the integration at 148 km, where the velocities are zero. The landward limit is chosen in order not to include the circulating coastal current, but the choice of lateral limits is not so crucial since these extreme flanks contribute just very little to the total flux calculation. The total annual averaged flux can now be presented as

$$Flux = \sum_i^4 \left\{ \int^{int(i)} \varepsilon_y + \beta_y e^{-\{(y-\mu_y)/\sigma\}^2} \int_0^{\lim_i(y)} \varepsilon_z + \beta_z \cos(\omega_z z + \mu_z(y)) dy dz \right\} Sv \quad (7.7)$$

Where $\lim_i(y)$ denotes the depth limit when we are in the lateral interval int(i) for i=1,2,3 and 4(figure 8).

This looks like an ugly function to handle, but when this method is implemented in Matlab® say, a matrix for $u(y,z)$ is obtained, and by applying the limits the transport in Sverdrups is easily found by simple summation.

7.2 A closer look at 1997-98

Going through the fitting procedure, the different constants and weights are determined and these are shown in tables 7.1 and 7.2

The phase functions in table 7.1, are shown in a form to show where they are applied. It becomes necessary to include the first phase function when we are 68 km from N01, and looking at the lower window in figure 7.3 again, we see that the flow is free of the shelf at these distances. The barotropic component gets much weaker in this region, and the necessity to include phase functions must therefore be a baroclinic effect. The phase functions rely on slopes of the isopycnals, which

Table 7.1 Coefficients for the year 1997-98

Fit	Coefficients
y-dependence	$\varepsilon_y = 0.35$, $\beta_y = 0.78$, $\mu_y = 56.5km$, $\sigma = 18.9km$
z-dependence	$\varepsilon_z = 12.4cm/s$, $\beta_z = 10.89cm/s$, $k = 0.071m^{-1}$
Shelf profile	$\varepsilon_s = 55m$, $\beta_s = 1.95m$, $\gamma = 0.066m^{-1}$, $\mu_s = 30km$
Phase func. one	$\mu_1 = -0.65 + (y - 68) \cdot 0.01$; $103 > y > 68km$
Phase func. two	$\mu_2 = -0.34 + (y - 103) \cdot 0.07$; $y > 103km$
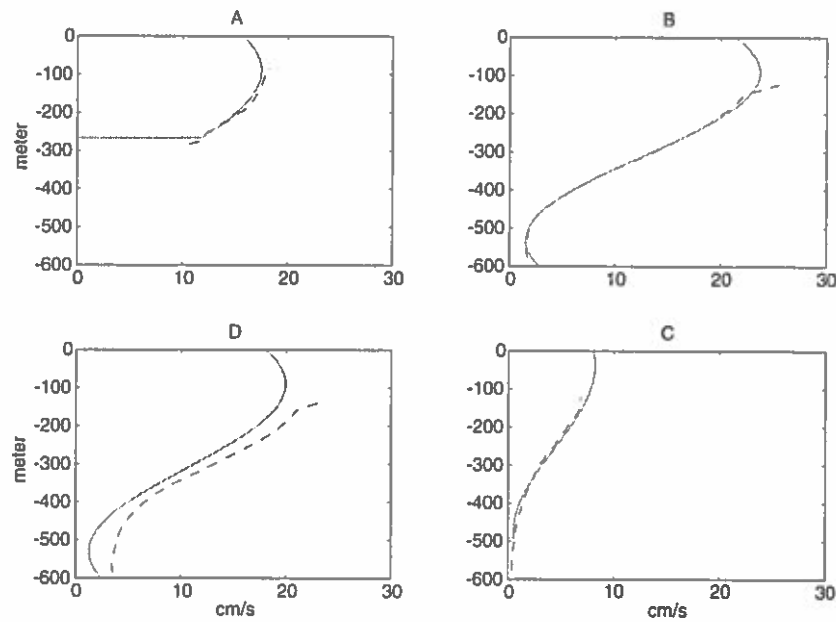
Figure 7.4 Overview over year-average depth profiles at all moorings in 1997-98 (east-west current direction). Real data are shown with dashed line, and the model is the full lines. The model jumps to zero a bit before the data at A, indicating a shallower bottom. This is because the resolution of the model is one km, and it is therefore not possible to plot the exact A position. The discrepancy at D is because this time series was shorter than the others and consisted mostly of winter data.

Table 7.2 All weights from 1997-98

Site	a	b	A	c	B	d	D	N05	N06	C	N07
Pos.(km)	13.0	38.5	41.3	53.5	64.5	65.9	69.6	74.1	92.6	104.6	129.6
Weight	0.30	0.60	0.76	1.20	1.00	0.95	0.84	0.50	0.44	0.35	0.35
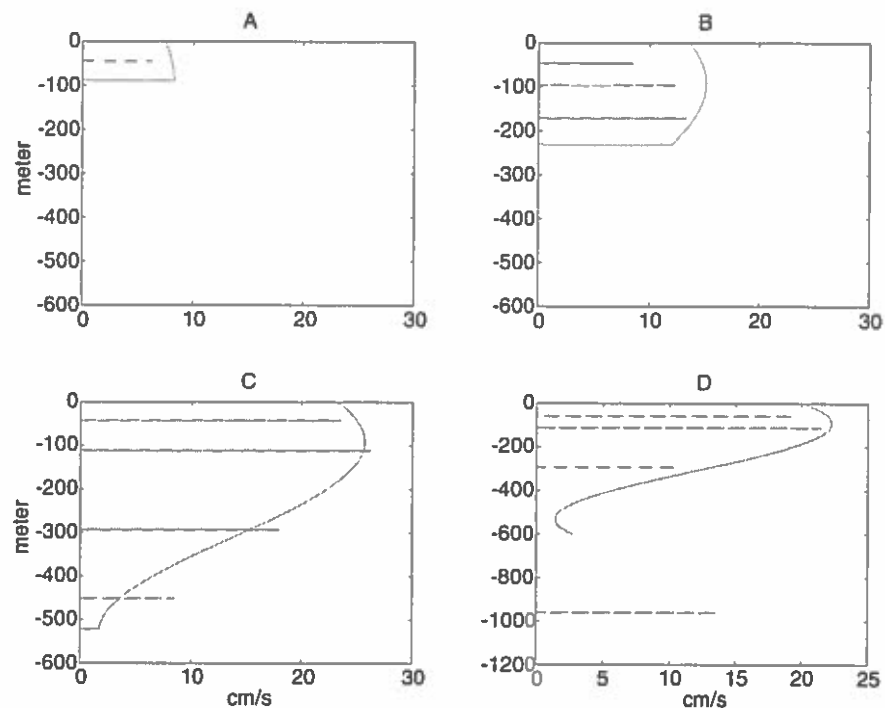
Figure 7.5 The model from 1997 compared to fourteen days of Aanderaa data from June 1986. This is just used as a guidance, but the shapes fit fairly well. The spikes show averaged east-west current data from each instrumet. The lower velocities that the model show at very shallow waters, seems to be confirmed by these measurements. The rather high velocity measured in deep water at D is not explained.

is a baroclinic phenomena. Having found all of these values, a matrix u(y,z) with dimensions 148x600 is produced. (148 km in lateral direction and 600 m in depth) We have now a model with 1 km resolution in the horizontal and 1 m resolution in the vertical direction. By plotting "slices" of this model as close to the different moorings as possible we shall validate this to reality. Figure 7.4 shows cuts at y = 41, 64, 70 and 93 km plotted against A, B, D and C. It is most important that these profiles match, which they very well do. Even the small velocity increase in the deepest bins which seems to occur for all time series in the main current area, lies inherent in the cosine function. There has been a question of how strong the currents can be in the near-surface where no ADCP data are available. This has been circumvented by others with the assumption of constant velocity from the highest good bins to the surface (private communication with B. Turrell and B. Hansen). The shallowest bins are much more uncertain than the rest as we have seen, so this might be a bit dubious. This model lets the cosine form continue naturally, resulting in larger velocities above the highest good bins, but velocities decrease again when we get close to the surface
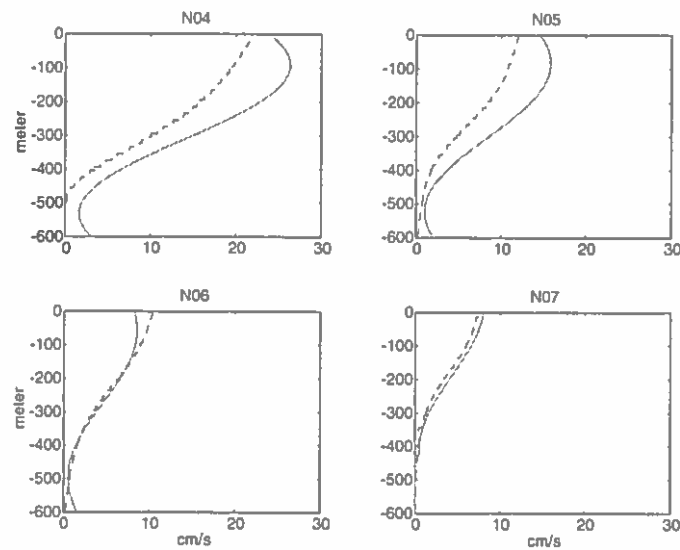
Figure 7.6 Model compared to twelve years of hydrographic data from the same section (the most central staions are shown). The CTD data underestimate the current when the bottom depth is shallower than approximately one kilometer (N04 and N05). Going to greater depths (N06 and N07), we see that the flow becomes baroclinic and the profiles agree better.

($\sim$0-80m). The shelf has been removed from the profile as we see in window A, figure 7.4. Making cuts at y = 13, 39, 54 and 66 km and plotting these "slices" against the Aanderaa data we also find a fair correspondence (figure 7.5). The cosine shape is confirmed, and even the current decrease close to the surface, which one could assume just was an effect from using a cosine, fits these data interestingly well.

Compared to the profiles calculated from the density (CTD), we see that both N04 and N05 underestimate the current. The discrepancy comes from the barotropic component which the thermal wind calculations cannot show. But when we get out to N06, and especially at N07, we see that model and data agree very well, and the flow is purely baroclinic. To caution against using CTD data in shallow water, I plot A and N03 (200-300m) in the same diagram (figure 7.7), and we see two completely different profiles.

Plotting lines of equal velocities (contour plot), we get a good overview of where the highest currents occur relative to the shelf. The shelf plotted in figures 7.8 and 7.9 comes from the fitted exponential function, and the integration areas, i = 1, 2, 3 and 4 and the limits in each area mentioned in (7.7), are apparent in these figures. The red dashed lines, which mark the zero velocity limits, are found by optimally fitting the phases in the velocity profiles (ADCP and CTD) and not by considering density directly. By considering figure 7.4C and figure 7.6, we see that the velocity
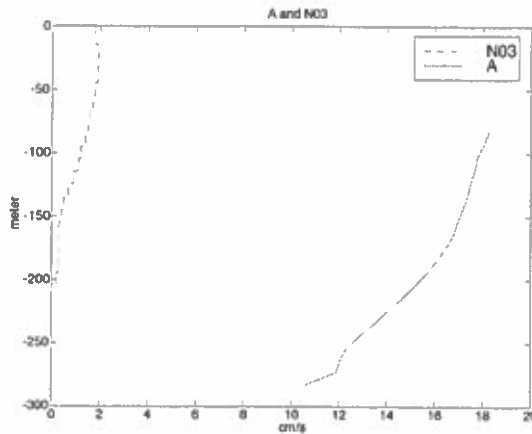
Figure 7.7   A and N03 are spaced only 4 km apart, and we see a large difference in velocities. The termal wind calculation has seriously broken down.

profiles are uniform only when the velocities are zero and from (3.4) section 3.1.2 we have

$$\frac{\partial u}{\partial z} = \frac{g}{\rho_0}\frac{\partial \rho}{\partial y}$$

and thereby $u = 0 \overset{from\ plot}{\Rightarrow} \frac{\partial u}{\partial z} = 0 \Rightarrow \frac{\partial \rho}{\partial y} = 0$. So the zero lines should go through an area where the isopycnals are level (because no baroclinic current exists in this region), and in figure 7.9 we see that this is not to far off. Because our Gaussian function f(y) (7.4) is constant in this region, and because our phase function appears inside a cosine we get the following result for the slope α in the phase function (7.2): First find the slope λ of the line which gives $\frac{\partial \rho}{\partial y} = const.$, and evaluate

$$\alpha = k_z \cdot \lambda \tag{7.8}$$

where k_z is the "frequency" of the z-dependency (see (7.3)). The necessity to introduce y-dependency in the cosine depends much on the rectilinearity of the isopycnals, and the vertical shear depends on the slopes down through a depth column. In figure 7.10 we present the 97-98 profile in a 3-D view, and the final y-profile becomes apparent here. The contour is retained in the background, and all the measurement stations are indicated. The shelf profile is enhanced in order to help to understand the physical situation, but it should in reality be directed more southward. From these figures it is evident that the high-velocity jet core lies somewhere above the 600-650 m isobaths which are around y = 55-57 km in our coordinate system. All elements in u(y,z) are now summed and the correct increments are multiplied to this sum, giving us an average transport in the year 1997-98 of 4.17 Sv (Sv=1·10^6 m^3/s).
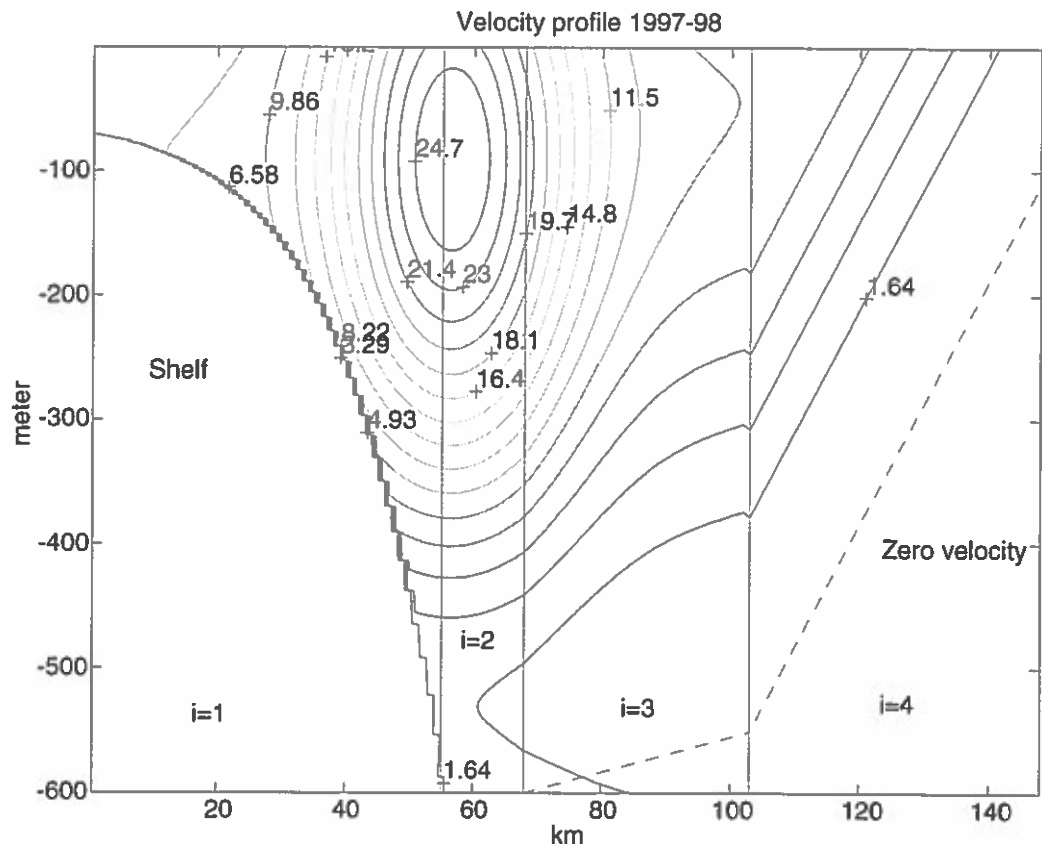
Figure 7.8   Contour plot of the velocity profile 1997-98, looking westward. The iso-velocity lines are plotted, and their velocities are shown in cm/s. Velocities are zero under the dashed lines. The integration area is divided by vertical lines (hardly seen), and the shelf profile is drawn (Jagged apperance is caused by model resolution).
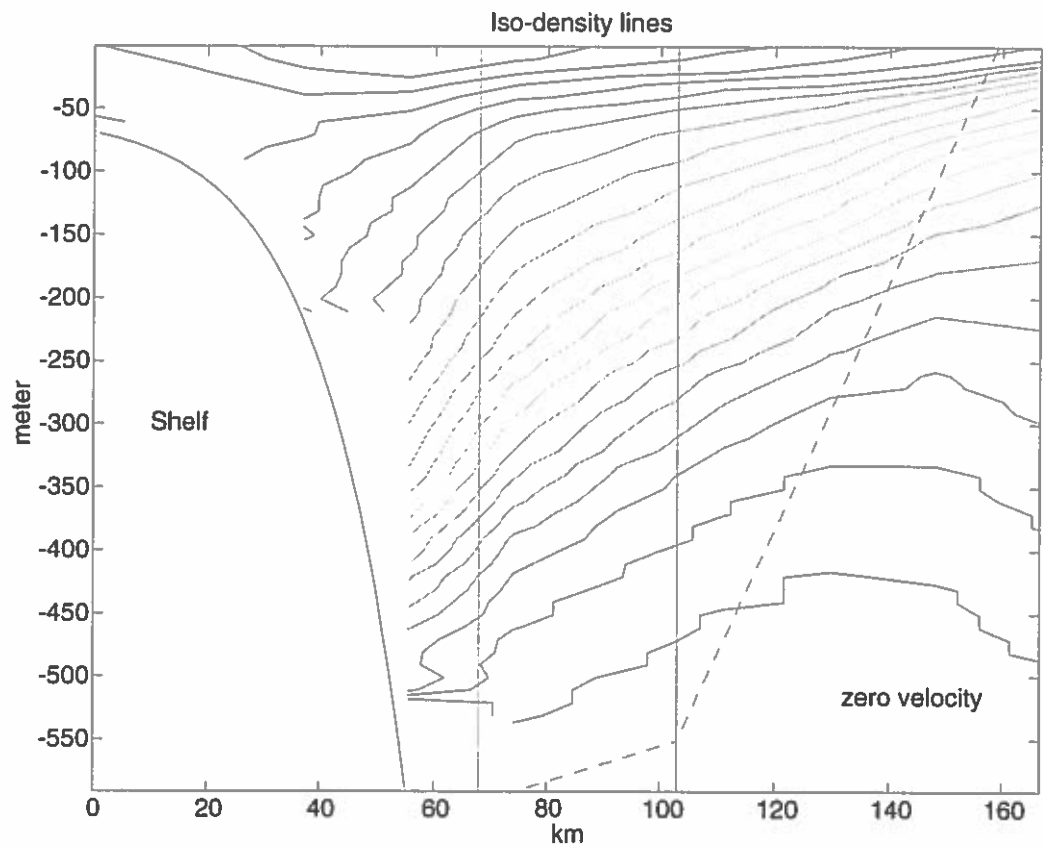
Figure 7.9 Sigma-theta plot from 12 years of CTD data. The zero velocity lines from the model are shown (dashed lines). The deepest iso-lines have the highest density and the shallowest lines have the lowest (westward view, shelf shown).
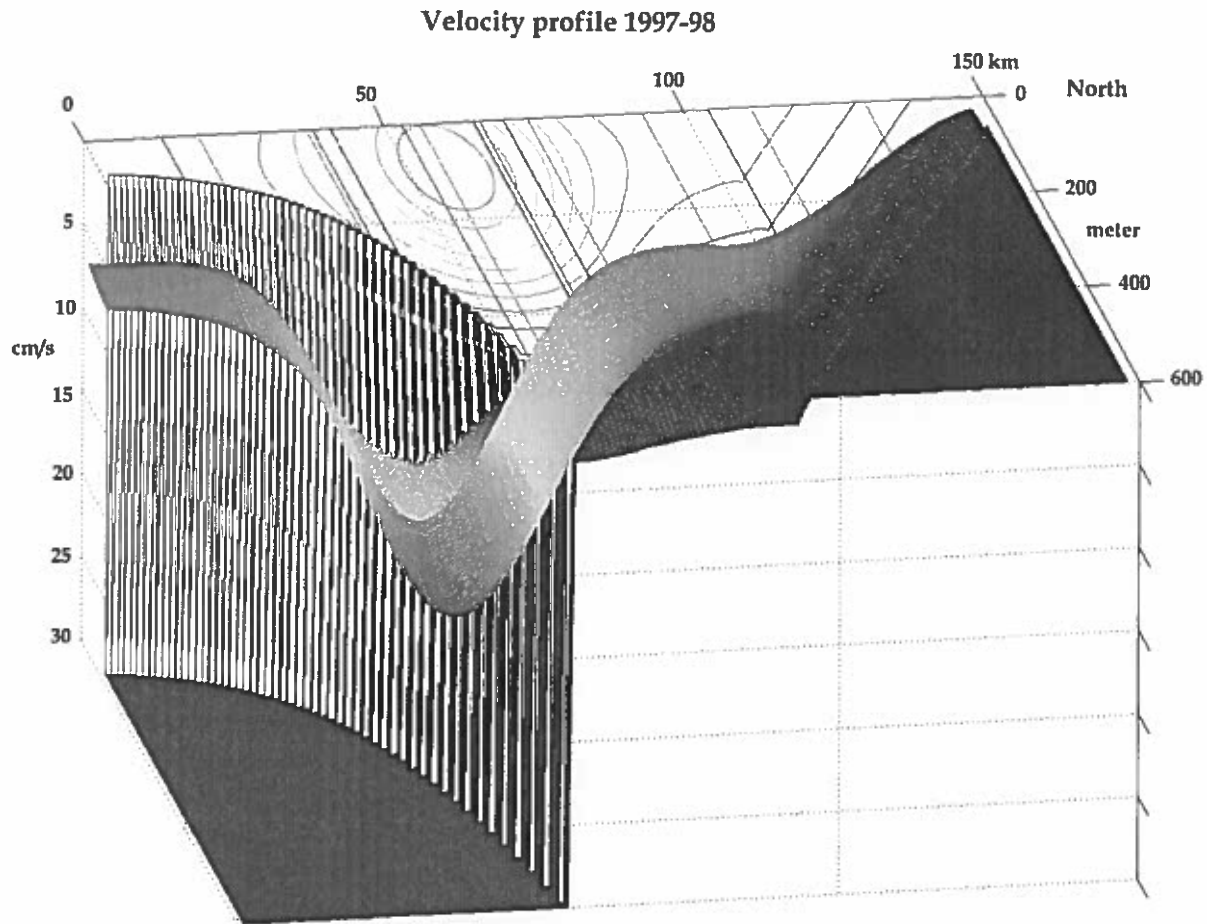
Figure 7.10   A birds eye perspective of the 3-D current profile estimated with the model for 1997-98, and the bottom shelf that it is leaning upon. A contour plot is drawn that shows levels of equal speed (see figure 7.8), and we see from this that the highest speeds are found close to the surface above the 600-650m isobaths. The lines indicating data-measurement sections are shown. The distance in kilometers north of the reference point is shown, together with the depth in meters and speed in cm/s.

Table 7.3   Coefficients for the year 1998-99

Fit	Coefficients
y-dependence	$\varepsilon_y = 0.35$, $\beta_y = 0.98$, $\mu_y = 58km$, $\sigma = 18.9km$
z-dependence	$\varepsilon_z = 12.4cm/s$, $\beta_z = 10.89cm/s$, $k = 0.071m^{-1}$
Shelf profile	$\varepsilon_s = 55m$, $\beta_s = 1.95m$, $\gamma = 0.066m^{-1}$, $\mu_s = 30km$
Phase func. one	$\mu_1 = -0.75 + (y - 42) \cdot 0.0042$; $98 > y > 42km$
Phase func.two	$\mu_2 = -0.52 + (y - 98) \cdot 0.07$; $y > 98km$

Table 7.4   All weights from 1998-99

Site	a	b	A	c	B	d	D	N05	N06	C	N07
Pos.(km)	13	38.5	41.1	53.5	65.1	65.9	nil	74.1	92.6	103.7	111.1
Weight	0.30	0.60	0.80	1.20	1.20	0.95	nil	0.50	0.44	0.35	0.35

7.3   A look at 98-99

Doing the same analysis for the consecutive year, 1998 - 99, we obtain the weights and coefficients shown in tables 7.3 and 7.4.

The interesting fact here is that the z-dependence coefficients are not altered at all. This is not because we use the same CTD and Aanderaa data in the fit, for the ADCP's have precedence in this fit and these data come from a different year. It is also interesting to note that only two coefficients are altered in the y-dependence which are the horizontal positioning factor μ_y and the amplitude β_y. The phase functions have though changed a bit which tells us that although the slope of the isolines changes very little (determining the z-dependence) their lateral positions might change some on an annual basis.

The phase varies only from land, and since we rely much on CTD data in this off-shelf region (have only ADCP C as a check-mark), a more trustworthy discussion must come from the CTD data on an annual resolution, and not twelve year averages. This is probably not so essential for our flux calculations, because the volume flux diminishes rapidly in this region far seaward. The fitting of the normal distribution f(y) (7.4) is shown in figure 7.11, and the best validation of a higher volume flux this year than in 1997 - 98, is that the weight at B now is 1.2 from unity the preceding year. We have only three ADCP's to rely on this year, making a fit of the normal distribution much more uncertain, but the fits using the same z-dependence with different weights, is still very good as shown in figure 7.12.

The deviations in the shallower bins (z < 200m) are caused by a higher error frequency this year than the year before, and we saw in section 6.1 that this was the only time when the cubic spline interpolation failed. Again summing up with the increments multiplied gives a transport of 4.56 Sv, and if we take the average over the two years 1997 - 99 this gives an average flux = 4.366 Sv. Estimates by Hansen et al. (1999), using a completely different approach, gave an average volume flux in the range 4.5 - 4.8 where the higher limit came from using a very crude linear
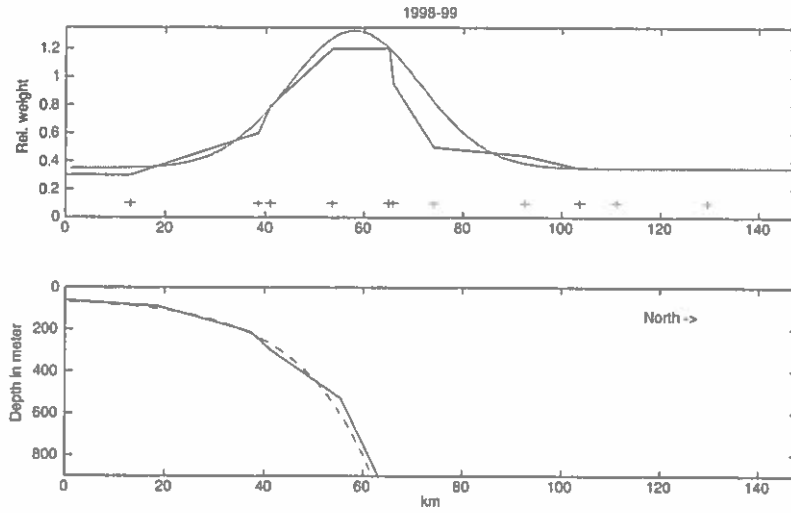
Figure 7.11 Relative weighting factors for the different moorings, a fitted normal distribution and bottom profile with fitted exponential function. Unity reference is still the B mooring in 1997-98. We see higher velocities than in 1997-98, but we have one less ADCP to rely on.
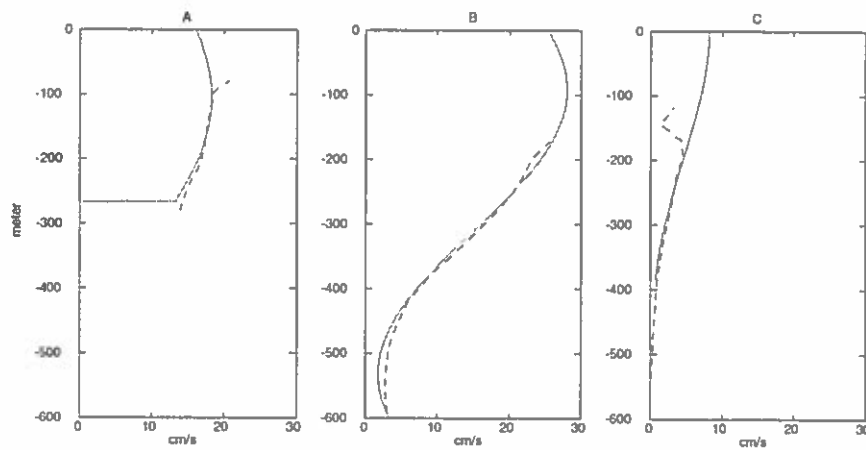

Figure 7.12 Overview over year-average depth profiles at all moorings in 1998 (east-west current direction). Real data are shown with dashed lines, and the model data are the full lines.
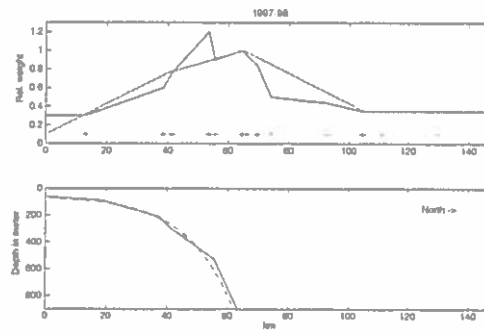
Figure 7.13   A crude linear interpolation between ADCP weighting factors and the shallowest Aanderaa mooring. Crosses indicate measurement stations and one more CTD station (N04) is included which supports the line between ADCP A and B.

approximation in the y-dependence. His lower limit came from a more pragmatic method, so the coherence must be said to be good.

Just as a comment (figure 7.13) on the more crude linear interpolation, I show a plot for 1997-98 where CTD N04 is included in the fit. The y-dependency is linear between the ADCP weight, but the cosine z-dependence is kept. Such an estimation gives these transports: 1997-98) 4.43 Sv, 1998-99) 4.82 Sv and average 4.63 Sv. The error implied is more serious than the flux estimates imply, because we move transports which in reality occur on the landside of B, to its sea-side. It is making two errors that neutralize each other.

Chapter 8
DISCUSSION

8.1 The tidal model and the high time-resolution data

The physics taking place on continental shelves can be very complex, and incoming meanders and other perturbations are known to be frequent along our area of interest. The reason for making the profile analysis with the high-resolution ADCP data, was to get a guideline of where the averaged profile was located. This analysis can be considered partly successful, because we qualitatively get the gradients that were expected. That is a positive gradient at A, meaning that the main current is seaward from this one; a negative and steeper gradient at B indicating that the jet is on the shore side of B and a negative and even steeper gradient at D telling us that this site is on the flank of the current, farther from the peak than B. This corresponds qualitatively well with the annually averaged character of the flow, but the gradients had a high variability. The instantaneous gradients were a factor 10-20 larger than the slope of the averaged profile which is about 0.4 $\frac{cm/s}{km}$, and this is probably too much. Such steep gradients would mean a very narrow, and thereby a very strong current jet, and this was never seen when scanning the entire data series with a "movie". If such a narrow jet existed, one should detect vertical current profiles that suddenly "jumped" to much higher values, and this was never observed. The tidal model reproduces the data quite well, so there might be other more complex physical factors that blur the picture. The method needs refinement before being used routinely.

8.2 Barotropic/baroclinic components and their and flow paths

There has been postulated a very fast, narrow barotropic current with currents in the range 60-100 cm/s which follows the slope, similar to those observed along other continental margins. Since this current has not been observed, it must be narrower than 10 km, if it exists. This is because a much wider jet would surely "hit" one of our measurement sites. If we construct the "worst" scenario, that we have a very fast current 8 km wide with a bell-shaped profile with a maximum 100 cm/s, located at $y = 48$ km (390 m depth), like shown in Appendix A.3, this would only increase the flux calculation by 0.33 Sv, from 4.17 Sv to 4.5 Sv. This exaggerated, very unlikely current, must be in rather shallow water, and it must be so narrow that it will not alter the total flux-calculation considerably.

Such a barotropic current has been measured near the 150-300 m isobath (see figures 7.5B and 7.7), and this is well reflected in the level isopycnals and in the salinity and temperature data (not shown), which show a relatively warm, high-saline core in this region. But this current does not present the largest velocities in the Faroe Current as we have seen.

The conclusions to be drawn from this are that there is a slope bounded current which approaches the Faroe slope through the Faroe Bank Channel or just to the north of the bank, as drifter experiments also have shown. This fast track leads Atlantic Water directly to our measurement section, explaining the higher temperatures and salinities. The water masses taking the more complex route toward Iceland will get cooled and mixed with other currents before reaching our section. These currents follow the broad IFR before reaching the Faroe shelf and are probably those which we measure as baroclinic. Conservation of potential vorticity is believed to be the dominating mechanism considering topographical steering. A change in flow depth will induce a change in relative vorticity and this change in vorticity creates the steering effect. The cold and deep overflow water probably creates a level "floor" on the IFR giving no topographic steering to the currents, and currents with no steering become baroclinic. Since baroclinicity represents the largest fluxes, we can deduce that a dominant part of the water masses in this section stem from areas closer to Iceland.

8.3 Correlations and seasonality

A interesting observation is that volume fluxes in the FC are negatively correlated with the corrected coastal water level between the islands. This correlation gets evident when we make block average of current and water level data over more than ten days. Monthly averages show the strongest correlations, and the seasonal variations with highest water fluxes in early spring when the water level is lowest was pronounced in all the four years that were analyzed. Correlations were not so clear in a short time scale, seven days or shorter, although data from the more remote stations D and C did during some periods (e.g. in periods during the year 1997-98, as shown in figures A.9 and A.10) match the sea-level data remarkably well. Better adjustments must be must be made to the water level data in order to accomplish the five day time-resolution which is the aim in the MAIA-project.

The seasonal variations are reported by Orvik et al. (1999) which show a clear current maxima in the eastern part of the Svinøy section during early spring, and they show that this increase is closely correlated to the NAO (North Atlantic Oscillation) which represents low pressures and thereby westerlies in the North Atlantic. Turrell et al. (1999), measure also a volume flux peak on the south side of the FSC in early spring. But this maximum in flux gets neutralized by the current on the north side of the channel which flows southward, resulting in no marked seasonal total volume flux variations in the channel. It is evident from figure A.25, and from all ADCP

data from the FC, that large annual variations occur here. Since no noticeable back-current has been measured north of the islands, we must conclude that there is a larger volume flux during late winter than during late summer through our section of interest. The currents which flow through the Svinøy section originate from FSC and FC, and if no clear seasonality comes from the FSC, then larger parts of the FC than previously assumed, must flow to the eastern Svinøy section, in order to explain the seasonality there.

The negative correlation between coastal water level and volume flux, which is in contrast to measurements from the Norwegian Continental shelf, must have its explanation in the more complex bathymetry around the Faroe Islands. The shelf in Norway is relatively straight and uniform, compared to the Faroes. A topographically steered barotropic Kelvin wave, which is assumed to transport the sea-level increase, will only send this signal to a coastal measurement station at the instance when it is passing by. The Norwegian coast is like a long straight "wall", and the Kelvin waves follow this "wall". The currents around the Faroes circle the shelf, and the same strong current signal can therefore be sent to the coast from many different directions. This will blur the picture on a short time scale but does not explain the long term negative correlations. More research must be done on this for a good explanation.

8.4 Tidal rectification

Another interesting observation is shown i figure 8.1. Depth averaged eastward current data, are smoothed by a running average for clarity and compared to the barotropic tidal model again. A, B and D are put in the same diagram to see resemblances and differences laterally. The interesting feature is that while tidal rectification models and theory predict current-increases, in periods with large tidal amplitudes (Huthnance (1981,1992), Chen & Beardsley (1995), Pérenne et al. (2000)), we observe the opposite at site B and D. Tidal rectification is the term for an along-isobath residual current generated against bottom friction by the nonlinear transfer of momentum from the oscillating tidal currents to the mean flow. Old models only include barotropic current, but the newer models include also stratification (baroclinicity), and show qualitatively the same results, but intensified (Pérenne et al. 2000). I have not found anything in the literature about tidal currents that break down residual flows, giving highest residual current at neap tide. Most analysis on this theme are numerical, and are mainly applied to shallower water than the depths at B and D, so there is a question if one should expect the same results. What I observe is that A shows a weak correlation to the spring-neap tide period, maybe a bit tidally rectified. In B and D it is evident that there is a sudden break-down in the eastward current at spring tide, which gets established again at neap tide. The main difference between A and (B and D), is that the first location has nearly no baroclinic component while the other two do, and I will therefore seek an explanation in this difference. A baroclinic
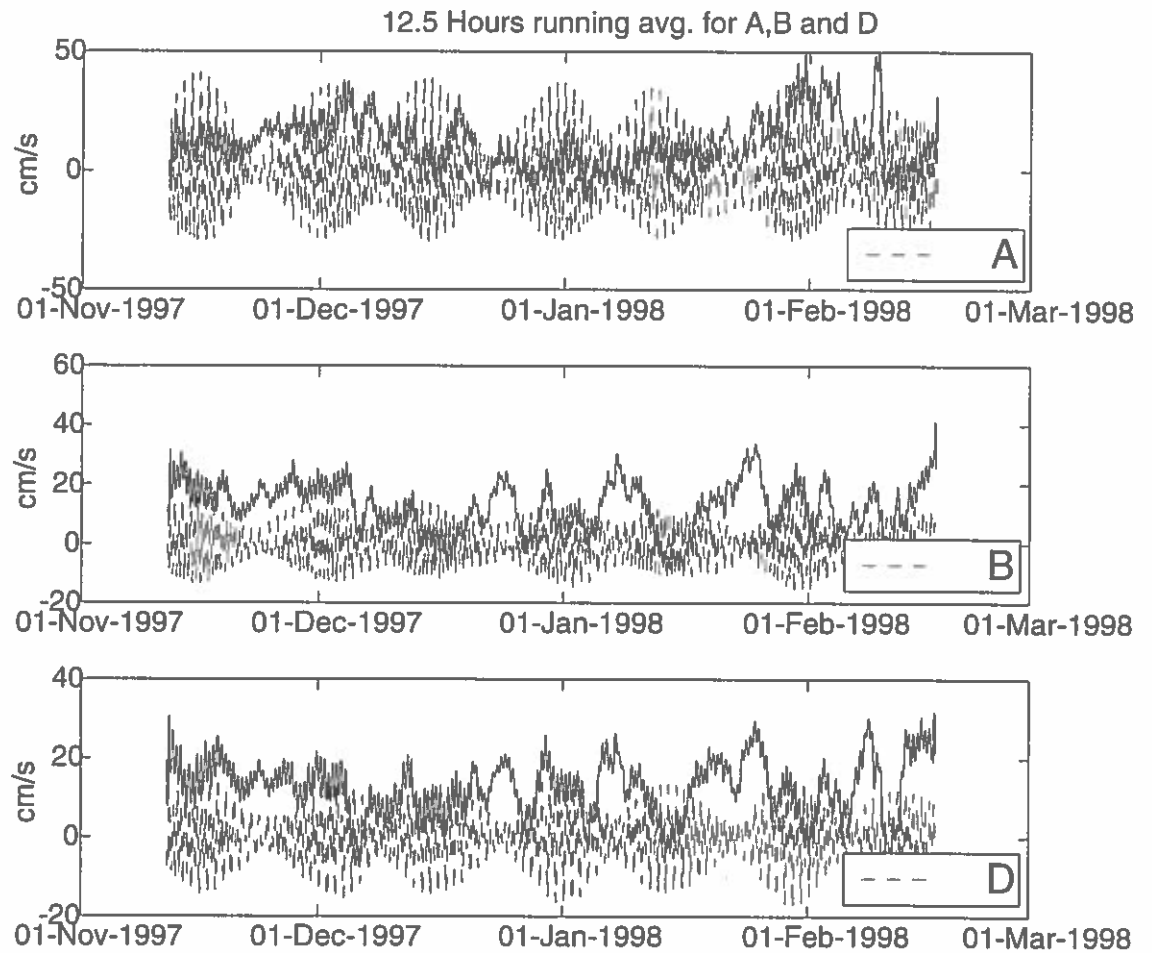
Figure 8.1 Running average of depth-averaged current data, over one tidal cycle, compared to tidal currents from a model (Simonsen, 2000). Sites B and D show that residual currents in the eastward direction are strongest at neap tide. Note the different scaling.

flow has isopycnals with a gradient, and the slope of these isopycnals determine the vertical velocity shears. Internal tides is a phenomena induced in these isopycnals and Pichon & Mazé, (1990) show that internal tide amplitudes can get as large as 80 m. Close to boundaries, like a continental shelf, the internal waves will be intensified and can eventually break. Breaking of internal tides intensifies horizontal mixing, and we know that this tidal mixing is strong on the Faroe shelf (Hansen, private communication).

Sloping isopycnals have greater available potential energy than level isopycnals, and the breaking will lower the center of gravity and even out the slopes somewhat. We know from breaking surface waves that there is a well defined limit for when they break, and the same goes for internal waves. Looking at figure 8.1, window B and D, we see that in mid December, early January, mid January and early February there are sudden decreases in the residual current, and this occurs when the tidal amplitudes are large. This is probably the moments when the internal tides have reached their limit and break. A closer look reveals that these breakdowns occur just after spring, indicating that the breaking tides take some time to induce the current breakdown. Full current strength is restored when we have neap-tides. Tidal mixing was also apparent in the analysis in section 5.3. The tidal traversing method showed that it was only at the shallower farther-from-land instruments that one could detect any horizontal temperature changes, and thereby any significant stratification. In the hodographs plotted with Aanderaa data in figure 5.5, we see that the clearest and strongest tidal signal was measured at site 'a'. The Aanderaa site 'a' is 28 km nearer land than the ADCP station A, and currents are probably barotropic this close to land. Loder (1980), showed that tidal current amplitudes of $1\frac{m}{s}$ magnitudes induced mean Eulerian current speeds of up to 0.23 $\frac{cm}{s}$ on the northwestern side of Georges Bank, and he also showed that this residual currents velocity depends roughly on the square of the tidal amplitude. The tidal amplitudes at 'a' generally do not exceed 0.5 $\frac{m}{s}$, so we can at the most expect a tidally rectified current around the Faroes to be one fourth of the Eulerian current circling Georges Bank, but we have too short time series to conclude anything. More data and the tidal current model could tell us about the effect of this contribution to the FCC.

8.5 Why sinusoidal z-dependency?

The z-dependency is very stable and a part of the explanation must lie in the local bathymetry. All profiles have a minimum eastward velocity slightly below 500 m, and this is explainable if we look at figure 2.3. The IFR is broad and in the area where it connects to the Faroe Plateau it is close to 500 m deep. We know that the overflow of AIW just reaches over the IFR, making the inflow conditions very uniform, and this may explain the lower velocity boundary. Why so sinusoidal? Sjöberg and Stigebrandt (1992) use a normal mode model to analyze currents over a sill. The model used knowledge from a barotropic tidal model, an assumed stratification as

a function of depth and a sill topography, to simulate the generation of internal progressive waves. Rotation and friction are neglected, and the barotropic tide is the generator of the internal waves; a conversion of barotropic energy to baroclinic energy. The vertical distribution to, and above, the step (sill) are assumed known, and below the top of the step the normal velocity should vanish which enforces a baroclinic response, it is argued. The first and the second mode (horizontal velocity $U_{1,2}(z)$), that the model produces, resembles the shear that we observe from our data. It is also mentioned that the modal energy flux (10^{-4} W m^{-2}) in the North Atlantic is distributed like this: mode 1) : 34, mode 2) :11, mode 3) : 5, mode 4) : 3 and mode 5) : 2. This indicates that modes one and two probably are dominant in our waters. This may have something to do with the shear profile. A more detailed study is needed to resolve this issue. A barotropic tidal model is available, quite dense CTD data are available for approximating the stratification $\rho(z)$ and the sill-topography is well known. If up-stream flow conditions could be made available as well one could check this idea and compare it with reality.

The sinusoidal form predicts also a slight current decrease close to sea-surface and this characteristic fits the Aanderaa data remarkably well. The Aanderaa data series is too short for any conclusive remarks, but these are the only near-surface current meter data from this section at present. Until better evidence is found, this might be a possible current behavior in near surface layer. This, however, is not reproduced in the CTD-profiles and is therefore a barotropic phenomena, most probably friction. This to should be studied in more detail.

8.6 Suggested moorings based on the sectional current profile

The remarkably sinusoidal z-dependence in the vertical current profile, which was common for all years (see also figure 8.2), and the fit with a normal distribution in the lateral direction, made an analytic function for the velocity profile possible to suggest. This model predicts most of the observed features, and should give accurate annually averaged flux estimates. The z-dependence might vary a bit inter-annually but can be established with only one ADCP placed fairly close to the current jet core. To estimate the y-dependence more instruments are needed, and the main objective of this work is to predict a deployment pattern that gives us the most information using the fewest instruments. The suggested distribution has four calibration coefficients, ε_y, β_y, μ_y and σ, and, if we for now assume that this is an accurate description of the real profile, we could by the use of four ADCP determine the profile absolutely. That is, four equations or data are needed to determine four unknowns. All data indicate that the high velocity core lies above the 600 - 650 m isobaths, so if one is to deploy four instruments in this section I would suggest that these were placed in the following way: The peak in 1997 was 56.5 km from the origin in our coordinate frame, and the distance in 1998 was 58 km so a general choice for the peak is 57 km. The four instruments should be placed symmetrically around this peak, and the
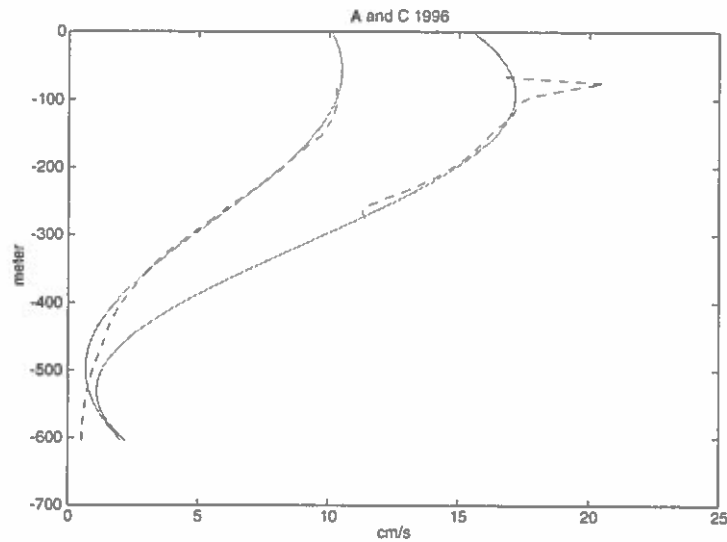
Figure 8.2 Two ADCPs velocity profiles (dashed lines) deployed in 1996-97. The exact same z-dependence (full line) as the two consecutive years is used, with different weights.

Table 8.1 Suggestion for moorings if four instruments are available

	A	B	C	D
This frame (km)	37	50.3	63.5	77
Positions	$62°40.00'N$	$62°47.16'N$	$62°54.30'N$	$63°01.56'N$
Approx. depth (m)	215	445	995	1600

distances 6.66 km and 20 km will give 88% and 32% of the maximum current value respectively. The suggested moorings are found in Table 8.1, where all lie on the $6°05'W$ string.

This would cover the main part of the current, and a very solid estimate could be derived. There might be problems around 500 m, because of intensive fishing activity, but it is highly advisable that a bottom mounted ADCP with fishing-net proof shield be placed here. We have ample evidence that the largest part of the Faroe Current is baroclinic. The strong vertical shears, the steeply sloping isopycnals and the good correspondence between ADCP to CTD profiles at the deeper locations are the most clear evidence, and this might help us to make good estimates with one ADCP instrument less. These instruments are very expensive, and a lot could be saved. The coefficients ε_y, β_y, μ_y and σ for the y-dependence did not change much from 1997-98 to 1998-99. The "background" ε_y and the spread σ actually remained the same, while the amplitude β_y and the placing μ_y varied. For flux calculational purposes I expect the geostrophic, baroclinic current from CTD measurements on the seaward flank at distances greater than 90 km, in our frame, to represent a sufficiently

Table 8.2   Suggestion for mooring if three instruments are available

	A	B	C
This frame (km)	42	57	69
Positions	$62°42.60'N$	$62°50.58'N$	$62°57.24'N$
Approx. depth (m)	300	660	1250
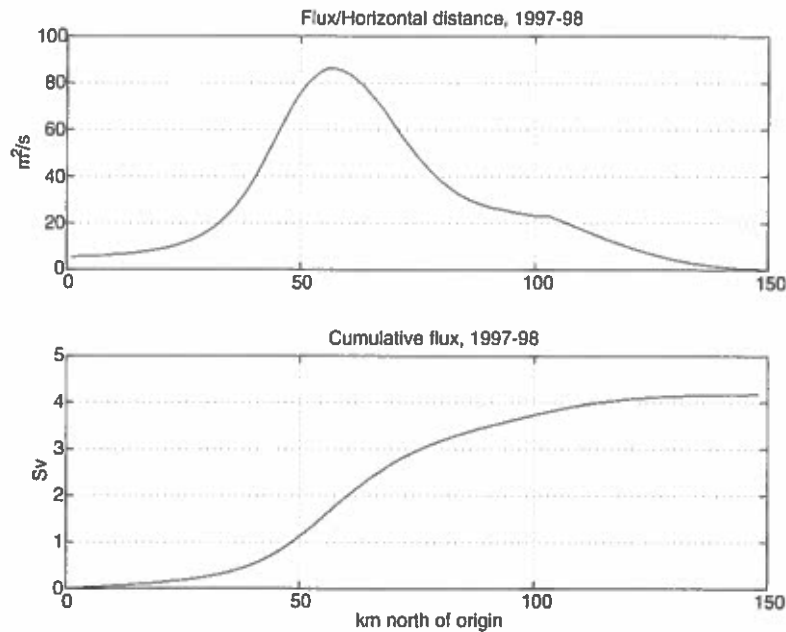
Figure 8.3   Illustration of where largest fluxes are. Upper window shows the volume flux per horizontal distance and lower window shows the cumulative flux.

accurate measure for the current profile. These measurements are routinely made, and will always be available. It might therefore be sufficient with only three ADCPs, and for this approach I would suggest these mooring positions:

Assuming same peak placing ($y = 57$ km in our frame) I propose a symmetric deployment pattern with one instrument placed as near the peak as possible, and the other two 15 km from the peak measuring approximately 53% of the maximum current. The suggestion is shown in Table 8.2., and the longitude is still $6°05'W$.

It is not advisable to use less than three ADCPs, if no other measurements are made. This would be too sparse to compute a reliable estimate on, but if bottom pressure measurements were made at the same time, two ADCPs could be used, and in that case these should be placed at $y = 47$ km and $y = 67$ km in our frame. This is at $62°45.36'N$ and $62°56.16'N$ respectively, measuring 76% of maximum current.

These suggestions assume good support from CTD measurements on the northermost flank, and the plot showing the cumulative flux in figure 8.3, shows that almost

one Sverdrup must come from CTD data, when we take 77 km as the most remote ADCP. It might seem like we have placed the ADCPs to close to land, but the suggestion in the tables gives the best coverage of the expected geometry of the profile. It also covers the area with most flux, and the CTDs come into play when the necessity of a phase function (7.2) becomes apparent.

The drawback with this method is that it cannot make predictions on a short time scale. But it gives good information on the geographical form of the current jet in both vertical and horizontal directions. This information helps when constructing a model for calculating short time volume fluxes. Following the examples of Hansen et al. (1999) and Turrell et al. (1999) where the section is divided into boxes, a coarse preliminary model using this method was employed in the correlation analysis.

Chapter 9
CONCLUSION

A compilation of different oceanographical data has given valuable information on the Faroe Current. Annual averages of ADCP data from the years 1994-99 are employed to establish a model for the sectional current profile. The upward looking ADCPs give much information from where they are placed and up through the water column, but only two to four ADCP instruments are deployed at a time, and other oceanographical data are therefore used in the gaps where no ADCPs are. CTD data have been used on the northern-most flank of the current where they are believed to well account for the absolute current velocities. Short time series of Aanderaa current meter data are use in a region closer to the shelf. The model-sectional profile produced from this analysis can be used to calculate annually averaged volume fluxes, and we find the fluxes for the years 1997-98 and 1998-99 to be 4.17 Sv and 4.56 Sv respectively. From this model we also find that the Faroe Current is mainly a baroclinic shelf guided current with a strong vertical shear in the region with strongest currents. The barotropic and the baroclinic components are mixed, and there is a continuous transition from a mainly barotropic component over the 200 m isobath to a purely baroclinic component when the bottom depths exceed 1 km. The sectional current profile reveals a broad current jet with maximum current velocities and maximum volume flux above the 600-650 m isobaths. The highest velocities in this annually averaged profile are 25-30 $\frac{cm}{s}$ and they occur approximately one hundred meters under the sea-surface. Nearly 80 % of the volume flux occurs in a 60 km wide region centered at the current peak. The vertical current profile shape changes little inter-annually, and a cosine-form seems to fit this shape each year. Inter-annual changes in the horizontal distribution can not be determined accurately at present because of to coarse horizontal resolution in the data coverage. It seems as the location and the spread of the jet remain fairly constant, while the maximum velocities, or the jet amplitude, will vary inter-annually.

A method that reveals short time characteristics of horizontal current profile is developed. Measured current data are assumed to consist of the slope guided jet, and a "disturbing" tidal current. A tidal current model is used to de-tide the eastward components of the vertically averaged ADCP data, and the residual is assumed to be the jet in this direction. The results from this analysis give the expected gradients of the instantaneous horizontal current profiles, but the magnitudes of these gradients are not reliable. This method must be developed further, before it is been used in

applications.

Water level data from Tórshavn in the period 1991-2000 have been adjusted for atmospheric pressure, and these corrected sea-level times-series are compared to current data. A good but negative correlation is found between most individual current data and the coastal sea-level, and these correlations get stronger when long block averages are used. The volume flux in the year 1998-99 is also compared to corrected coastal sea level, and good, but negative, correlation is found. There is a clear volume flux seasonality in the Faroe Current with highest fluxes in early spring, and lowest fluxes during late summer. The corrected water level shows the opposite character.

Based upon the sectional current profile, suggestions are given of where to deploy future ADCPs along this section. This is done in the cases when three or four ADCP instruments are available. To use more than four instruments is not found necessary, and to deploy less than three instruments will not be helpful unless data are collected in other ways also. These deployment strategies should give good data coverage with the fewest instruments.

Appendix A
ADDITIONAL FIGURES
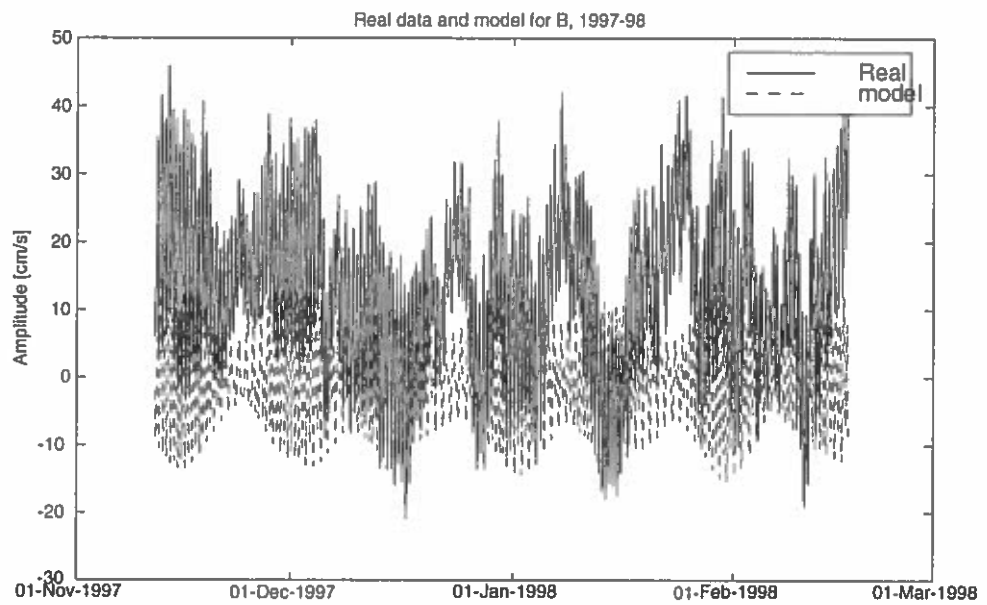
Figure A.1   Three months of data from mooring B (907m) compared with a barotropic tidal model. The fluctuations are neap and spring, and we see a nice correlation. The constituents $M_2, S_2, O_1, K_2, N_2, P_1, K_1,$ and Q_1, are found in the model.

A.1   Related to high-resolution ADCP data

Figures for sites B and D, equivalent to the ones presented for ADCP station A in section 6.1, are presented here.
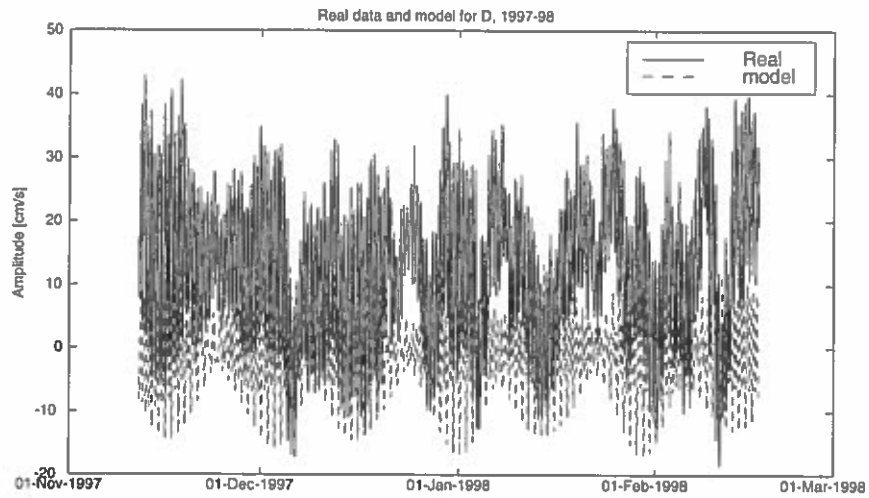
Figure A.2   Three months of data from mooring D (1283m) compared with a barotropic tidal model. The data show less tidal signal than those close to land, and there is a tendency that higher velocities are found at neap. $M_2, S_2, O_1, K_2, N_2, P_1, K_1,$ and $Q_1,$ are found in the model.
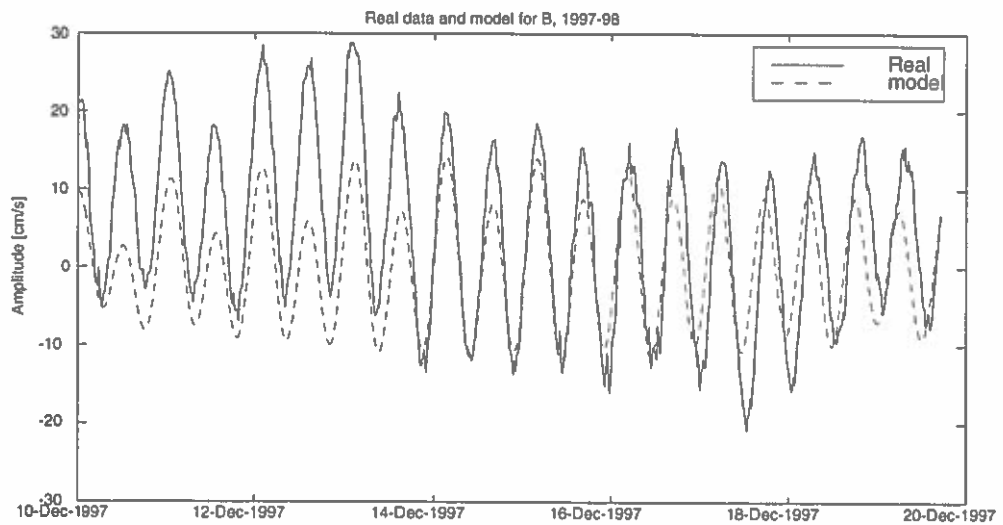
Figure A.3   Depth-averaged data from mooring B (907m) over ten days compared to the model. The east-west component of the current velocities is shown, being positive eastwards. This in an even better match than at A, and the semidiurnal-diurnal mixture fits better.
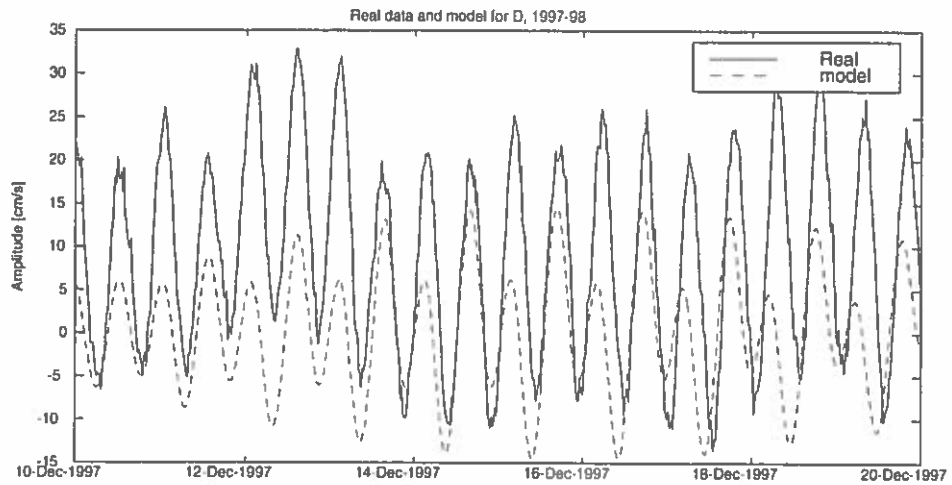
Figure A.4   Depth-averaged data from mooring D (1283m) over ten days compared to the model. The east-west component of current velocities is shown, being positive eastwards. The model predicts, like in A, somewhat larger mixture of diurnal and semidiurnal signals, but corresponds well to the data.
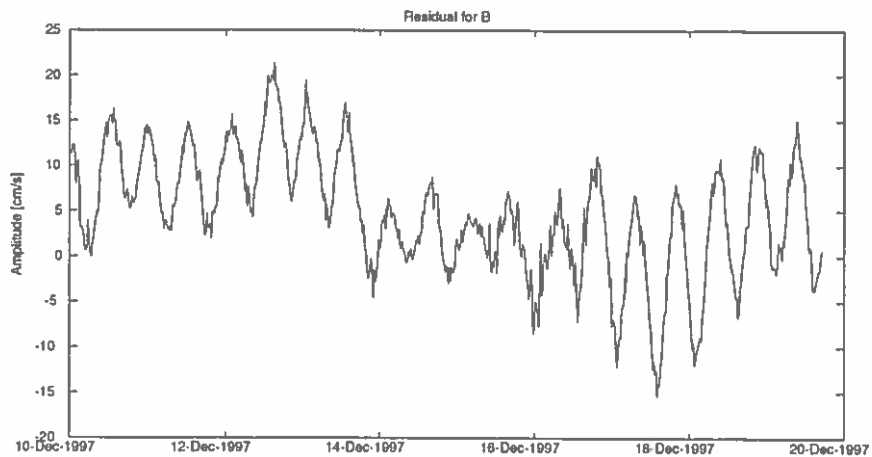
Figure A.5   The velocity residual found by subtracting the model-syntesized time series from the data at B.
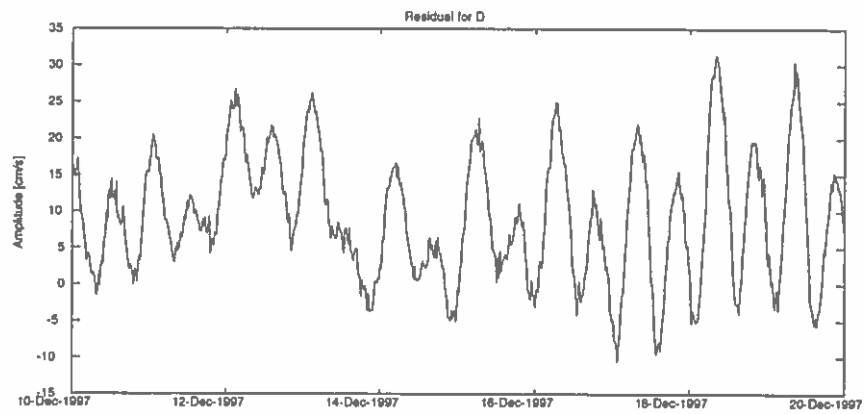
Figure A.6   The velocity residual found by subtracting the model-syntesized time series from the data at D.
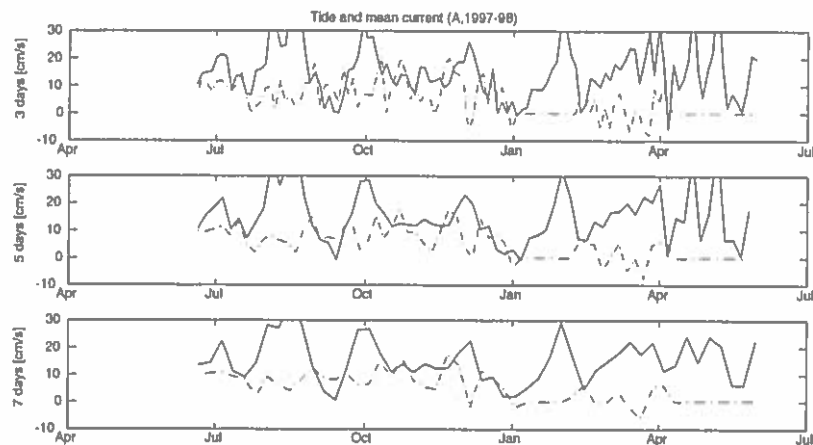
Figure A.7 A closer look at the depth averaged east-west current velocity (full lines) at mooring A, compared to the corrected water level (dashed lines) in Tórshavn from the period 1997-98. We compare 3, 5 and 7 day averages and the flat dashed line shows missing data.

A.2 Related to daily averaged ADCP data

Data from the period 1997-98 are presented here for three, five and seven days block averages. Water level data from this period were missing so longer block are not included from this period. Data from the periods 1994-95 and 1996-97 respectively, are presented including vertical velocity profiles. Correlations between water level data from Tórshavn and depth-averaged eastward current velocities in periods 1994-95, 1996-97 and 1998-99 are presented here. These water level data are also compared to the total volume flux, calculated from a coarse algorithm, during the year 1998-99. The correlations are found from five days, fifteen days and one month block-averaged data. A diagram showing how water level data is adjusted with air pressure data from Tórshavn is also given.
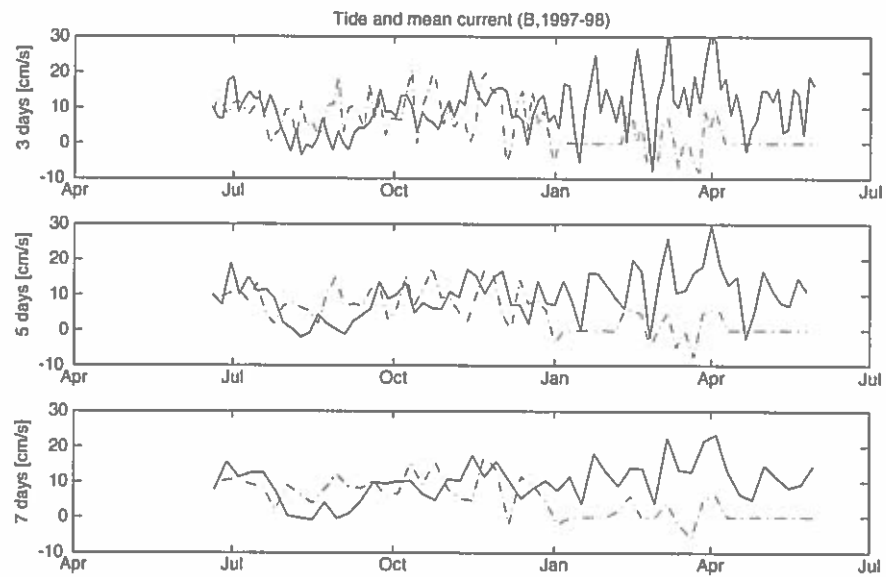
Figure A.8 A closer look at the depth averaged east-west current velocity (full lines) at mooring B, compared to the corrected water level (dashed lines) in Tórshavn from the period 1997-98. We compare 3, 5 and 7 day averages and the flat dashed line shows missing data.
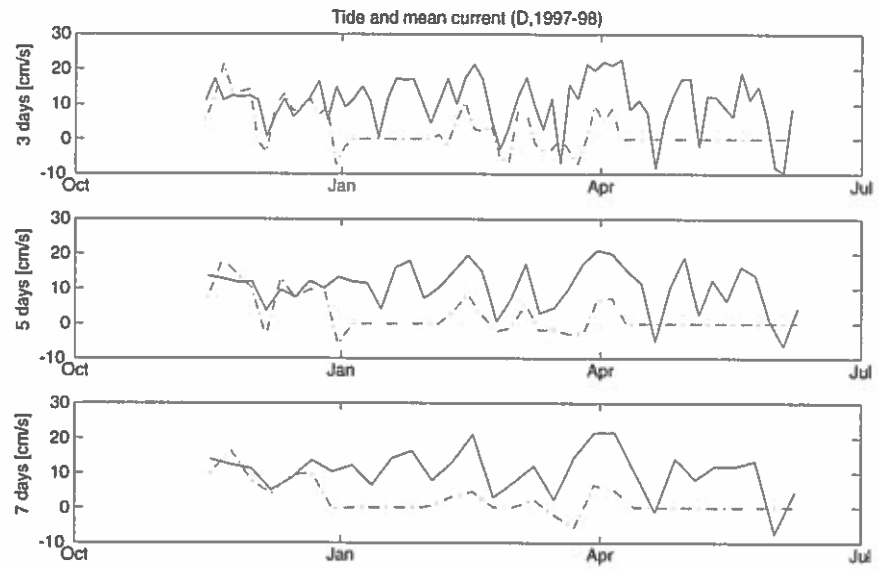
Figure A.9   A closer look at the depth averaged east-west current velocity (full lines) at mooring D, compared to corrected water level (dashed lines) in Tórshavn during the period 1997-98. We compare 3, 5 and 7 day averages and the flat dashed line shows missing data.
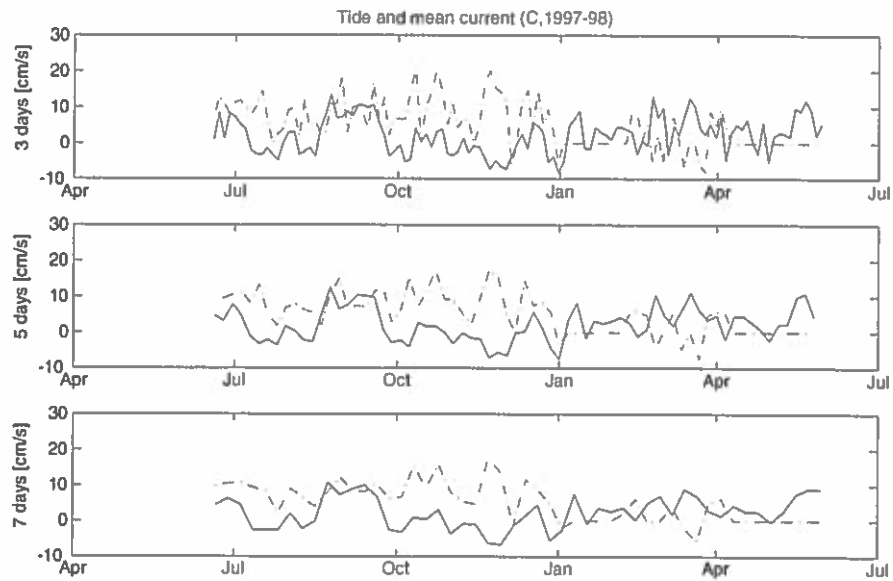
Figure A.10   A closer look at the depth-averaged east-west current velocity (full lines) at mooring C, compared to the corrected water level (dashed lines) in Tórshavn during the period 1997-98. We compare 3, 5 and 7 day averages and the flat dashed line shows missing data.
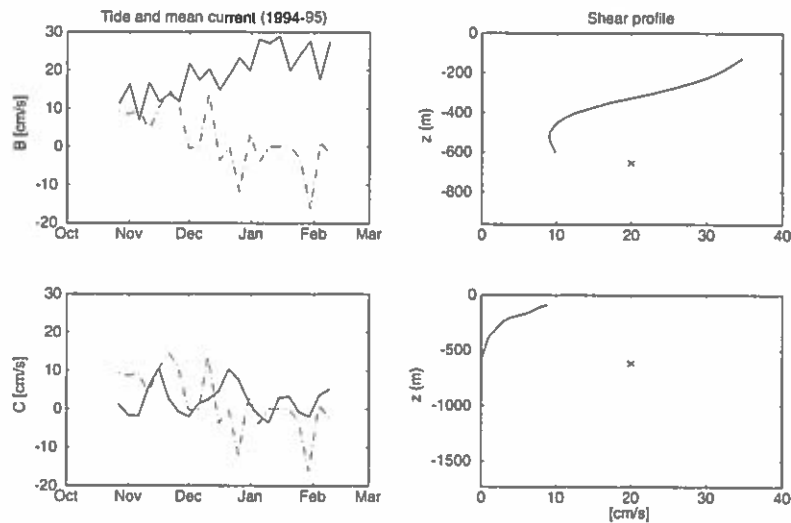
Figure A.11   Overview over data from 1994-95, where the dashed line is five-day average water-level in Tórshavn and the full is east-west depth-averaged current at site B and C. Their averaged shear profiles over the period are also shown. Lower axis in shearprofile figures is at bottom depth, and the 'x' marks the instrument position.
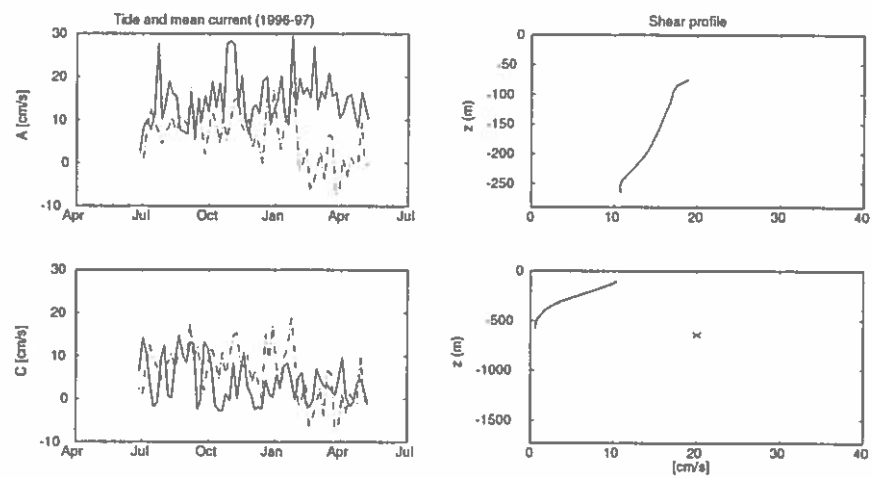
Figure A.12 Overview over data from 1996-97, where the dashed line is the five-day average water-level in Tórshavn and the full is east-west depth-averaged current at site A and C. Their averaged shear profiles over the period are also shown. Lower axis in shearprofile figures is at bottom depth, and the 'x' marks the instrument position.
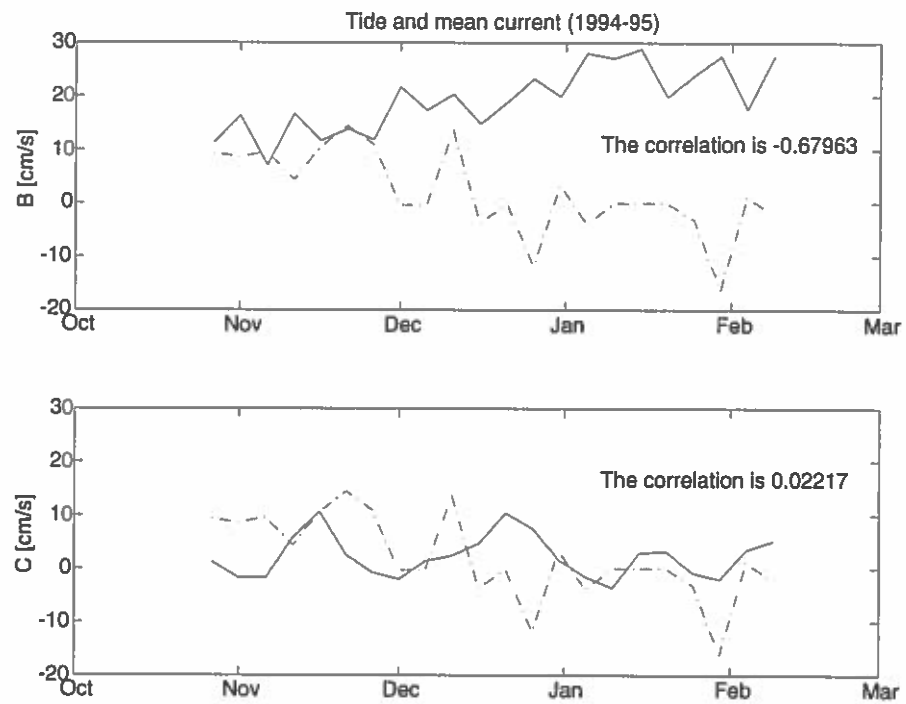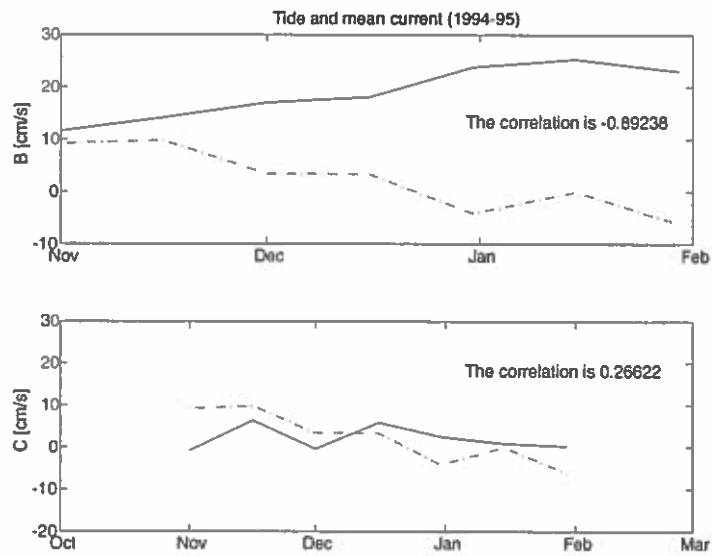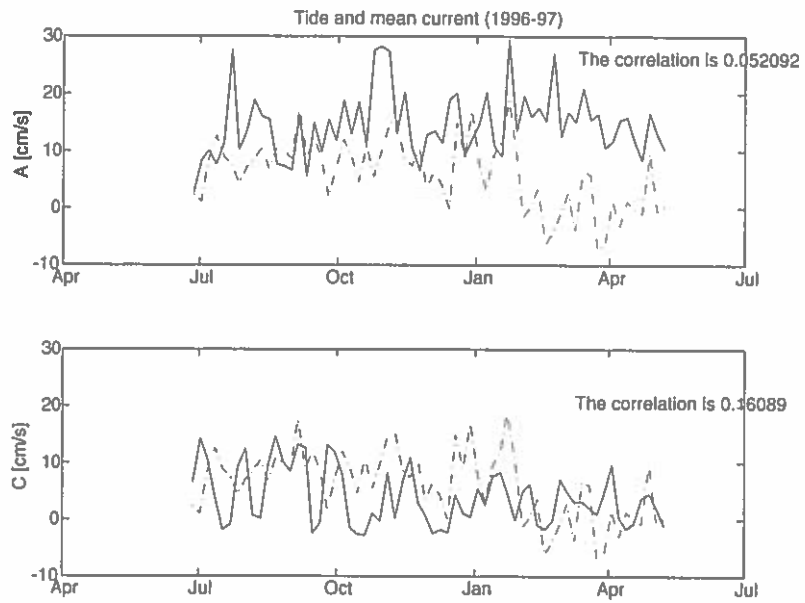
Figure A.13 Five-day block averages of depth averaged current velocities (full) and corrected waterlevel in Tórshavn (dashed). All available ADCP current data from the period 1994–95 are shown.
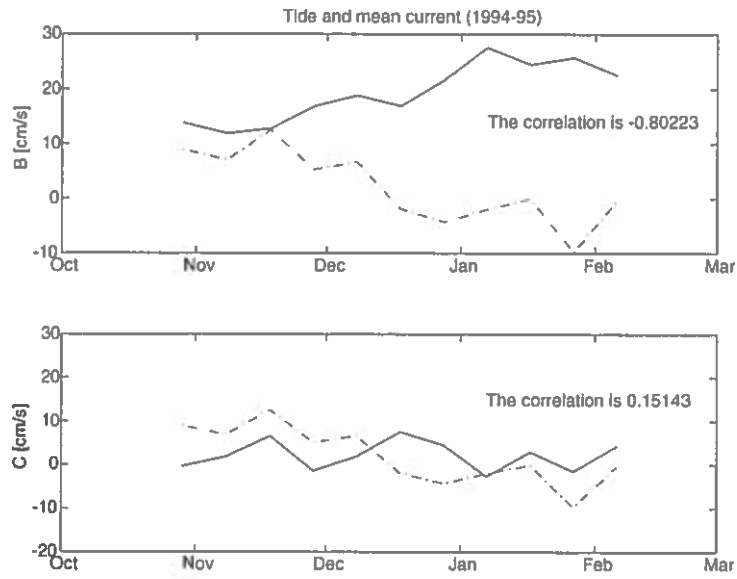
Figure A.14 Fifteen-day block averages of depth averaged current velocities (full) and corrected waterlevel in Tórshavn (dashed). All available ADCP current data from the period 1994-95 are shown.
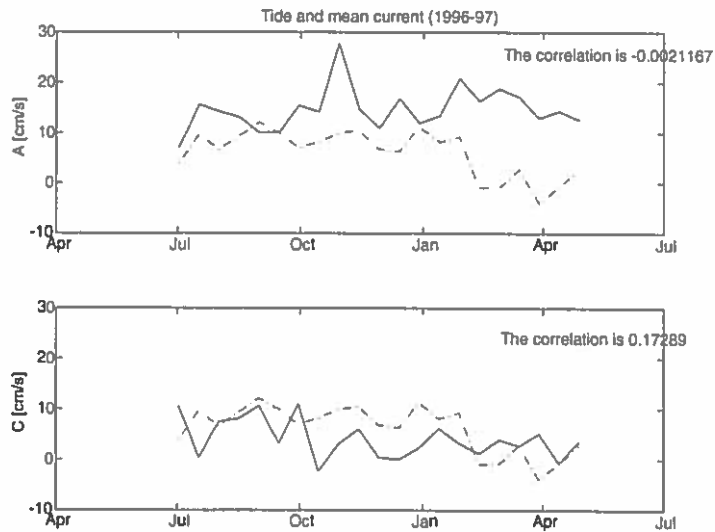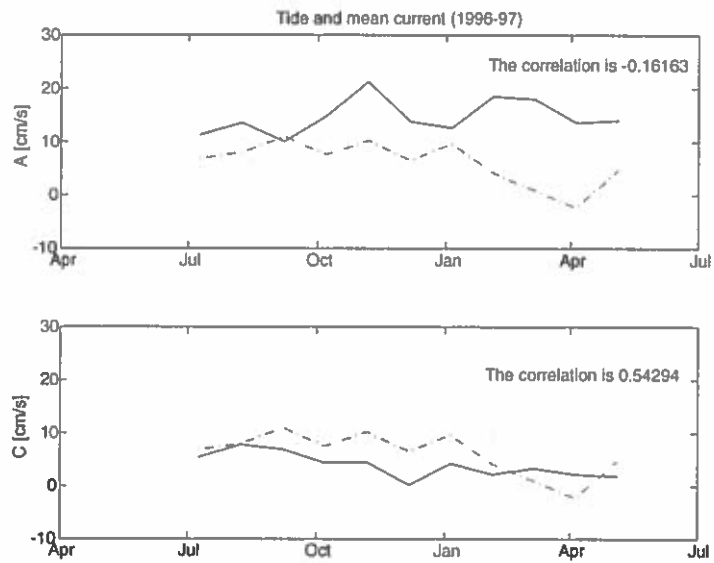

Figure A.15 One month block averages of depth averaged current velocities (full) and corrected waterlevel in Tórshavn (dashed). All available ADCP current data from the period 1994-95 are shown.

Figure A.16   Five-day block averages of depth averaged current velocities (full) and corrected waterlevel in Tórshavn (dashed). All available ADCP current data from the period 1996-97 are shown.
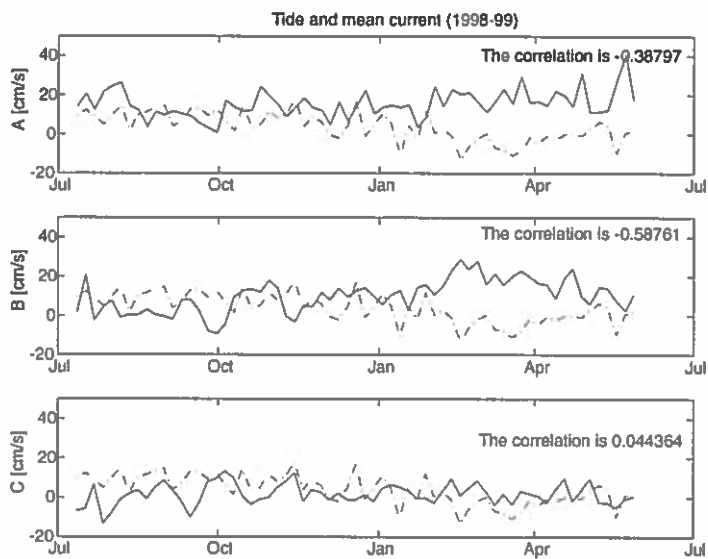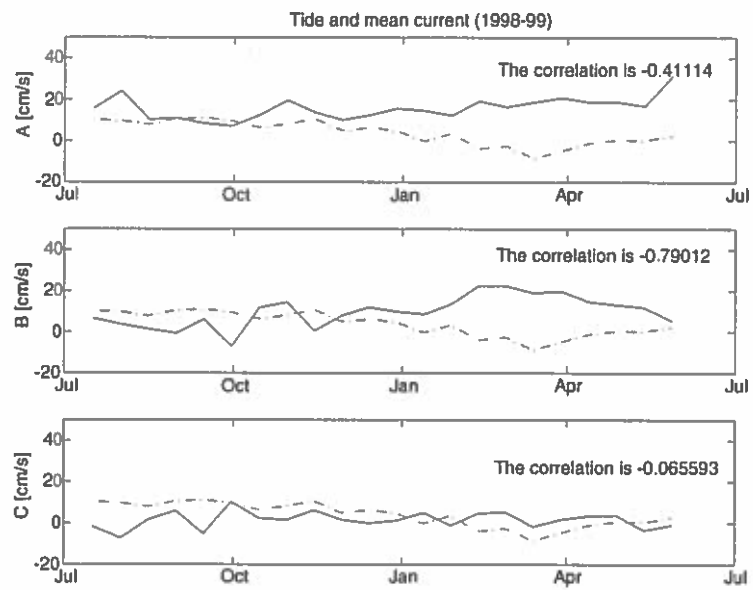

Figure A.17   Fifteen-day block averages of depth averaged current velocities (full) and corrected waterlevel in Tórshavn (dashed). All available ADCP current data from the period 1996-97 are shown.

Figure A.18   One month block averages of depth averaged current velocities (full) and corrected waterlevel in Tórshavn (dashed). All available ADCP current data from the period 1996-97 are shown.

Figure A.19   Five-day block averages of depth averaged current velocities (full) and corrected waterlevel in Tórshavn (dashed). All available ADCP current data from the period 1998-99 are shown.
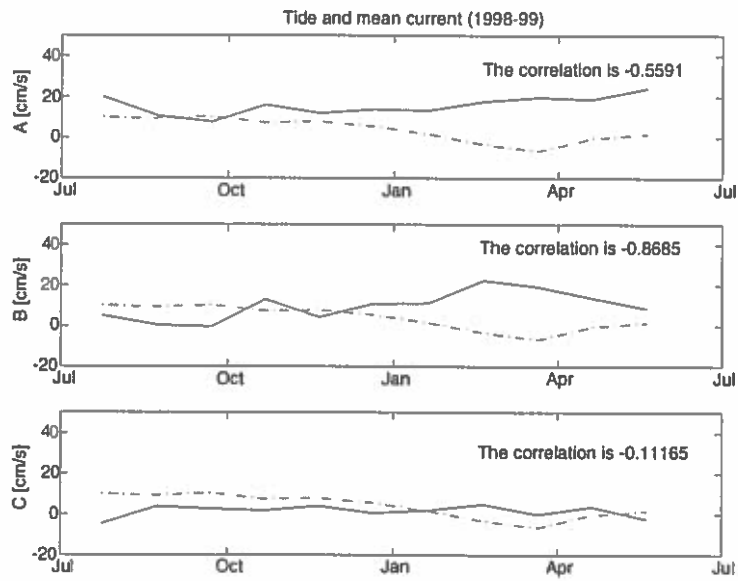
Figure A.20 Fifteen-day block averages of depth averaged current velocities (full) and corrected waterlevel in Tórshavn (dashed). All available ADCP current data from the period 1998-99 are shown.

Figure A.21   One month block averages of depth averaged current velocities (full) and corrected waterlevel in Tórshavn (dashed). All available ADCP current data from the period 1998-99 are shown.
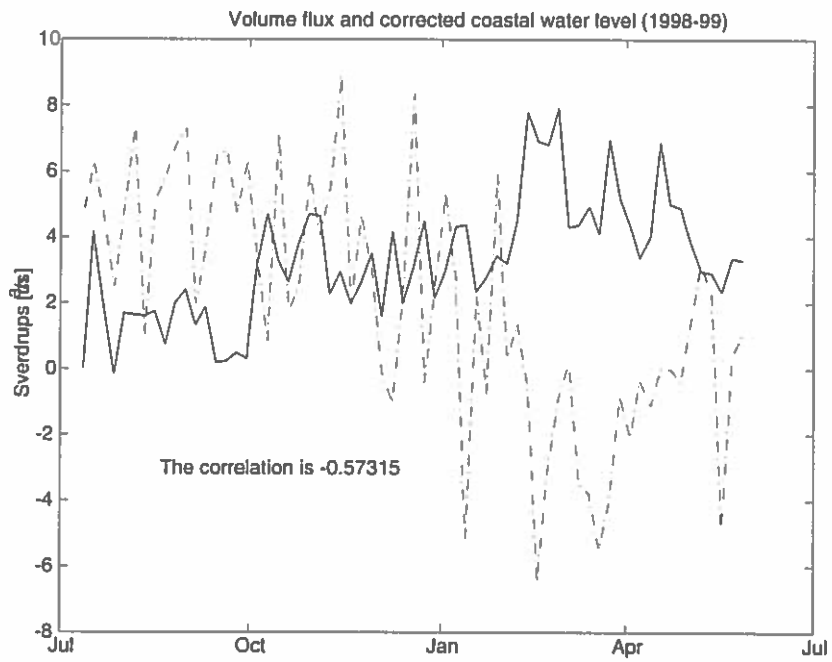
Figure A.22 Total volume flux (full) in eastward direction calculated from a coarse algorithm is compared to corrected water level in Tórshavn. Five-day block average of the total flux (full) in the eastward direction.
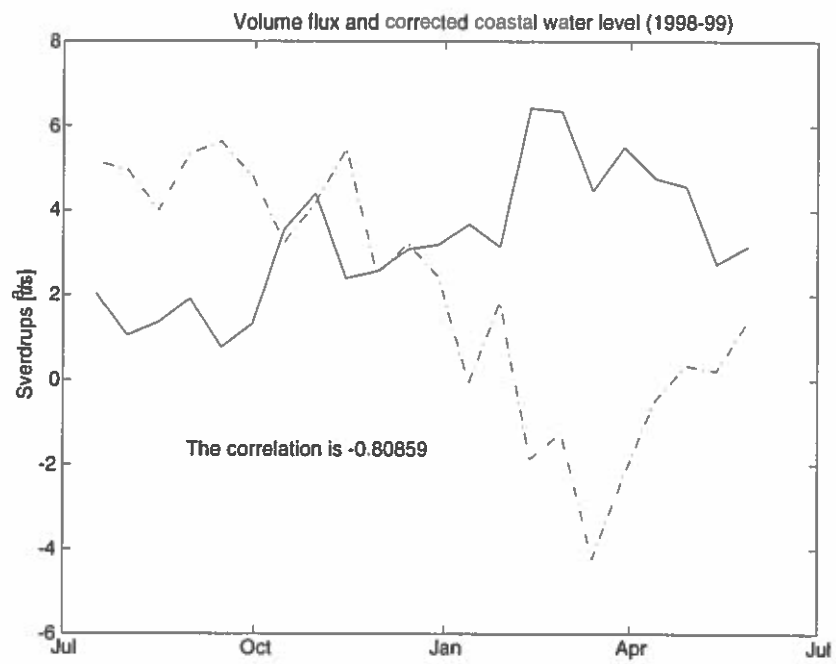
Figure A.23 Total volume flux (full) in eastward direction calculated from a coarse algorithm is compared to corrected water level in Tórshavn. Fifteen-day block average.
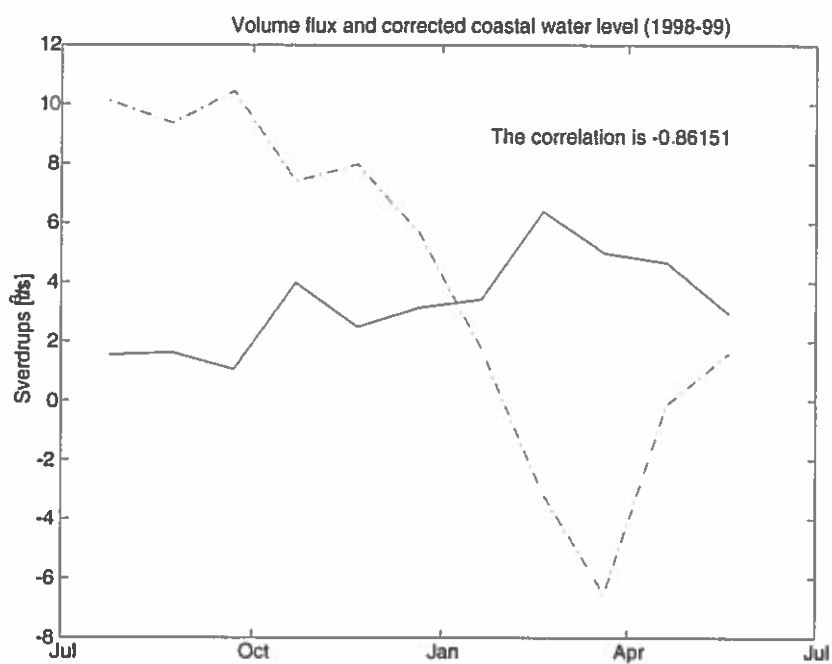
Figure A.24 Total volume flux (full) in eastward direction calculated from a coarse algorithm is compared to corrected water level in Tórshavn. One month block average.
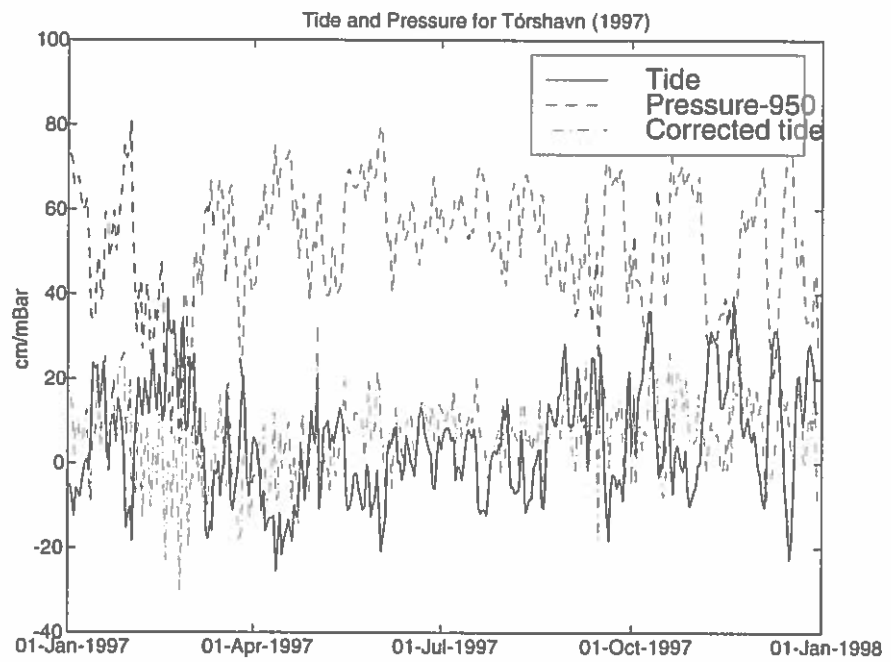
Figure A.25 The water level in Tórshavn is corrected by adding the air pressure time series to the sea level data. One mBar is assumed to suppress the water level by one centimeter.
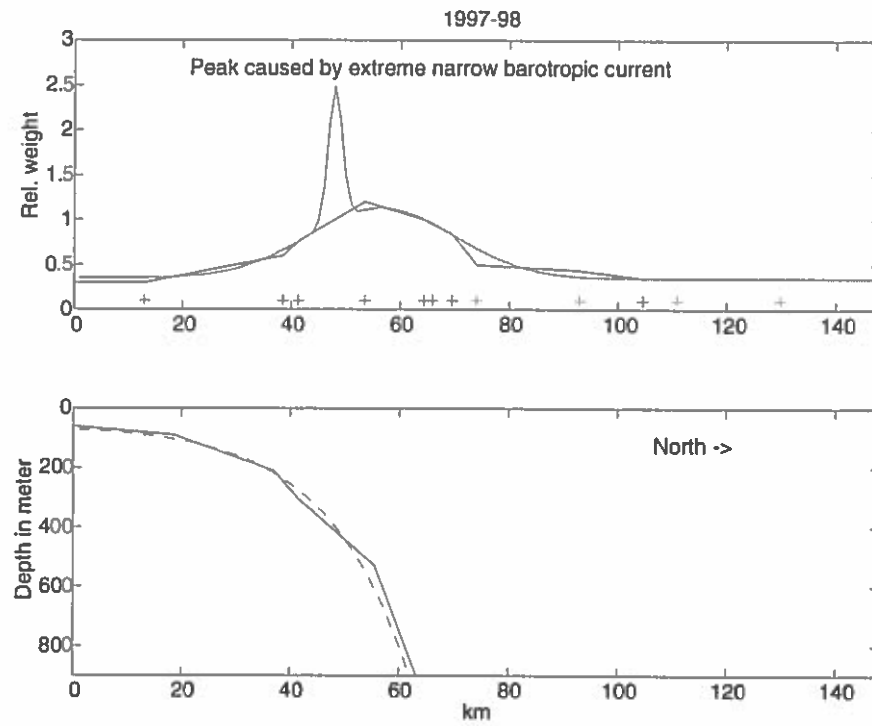
Figure A.26 A "worst" case scenario, with a fast, narrow barotropic current. A 8 km wide jet, with a peak-velocity of 80 cm/s is included in the current profile to check its importance for volume flux calculations. This is done for the year 1997-98.

A.3   Related to averaged current profile

References

Chen,C. and Beardsley, R.C. 1995: *A Numerical study of stratified Tidal Rectification over Finite-Amplitude Banks. Part I: Symmetric Banks. Journal of Physical Oceanography,* Vol **25**, pp. 2090-2109.

Gill, A.E. 1982: *Atmosphere-Ocean Dynamics. Academic Press, Inc. CA., USA.*

Hansen, B. 1975: *Sea level fluctuations in Tórshavn, Preliminary results. Fródskaparrit (Annal.societ.scient. Faroensis).*

Hansen, B., Malmberg, S.A., Sælen,O.H. and Østerhus, S. 1986: *Measurement of flow north of the Faroe Islands, June 1986.* International Council for the Exploration of the Sea. C.M./C:12.

Hansen, B.,Østerhus, S., Kristiansen, R. and Larsen, K.M.H. 1999: *The Iceland-Faroe inflow of Atlantic water to the Nordic Seas.* ICES annual Science Conference 1999.CM 1999/L:21.

Hansen, B. and Østerhus, S. 2000: *North Atlantic- Nordic Seas exchanges. Progress in Oceanography* **45**, *pp.109-208.*

Hansen, B. and Meincke, J. 1984: *Long term coastal sea surface temperature observations at the Faroe Islands.* Rapports et Procès-Verbaux des Réunions du Conceil International pour l 'Exploration de la Mer, **185**, pp. 162-169.

Helland-Hansen, B. and Nansen, F. 1909: *The Norwegian Sea, its physical oceanography. Based on the Norwegian researches 1900-1904.* In Report on Norwegian fishery and marine-investigation, vol **2**.

Hermann, F. 1949: *Hydrographic conditions in the South-Western part of the Norwegian Sea.* Annales Biologiques du Conseil International pour l 'Exploration de la Mer, **5**, 19-21.

Hutnance, J.M. 1981: *Waves and currents near the continental shelf edge.* Prog.

Oceanography, Vol. **10**, pp. 193-226.

Hutnance, J.M. 1992: *Extensive slope currents and the ocean-shelf boundary.* Prog. Oceanography, Vol.**29**, pp. 161-196.

Kundu, P.K. 1990: *Fluid Mechanics.* Academic Press, Inc. CA., USA.

Larsen, K.M.H., Hansen, B. and Kristiansen, R.: *ADCP Deployments in Faroese Waters 1997-1999.* Technical Report No.:99-07, The Faroese Fisheries Laboratory.

Larsen, K.M.H., Hansen, B. and Kristiansen, R.: *Nordic WOCE ADCP Deployments 1994-1997.* Technical Report No.:99-05, The Faroese Fisheries Laboratory.

Li, S. and McClimans, T.A. 1998: *The effects of winds over a barotropic retrograde slope current.* Continental Shelf Research Vol.**18**, pp. 457-485 .

Li, S. and McClimans, T.A. 2000: *The stability of Barotropic and Retrograde Jets along a Sloping Bottom.* JGR.

Loder, J.W. 1980: *Topographic Rectification of Tidal Currents on the Sides of Georges Bank.* Journal Of Physical Oceanography, Vol **10**, pp.1399-1416.

McClimans, T.A. and Lønseth, L. 1984: *Oscillations of frontal currents.* Continental Shelf Research, Vol.**4**, No.6, pp. 699-707.

McClimans, T.A., Johannessen, B.O and Jenserud, T. 1999: *Monitoring a shelf edge current using bottom pressure or coastal seal-level data.* Continental Shelf Research **19**, pp.1265-1283.

Nielsen, J.N. 1904: *Hydrography of the water by the Faroe Islands and Iceland during the cruise of the Danish research steamer 'Thor' in the summer 1903.* Meddelelse fra Kommisionen for Havundersøgelser. Series Hydrografi, I (4) 42 pp.

Orvik, K.A., Skagseth, Ø. and Mork, M. 1999: *Atlantic inflow to the Nordic Seas in the Svinøy section.* International WOCE Newsletter, Number **37**.

Pérenne, N., Pichon, A and Huet, P. 2000: *A numerical study of stratified tidal rectification.* Continental Shelf Research Vol. **20**, pp. 37-68.

Pichon and Mazé 1990.

Pond, S & Pickard, G. 1983: *Introductory Dynamical Oceanography (Second Edition).* Pergamon Press.

Poulain, P.M., Warn-Varnas, A., & Niiler, P.P (1996): *Near-surface circulation of the Nordic seas as measured by Lagrangian drifters.* Journal of Geophysical Research, 101, 18237-18258.

Schwiderski, E.W. 1980: *On charting global ocean tides*, Reviews of geophysics and space physics, vol **18**, No 1, pp. 243-268.

Sjöberg, B. & Stigebrandt, A. 1992: *Computations of the geographical distribution of the energy flux to mixing processes via internal tides and the associated vertical circulation in the ocean.* Deep-Sea Research Vol. **39**, pp. 269-291.

Tait, J.B. 1957: *Recent oceanographical investigations in the Faroe-Shetland Channel.* Proceedings of the Royal Society, London, **18**, 239-289.

Tait, J.B. 1967: *The Iceland-Faroe Ridge international (ICES) 'Overflow' expedition, May-June 1960.* Rapport et Procès-Verbaux des Réunions du Conseil International pour l 'Exploration de la Mer, **157**, pp 71.

Turrell, W.R, Hansen, B, Østerhus, S, Hughes, S., Ewart, K. and Hamilton, J. 1999: *Direct observations of Inflow to the Nordic Seas through the Faroe Shetland Channel 1994-1997.* Nordic Seas Exchange. CM 1999/L:01.

List of Abbreviations

ADCP: Acoustic Doppler Current Profiler.

AIW: Arctic Intermediate Water.

CTD: Conductivity, Temperature & Depth.

DSU: Data Storing Unit.

FB(C): Faroe Bank (Channel).

FC: Faroe Current.

FCC: Faroe Coastal Current.

FFL: Faroese Fisheries Laboratory.

FSC: Faroe-Shetland Channel.

IFR: Iceland-Faroe Ridge.

MAIA: Monitoring the Atlantic Inflow toward the Arctic.

MEM: Maximum Entrophy Method.

NAC: North Atlantic Current.

NAO: North Atlantic Oscillation.

NH: Northern Hemisphere.

RCM: Recording Current Meter.

VEINS: Variability of Exchanges in the Northern Sea.

WOCE: The World Ocean Circulation Experiment.